**UNIVERSIDAD AUTÓNOMA DE MADRID**

**FACULTAD DE CIENCIAS**

**DEPARTAMENTO DE FÍSICA DE MATERIALES**

ERVING CLAYTON XIMENDES

# Multifunctional nanoparticles for hyperthermia, thermometry and fluorescence imaging in the biological windows

Madrid

2018

**UNIVERSIDAD AUTÓNOMA DE MADRID**

**FACULTAD DE CIENCIAS**

**DEPARTAMENTO DE FÍSICA DE MATERIALES**

ERVING CLAYTON XIMENDES

# Multifunctional nanoparticles for hyperthermia, thermometry and fluorescence imaging in the biological window

Thesis report presented as a partial requirement to obtain a PhD title in Physics.

PhD thesis advisors:
Daniel Jaque García (UAM – Spain)
Carlos Jacinto da Silva (UFAL – Brazil)

Madrid

2018

**UNIVERSIDAD AUTÓNOMA DE MADRID**

**FACULTAD DE CIENCIAS**

**DEPARTAMENTO DE FÍSICA DE MATERIALES**

ERVING CLAYTON XIMENDES

# Nanopartículas multifuncionales para hipertermia, termometría e imágenes de fluorescencia en las ventanas biológicas

Memória presentada para optar por el grado de Doctor en Ciencias Físicas.

Directores de Tesis:
Daniel Jaque García (UAM – España)
Carlos Jacinto da Silva (UFAL – Brasil)

Madrid

2018

**UNIVERSIDADE FEDERAL DE ALAGOAS**

**INSTITUTO DE FÍSICA**

**PROGRAMA DE PÓS-GRADUAÇÃO IF-UFAL**

ERVING CLAYTON XIMENDES

# Nanopartículas multifuncionais para hipertermia, termometria e imagem de fluorescência nas janelas biológicas

Tese apresentada como requisito parcial para obtenção do título de Doutor em Física.

Orientadores da Tese:
Daniel Jaque García (UAM – Espanha)
Carlos Jacinto da Silva (UFAL – Brasil)

Maceió

2018

# Abstract

In this thesis, the use of core/shell engineering for the synthesis of fluorescent nanoparticles (NPs) capable of operating as nanothermometers, nanoheaters and/or contrast agents for fluorescence imaging in small animal models is explored. The materials here studied – rare-earth ($Nd^{3+}$, $Yb^{3+}$, $Tm^{3+}$ and/or $Er^{3+}$) doped NPs and PbS/CdS/ZnS quantum dots (QDs) – presented emission and/or excitation bands in the so-called biological windows, where light penetration into tissues is maximal, allowing for *ex vivo* and *in vivo* applications. It was demonstrated that the spatial separation between the rare-earth ions, achieved by the core/shell nano-engineering, resulted not only in a considerable improvement on the values of thermo-optical parameters such as the light-heat conversion efficiency and the relative thermal sensitivity, but also on a multi-functionality of the nanosystems. As a consequence, innovative applications in nanothermometry were successfully accomplished when developing this thesis. Among those applications, one can mention: the study in real time of the thermal dynamics of an *in vivo* tissue, the detection and monitoring of cardiovascular diseases and the recording of *in vivo* thermal images and videos at a subcutaneous level by means of a ratiometric approach. The results here presented open up avenues for new diagnosis and control techniques that can revolutionize the current methods found in biomedicine.

# Resumen

En esta tesis, se explora el uso de la ingeniería de núcleo/cascara (en inglés core/shell) para la síntesis de nanopartículas (NPs) fluorescentes capaces de operar como nanotermómetros, nanocalentadores y/o agentes de contraste para imágenes de fluorescencia en modelos de animales pequeños. Los materiales aquí estudiados - NPs dopadas de tierras raras ($Nd^{3+}$, $Yb^{3+}$, $Tm^{3+}$ y/o $Er^{3+}$) y puntos cuánticos (en inglés, quantum dots - QDs) de PbS/CdS/ZnS - presentaron bandas de emisión y/o excitación en las llamadas ventanas biológicas, donde la penetración de la luz en los tejidos es máxima, lo que permitió aplicaciones *ex vivo* e *in vivo*. Se demostró que la separación espacial lograda mediante la nanoingeniería de núcleo/caparazón, dio como resultado no solo una mejora considerable en los valores de los parámetros termoópticos, tales como la eficiencia de conversión de luz-calor y la relativa sensibilidad térmica, sino también en una multifuncionalidad de los nanosistemas. Como consecuencia, algunas aplicaciones innovadoras en nanotermometría se lograron con éxito al desarrollar esta tesis. Entre esas aplicaciones, se pueden mencionar: el estudio en tiempo real de la dinámica térmica de un tejido in vivo, la detección y el control de enfermedades cardiovasculares y el registro de imágenes y videos térmicos *in vivo* a nivel subcutáneo mediante un enfoque ratiométrico. Los resultados presentados aquí abren vías para nuevas técnicas de diagnóstico y control que pueden revolucionar los métodos actualmente encontrados en la biomedicina.

# Resumo

Nesta tese, explora-se o uso da engenharia core/shell para a síntese de nanopartículas fluorescentes capazes de operar como termômetros, nano-aquecedores e/ou agentes de contraste em imagens fluorescentes em modelos animais. Os materiais aqui estudados – pontos quânticos de PbS/CdS/ZnS e NPs dopadas com terras-raras ($Nd^{3+}$, $Yb^{3+}$, $Tm^{3+}$ e/ou $Er^{3+}$) – apresentaram emissão e/ou excitação dentro das chamadas janelas biológicas, onde a penetração da luz é maximizada permitindo, portanto, aplicações *ex vivo* e *in vivo*. Foi demonstrado que a separação espacial entre os íons terras-raras, alcançada por meio da nano-engenharia core/shell, resultou não somente em uma melhora nos valores dos parâmetros termo-ópticos tais como a eficiência de conversão luz-calor e a sensibilidade térmica relativa, mas também na multifuncionalidade dos nano-sistemas. Como consequência, aplicações inovadoras foram alcançadas no campo da termometria luminescente durante o desenvolvimento desta tese. Dentre essas aplicações, pode-se mencionar: o estudo em tempo real da dinâmica térmica de um tecido vivo, a detecção e monitoramento de doenças isquêmicas e a gravação de imagens e vídeos térmicos *in vivo* a nível subcutâneo por meio da abordagem ratiométrica. Os resultados aqui apresentados abrem muitas portas para novas técnicas de diagnóstico e controle que podem revolucionar os métodos atuais da biomedicina.

# Acknowledgements

First of all, *Soli Deo Gloria*! It would be imposible to start this section saying any other words. I am grateful to God for providing me with everything that was necessary for the completion of this thesis: the family I was born in; the access to education; the friends he presented me; the wife he gave me and the knowledge of what it means to be a good and faithful servant. To be able to study the works of His hands and to obey the cultural mandate are things I will ever be grateful for.

Secondly, I must express my gratitude to Manuela, my wife. First, for taking time off college when the opportunity to move to Madrid arose; and later for the wholehearted support throughout my studies. The movie nights, the telepizzas, the struggle to speak Spanish, the trips, and the conversations I shared with her are certainly the fond memories I will forever have of this period of my life. Without the blessing of her companionship, I would not be able to complete this thesis.

I am particularly thankful for the support of my family (including the in-laws!). Even when I was on the other side of the ocean, they have made themselves present in every page of this work, showing support in every way they could. Every academic achievement of mine is a direct result of the great efforts put forth by my parents, Erasmo and Vaneide, since the day I was born.

As I promised him, a single paragraph will be dedicated to Dr. Ueslén Rocha, my "offstage" mentor. Not only has he shared many hours of work with me, but he has become a very good friend of mine. I am really thankful for his presence and the presence of his family in our lives. May God abundantly bless Uéslen, Valéria, Cecília (and the ones to come).

I am also grateful to my brothers and sisters from Libre Aceso in Madrid, the GrACE apologetics group at UFAL and the Castelo Forte Presbyterian Church in Maceió. It was a blessing to serve the Lord in their company.

I am also grateful to all my dear friends who were not necessarily work colleagues but that directly or indirectly contributed towards this PhD. In order to express my appreciation, I would like to mention three who, in a certain way, represent them all: Luis Felipe, Ebson and Walbert. It was a pleasure to play videogames with them whenever I got too tired. I wish them all joy in their lives and success in their careers!

A special thank you goes to my colleagues with whom I shared the office, lunchs, trips, equations, laughs, articles or even mice... Here I met many talented researchers, all gifted with a kindness that I will never forget. Among the ones I met in Spain are Patri, Emma, Dirk, Lucía, Paloma, Rui Yun, Hu Jie, Blanca, Irene, Laura and Antonio. Being myself a foreign newbie in the lab, they demonstrated some real patience with me. I am thankful for all the conversations that used to take place during our lunchtime (even if, in most of them, I wast just a listener). I am very fond of those memories. Among the ones I met in Brazil are Harrisson, Tasso, Michael, Jefferson, Wesley, Weslley, Janaína and Prof. Wagner. Thank you for all the scientific discussions we had and for sharing some laughs when talking about the dramatic life of a Brazilian investigator.

I appreciate the valuable assistance offered by the staff members of the School of Medicine of UAM, namely: Prof. Dr. María del Carmen Iglesias de la Cruz, Prof. Dr. Luis Monge, Prof. Dr. Francisco Sanz Rodríguez and specially Prof. Dr. Nuria Fernández. They always displayed professional competence and a great sense of humour. It has been a great satisfaction to work alongside them. I bet they never thought that I would miss drinking hot chocolate while watching mice getting anesthetized…

My doctoral scholarship was sponsored by brazilian agencies CAPES and CNPq, for which I am very appreciative. I am also thankful to COST for providing the financial support necessary to be part of UPCON in Wroclaw, Poland.

I am also indebted to Prof. Dr. José García Solé and Prof. Dr. Marcelo Lyra. Not only did they give me advice relating to scientific matters, but they also gave me a great deal of motivation to carry out my studies.

Finally, I would like to express my sincere sense of gratitude to my supervisors, Prof. Dr. Carlos Jacinto and Prof. Dr. Daniel Jaque, for dedicating both their time and experience. Prof. Dr. Carlos Jacinto has been an admirable mentor since the day I stepped my feet at UFAL. He has always believed in my potential and fought against bureaucracy so that I could have excellent (and yet very rare) academic opportunities. On the other side of the ocean, Prof. Dr. Daniel Jaque offered Manuela and myself the warmest welcome we could have ever expected. As a mentor, he knew exactly how to make high quality research an enjoyable task – something that anyone starting a scientific career would dream of. It was a great pleasure and honour to work under the guidance of such great men; the fruits of which I will benefit from for the rest of my career. I am very thankful for their level of care and friendship.

All of the names found on these pages not only brought meaning and joy to my scientific research, but also to my life outside the lab. And for that, I will be forever grateful…

# Abbreviations and symbols

BW – Biological window

BW-I – First biological Windows (650-950 nm)

BW-II – Second biological window (1000-1350 nm)

BW-III – Third biological window (1500-1800 nm)

EPR – Electron Paramagnetic Resonance

ET – Energy transfer

FIM – Fluorescence Imaging

IR – Infrared

LNThs – Luminescent nanothermometers

$l_p$ – Penetration Depth

NH - Nanoheater

NP – Nanoparticle

NThs - Nanothermometers

PBS – *Phosphate-buffered saline*

QD – *Quantum Dot*

SDTI – Subcutaneous dynamical thermal imaging

TEM – Transmission Electronic Microscopy

# Summary

# 1. Introduction

## 1.1. Main applications of luminescent materials in biomedicine

**Figure 1.1. Number of publications per year (as obtained with the Publish or Perish software up until 2017) in the fields of fluorescence imaging, luminescence thermometry and photothermal therapy.**

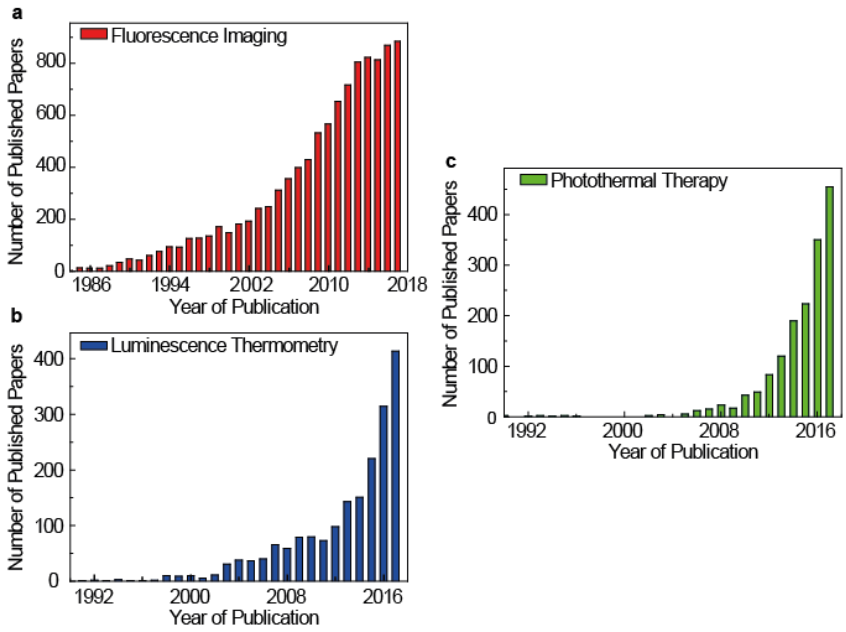


The development of nanotechnology has had a great impact on biomedical research by providing new perspectives on imaging, diagnosis and therapy and also by offering straightforward solutions to challenging problems that had remained unsolved for a long period of time (BRIGGER; DUBERNET; COUVREUR, 2002). In a very broad sense, nanotechnology highlights the design of nanoscale materials that offer specific responses when exposed to certain stimuli (SAJI; CHOE; YEUNG, 2010). Its remarkable applications in biomedicine is attributed to the fact that most biological systems have dimensions pertaining to the nanoscale — living organisms are built of cells whose parts are in the sub-micron size domain. When studying the practical side of nanomaterials, one can find a great number of size-dependent physical properties. The optical and magnetic

effects, however, stand out as the most exploited for biological applications (PANKHURST et al., 2003; PARAK et al., 2003).

Particularly, when dealing with optical effects, the nanomaterials should either fluoresce or change their optical properties. Given the current state of the scientific production, it is safe to say that at least three optical applications of nanomaterials in biomedicine draw the attention of the scientific community. They are namely (i) fluorescence imaging, (ii) luminescence thermometry and (iii) photothermal therapy (DEL ROSAL et al., 2016b; SALATA, 2004). This fact is reflected in the increasing number of publications per year, represented in **Figure 1.1**, whose main themes directly touch on each one of those three subjects. For this reason, we will briefly describe them in the following subsections.

### 1.1.1. Fluorescence Imaging

The design of the first fluorescence microscope in the early twentieth century was urged by the discovery of the fluorescence phenomenon by George G. Stokes in 1852. The potential of the technique, however, was not realized until Albert Coons labeled certain antibodies by means of a fluorescent system in the early 1940s. Since then, the continuous design of fluorophores with suitable properties for biomedical research (CHALFIE et al., 1994; PATTERSON; BOOTH; SABA, 2014) together with the constant evolution of modern microscope devices such as detectors, excitation sources, optical systems and analysis software have urged the improvement of the technique and lead to a phase of clinical applications in surgery and/or diagnosis. Furthermore, fluorescence imaging is already being used in regenerative medicine, in biodistribution and pharmacokinetic assays and in the study of neurodegenerative diseases (COWLES et al., 2013; PATTERSON; BOOTH; SABA, 2014).

When compared to other established imaging techniques, fluorescence imaging presents several advantages: relative simplicity, absence of ionizing radiations and cost-effective equipment. On the other hand, it also presents two

major drawbacks: (i) low penetration depth due to absorption and scattering of light in biological tissues and (ii) the intrinsic autofluorescence of the tissues (LEE et al., 2012; WEISSLEDER; PITTET, 2008). Nonetheless, those limitations become less relevant if one works with fluorescent labelers operating in certain ranges of the electromagnetic spectrum, specifically the so-called biological windows (BWs). **Figure 1.2a** demonstrates the tissue auto-fluorescence dependence with excitation and emission wavelengths. The auto-fluorescence is remarkably reduced when increasing the excitation and emission wavelength. Compared to the visible range, the signal emitted by tissues (790-830 nm) under infrared excitation (725-775) nm is minimal.

Not only the visible light overlaps with auto-fluorescence but is greatly absorbed by certain components of biological tissues, mainly hemoglobin and deoxyhemoglobin. This can be clearly seen in **Figure 1.2b**, which represents the absorption spectrum of a representative biological tissue (with water content and hemoglobin). For wavelengths shorter than 650 nm, absorption is very high which, in turns, results in minimal light penetration into biological tissues. In fact, the penetration depth ($p_d$) does not even reach the millimeter scale (BASHKATOV et al., 2005). To maximize $p_d$ it is necessary to use contrast agents whose excitation and emission bands are found in the infrared region. The BWs are indicated in **Figure 1.2b**, corresponding to the following spectral ranges: 750-950 nm (first biological window, BW-I), 1000-1350 nm (second biological window, BW-II) and 1500-1800 nm (third biological window, BW-III). In those regions, auto-fluorescence, scattering and absorption of light by biological tissues are minimized (JACQUES, 2013).

**Figure 1.2. Autofluorescence and absorption in biological tissues. (a)** ex vivo autofluorescence in three excitation and emission wavelength ranges of a mouse whose organs have been exposed after sacrifice. Figure adapted from (FRANGIONI, 2003). **(b)** Absorption coefficient of a representative biological tissue. The spectral ranges corresponding to the biological windows (BW-I, BW-II and BW-III) are indicated.

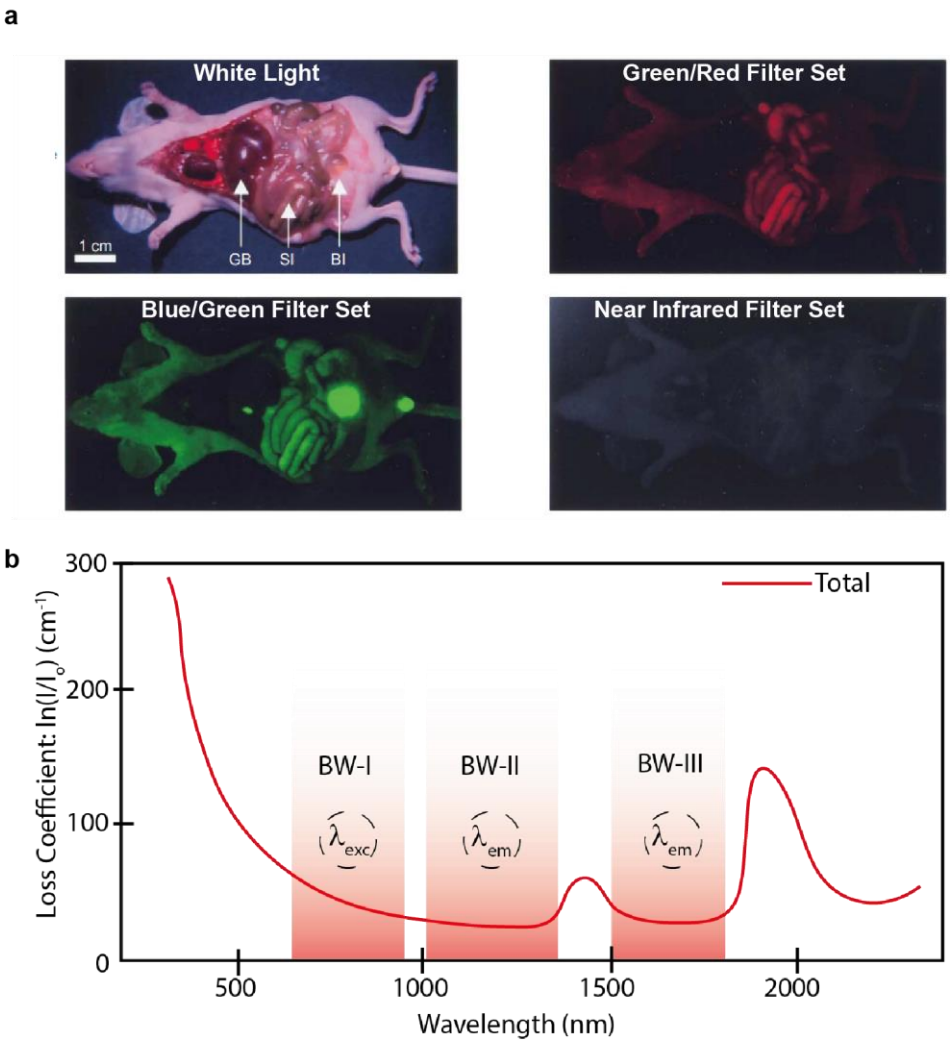


## 1.1.2. Luminescence thermometry

The second application, luminescence thermometry, is based on the use of luminescent nanoparticles (LNPs) whose spectroscopic properties (such as intensity, peak position, band shape, lifetime etc.) show appreciable temperature dependence in the physiological temperature range (10–50 °C) (BRITES et al.,

2012; WANG; WOLFBEIS; MEIER, 2013). In literature, those nanomaterials are commonly referred as luminescent nanothermometers (LNThs). Different fluorescent compounds, including organic dyes, fluorescent proteins and a large variety of NPs (metallic, dielectric doped with rare earth ions, QDs etc.) have a temperature-dependent emission and have been successfully used to perform thermal reading.

Luminescence thermometry is specifically sought in fields of science in which conventional (contact) thermometry cannot be applied. Microelectronics, integrated photonics and biomedicine are examples of such scientific fields (AIGOUY et al., 2005; ALLISON; GILLIES, 1997). But because of the vast number of important biochemical processes at a cellular level that are somehow connected to a temperature change, the application of LNThs in biomedicine became a goal that is wholeheartedly pursued by researchers in the whole world (MAESTRO et al., 2010b; OKABE et al., 2012; YANG; YANG; LIN, 2011; ZOHAR et al., 1998). Not limited to the cellular level, luminescence thermometry could also find applications in clinics as it is a potential tool for the diagnosis of some diseases, such as malignant tumors, inflammatory processes or cardiovascular pathologies (COLLINS et al., 1974; NG, 2009; TOUTOUZAS et al., 2009). Additionally, since temperature is a key parameter in photothermal therapies - as it will be described in detail in the following subsection - luminescence thermometry could also be useful in the control of the treatment. Even though different methods (including computerized tomography, ultrasound and magnetic resonance imaging) have already been used to control the temperature in such therapies (SACCOMANDI; SCHENA; SILVESTRI, 2013), LNThs present the advantage of being inexpensive and easy to implement, requiring only a suitable excitation source and a suitable detector to monitor emission in real time.

**Figure 1.3. Relative thermal sensitivity and operation spectral ranges of different LNThs.** Biological windows corresponding to the spectral ranges of maximum light penetration in tissues are represented in the graph as BW-I (first biological window, 650-950 nm), BW-II (second biological window, 1000-1350 nm) and BW-III (1500-1800 nm). The LNThs used throughout this thesis were highlighted in bold.

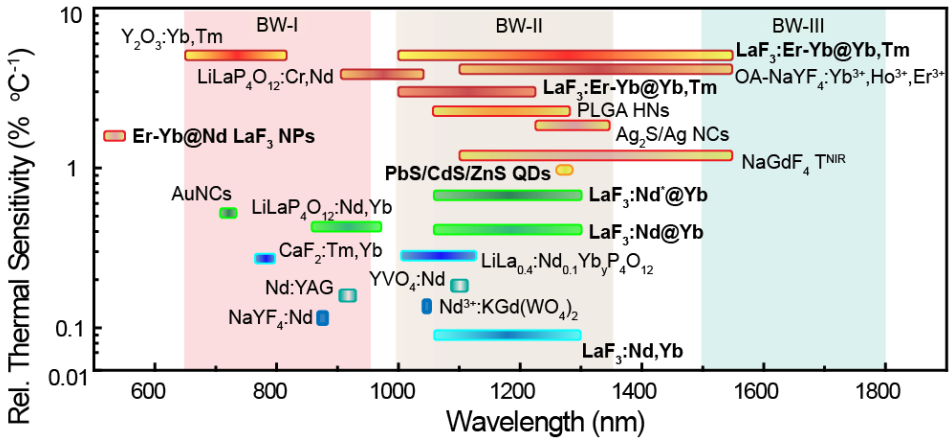


Despite the positive points and perspectives, *in vivo* applications of luminescence thermometry were very limited. This was due to the fact that most of the luminescent thermometers operated in the visible range, which, in turns, limited their application in animal models due to, as explained before, the low penetration depth of visible light in biological tissues. Thus, the first *in vivo* luminescence thermometry studies found in literature were performed on semitransparent organisms, including fly larvae (*D. melanogaster*) and nematodes (*C. elegans*). (ARAI et al., 2015; DONNER et al., 2013)

In recent years, however, numerous LNPs capable of operating in the BWs have been synthesized, some of which were temperature sensitive, as one can see in **Figure 1.3**. Where the relative thermal sensitivity, $S_r$, is defined as:

$$S_r = \frac{1}{\Delta}\left|\frac{d\Delta}{dT}\right| \quad \textbf{(Equation 1.1)}$$

Δ being the thermometric parameter (intensity, lifetime etc.)

We can see in **Figure 1.3** that there were several temperature-sensitive luminescent materials whose emissions lied in BW-I or BW-II. However, prior to the development of this thesis, neither the study of the thermal dynamics of a living animal nor the design of a LNTh capable of providing dynamic acquisition of subcutaneous thermal images (*i.e.* two-dimensional thermal reading) had been actualized. The first *in vivo* applications of infrared emitting nanothermometers for (i) the numerical estimation of basic properties of biological tissues, (ii) the detection of cardiovascular diseases and (iii) the recording of subcutaneous thermal videos in animal models were carried out in this thesis, as described in detail in Chapter 5.

### 1.1.3. Photothermal therapy

Thermal therapy consists of treating malignant tumors by producing irreversible damage to cancer cells while minimizing the effect on the surrounding and healthy tissues. This is done by increasing the temperature in a well-defined location of the tissue. Its effects depend on both the magnitude and the duration of the temperature increment, as shown in Figure 1.4, which summarizes the main effects of treatments at different temperatures. For values lower than 41 °C no cellular damage occurs. Irreversible damage requires long exposures (longer than 1 hour) at moderate temperatures (41-48 °C) or shorter exposures (4-6 minutes) at higher temperatures (48-60 °C). This latter temperature range, known as the thermal ablation range, is the one that is generally used in tumor therapy treatments. Therapy can also be used as an adjunct to conventional treatments (radiation therapy, chemotherapy). In this case, one usually works at lower temperatures (41-48 ° C, corresponding to the range of hyperthermia indicated in **Figure 1.4**). (CHICHEŁ et al., 2007; TAKAHASHI et al., 2002)

Although the possibility of treating tumors using thermal therapy has been known for decades, these types of treatments have regained interest as nanotechnology developed. By locating nanoheaters inside a tumor, it is possible

to perform a minimally invasive treatment, something impossible for traditional heating systems (radiofrequency, microwave and ultrasound). Even though the ability of magnetic nanomaterials to treat tumors in a non-invasive way has been widely demonstrated in numerous *in vivo* experiments, the fast development of synthesis methods has led to the appearance of a large number of materials capable of generating heat under optical excitation. As a result, photothermal therapy has attracted a great deal of attention by the scientific community in the last decade.

**Figure 1.4. Biological effects of heating procedures.** Summary of the main effects of thermal therapies on treated tissues. Commonly used ranges for thermal therapy alone (thermal ablation, 48-60 °C) and in combination with conventional treatments (hyperthermia, 41-48 °C) are indicated.

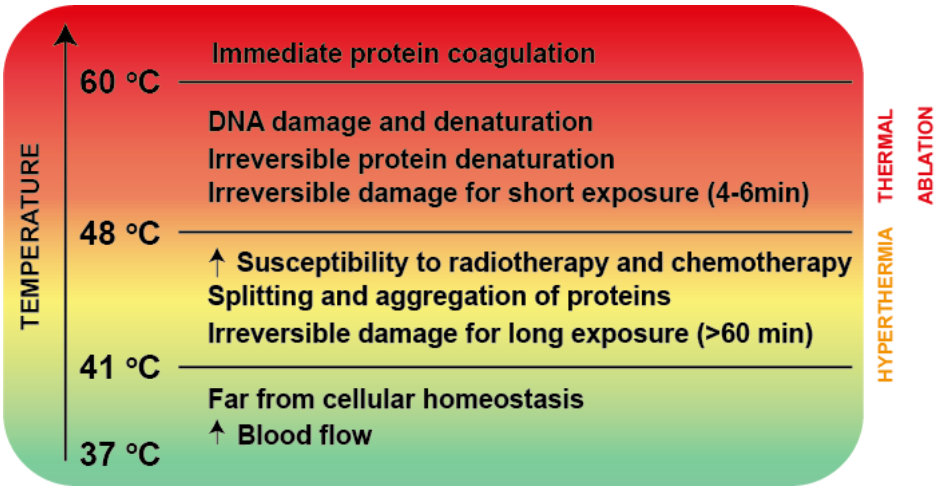


The main advantage of photothermal therapy is its simplicity in operation and its low cost, while its main limitation lies in the low penetration of light into the tissues. This problem, as we have stated before, can be overcome by operating with photothermal agents that can be excited within the BWs. Additionally, in order to be a good photothermal agent, the nanomaterial must also have a high photothermal conversion efficiency (η). This is defined as the fraction of energy absorbed (under a certain excitation wavelength) that is re-emitted as heat. Currently, there is a great variety of nanomaterials with high photothermal conversion efficiencies reported, including carbon

nanostructures, semiconductors, organic NPs and hybrid systems in which various types of materials are combined. In terms of their applications in animal models, different NPs, among them gold nanostructures, carbon nanotubes and graphene NPs have demonstrated their potential to treat tumors effectively in animal models (JAQUE et al., 2014a). They have also been successfully used in combined therapies (photothermal therapy + chemotherapy or radiotherapy) in animal models (HAINFELD; SLATKIN; SMILOWITZ, 2004; SHEN et al., 2013).

Since the net effects caused on cancer tumors during PTTs strongly depend on both the magnitude of the heating as well as the treatment duration (DEWEY; DIEDERICH, 2009; HABASH et al., 2006; HILDEBRANDT et al., 2002; JOHANNSEN et al., 2005; MARMOR et al., 1979), in order to achieve an efficient treatment and keep the collateral damage at minimum it is extremely necessary to have a temperature reading during NP-based PTTs. In order to do this, infrared thermography is commonly used in most *in vivo* experiments. This particular method has several advantages, such as simplicity, low cost and relative precision (around 1 °C) but its major drawback is that it only provides information about the surface thermal status. There is no guarantee, however, that the surface temperature corresponds to the one inside the tumor, especially if one considers the presence of heating NPs, blood perfusion and various heat dissipation mechanisms on the surface and in the treated areas. Aiming to overcome this limitation, an increasing interest in the design of multifunctional luminescent NPs capable of simultaneous heating and thermal sensing under single power excitation has emerged as they would constitute significant building blocks towards the achievement of real controlled PTTs (XIMENDES et al., 2016b). Obviously the most direct way to produce such multifunctional agents consists in the combination of two nanosized elements in a single nanostructure: one of them acting as a heating nanoparticle and the other providing the thermal sensing capacity (*i.e.* acting as a thermometer). This "double particle" approach was already successfully adopted by combining metallic or magnetic NPs (as heating units) with rare earth doped nanocrystals

(as thermal sensors). Despite the good results obtained, the use of two physically linked nanostructures increases the complexity of the system and compromises their long-term stability (BRITES et al., 2012; HUANG et al., 2015; JAQUE; VETRONE, 2012). Additionally, only a few of them show real potential of working subcutaneously.

Therefore, the second goal of the work developed in this thesis, as presented in Chapter 4, was to use single NPs capable of acting as multifunctional agents (heaters and thermometers). Once we introduced this concept, we dealt with the problem of subcutaneous thermal reading by producing a multifunctional NP with thermosensitive fluorescence emission lying in the BW-II. The properties and foundations of those NPs, as well as of the other NPs studied throughout this doctoral thesis, will be further described in Chapter 2.

## 1.2. Pre-tailoring NPs properties by means of core/shell engineering

The synthesis of nanoparticles constitutes one of the many important sections of nanotechnology. In fact, if one looks into the current state of the scientific production, one will find numerous synthesis techniques destined to produce different kinds of nanoparticles. To generalize all these techniques would be rather difficult - if not impossible - but in terms of results one can safely say that, by using them, not only pure nanoparticles are being synthesized but also hybrid or coated nanoparticles (with hydrophilic or hydrophobic materials depending on the intended application).

Initially the scientific community focused on single nanoparticles because of their better properties when compared to bulk materials. However, between the late 1980s and the early 1990s, it was discovered not only that composite, heterogeneous or sandwich particles had better efficiency than their corresponding single particles but also that some of their properties could be improved by synthesizing concentric multilayer semiconductor nanoparticles.

From this point forwards, the terminology "core/shell" was adopted (HOENER et al., 1992; HONMA; SANO; KOMIYAMA, 1993; ZHOU et al., 1994). Due to the many demands of nanotechnology for more and more advanced materials and the simultaneous advancement of characterization techniques, there has been a gradual establishment of the structures known as core/shell nanoparticles. A statistical data analysis is presented in **Figure 1.5** to show the increasing trend of published research papers in this area. The data was collected in 2018 by means of the *Publish or Perish* software.

**Figure 1.5. Publications per year for core/shell nanoparticles during the period 1994 to 2017 (Data collected from the *Publish or Perish* software database).**

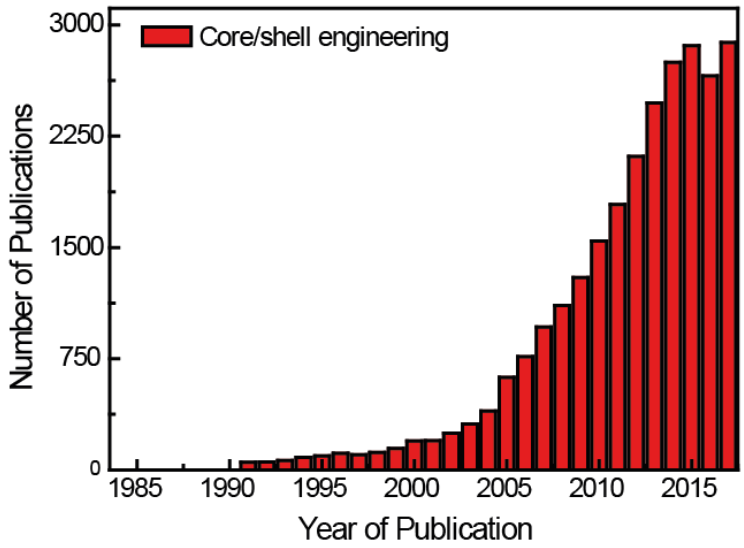


In general terms, the distinction between simple and core/shell nanoparticles is given by what follows: the formers are made of a single material whereas the latter, as the name implies, are composed of two or more materials. The core/shell type can be broadly defined as having a shell (outer layer material) and a core (inner material) which, in turns, are in close interaction and may consist of different combinations, such as inorganic/inorganic, inorganic/organic, organic/inorganic, and organic/organic materials. The choice

of material for the shell strongly depends on the end application. In **Figure 1.6**, two different classes of core/shell nanoparticles are depicted. The most common ones, concentric spherical core/shell nanoparticles (**Figure 1.6a**), have a simple spherical core particle completely coated by a shell of a different material. Concentric nanoshells, on the other hand, have alternate compositions (A/B/C type) as shown in **Figure 1.6b**.

The reason for all the attention given to core/shell nanoparticles is that they have emerged at the frontier between materials chemistry and many diversified areas such as electronics, biomedicine, optics and catalysis. Sometimes properties arising from either core or shell materials can be quite different. This, in turns, allows for the modification of the NPs properties by changing either the constituent materials or the core-to-shell ratio. The purposes for the existence of the shell (or shells) are manifold: surface modification, ability to increase the functionality, stability, and dispersibility, controlled release of the core, reduction in consumption of expensive materials etc. (CARUSO, 2001)

**Figure 1.6. (a)** spherical core/shell nanoparticles; **(b)** core/shell/shell nanoparticles.

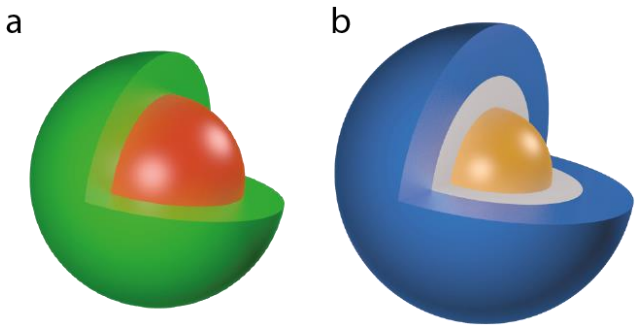


With this in mind, one can of course propose the core/shell engineering as a method to overcome all the problems discussed in Section 1.1. This was in fact the main motivation for using core/shell nanoparticles in the investigation performed throughout this thesis. Prior to its development, several problems and serious impediments had remained in the fields of photothermal therapy and luminescence thermometry. These problems are correspondingly

summarized in **Figure 1.7**. Firstly, luminescence thermometry lacked the design of highly sensitive LNThs operating in BW-II and/or BW-III which, in turns, made the study of subcutaneous *in vivo* thermal dynamics a rather difficult task - not to mention the achievement of a subcutaneous thermal video recording. Secondly, photothermal therapy lacked the presence of multifunctional NPs capable of acting as heaters and thermometers simultaneously. This impediment also made the control of the treatment a rather difficult task. Thus, the main goal of this thesis was to propose the core/shell engineering as a reliable method to overcome the aforementioned problems.

**Figure 1.7. Impediments (and proposed solutions) in the fields of luminescence thermometry and photothermal therapy.**

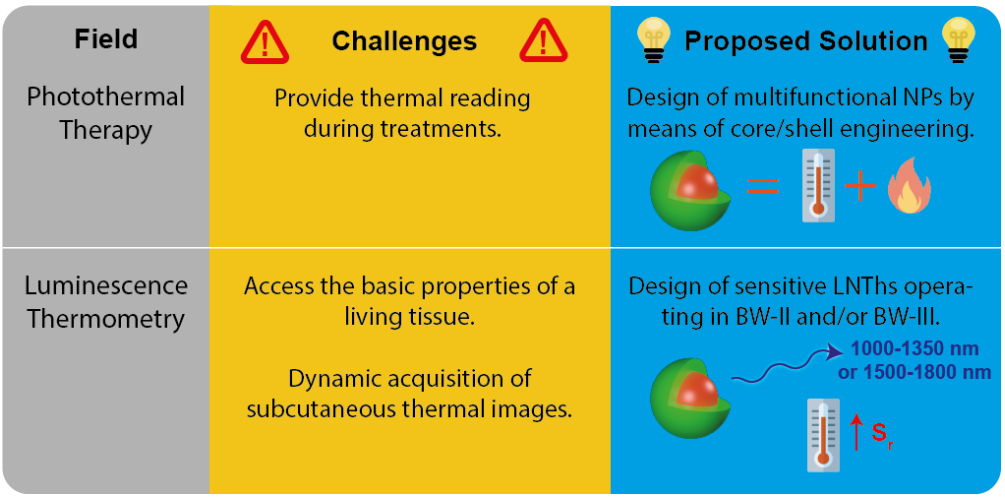

# 2. Fundamental Concepts

In this chapter we will briefly describe the main characteristics of the NPs studied throughout the thesis (core/shell NPs doped with rare-earth ions and QDs of PbS/CdS/ZnS) and the physical processes behind their interaction with biological tissues. We will specifically focus our attention on the properties that convert these nanomaterials into systems of special interest for thermal sensing applications in biomedicine and on the governing equations for the different physical processes involved.

## 2.1. Heating nanoparticles

The battle against cancer is continuously bringing about new challenges that can only be overcome if faced from a multidisciplinary point of view. Among the different ongoing research areas focusing on cancer, we can safely say that nanotechnology is standing out by the development of new materials and techniques that would improve its detection and therapy (FERRARI, 2005; NIE et al., 2007). If, at a certain moment in the past few years, only NPs with large quantum yields (QYs) were desired, as they would operate as good luminescent probes, today we can also find applications for LNPs with low QY. In fact, when a LNP has a low QY, a great fraction of the excitation radiation is transformed into heat and the NP behaves as a nanoheater (NHs) (HENDERSON; IMBUSCH, 1989). This is, for example, the case of gold nanoparticles (GNPs) and Carbon Nanotubes (CNTs) that have been extensively used as photothermal agents for both *in vitro* and *in vivo* experiments (ELSAYED; HUANG; ELSAYED, 2006; MOON; LEE; CHOI, 2009). The fact that many authors had already reported on successful laser-induced tumor treatment by using NHs led the scientific community to seriously consider nanoparticle-based PTTs as an actual alternative therapy against cancer.

### 2.1.1. Heat generation in $Nd^{3+}$-doped nanoparticles

A recent but nonetheless important demonstration of heating by LNPs is found in the $Nd^{3+}$-doped $LaF_3$ NPs. The physical principle behind this system is found in the role of the concentration of optically active ions on the properties of

rare earth doped NPs. In fact, it has been experimentally shown that for NPs of identical size, both fluorescence intensity and lifetime present a meaningful dependence with the concentration of dopant ions (and $Nd^{3+}$-doped $LaF_3$ NPs are no exceptions). In general, it is observed that the fluorescence intensity of nanocrystals doped with $Nd^{3+}$ ions increases with $Nd^{3+}$ concentration but only up to a certain value, from which additional increases result in a decrease of intensity. Additionally, it was observed that the average fluorescence lifetimes monotonously decreased with the concentration of dopant ions within the NPs. This is because, by increasing the amount of $Nd^{3+}$ ions in the crystalline matrix, the distance between them is reduced and the energy transfer processes become more relevant (HENDERSON; IMBUSCH, 1989).

**Figure 2.1. Schematic representation of energy transfer processes between Nd3+ ions. (a)** Radiative and non-radiative de-excitation processes of free $Nd^{3+}$ ions **(b)** Cross-relaxation process between two adjacent $Nd^{3+}$ ions. **(c)** Energy migration process between $Nd^{3+}$ ions, which ends in a non-radiative de-excitation from a non-emitting center.

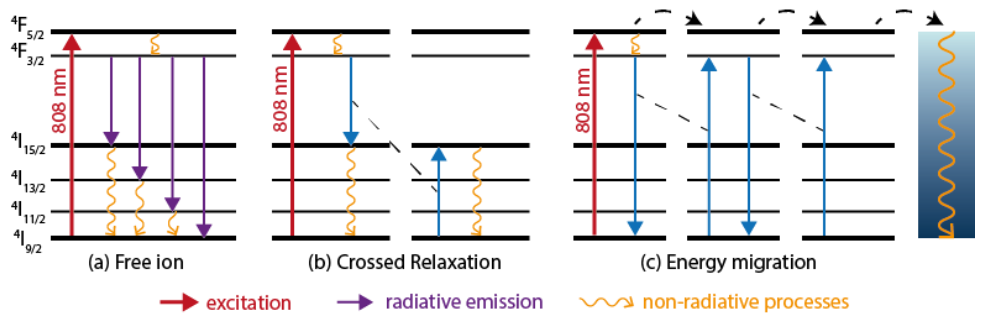


**Figure 2.1** contains the schematic representation of (i) the possible de-excitation processes of a free $Nd^{3+}$ ion when excited from the ground state up to the $^4F_{5/2}$ level by an 808-nm wavelength radiation and (ii) the energy transfer processes between ions of same-species, which can be of two types: crossed relaxation (**Figure 2.1b**) and energy migration (**Figure 2.1c**). We see in this figure that, for the case of an isolated ion, non-radiative de-excitation processes occur through the emission of phonons, which implies in heat generation in the system. Both the transition between the excited state and the metastable state from which the radiative emissions occur ($^4F_{5/2} \rightarrow {}^4F_{3/2}$) and the transitions between

the final states of the radiative processes $^4I_J$ (J = 15/2, 13/2, 11/2) and the ground state $^4I_{9/2}$ take place in non-radiative manner. This indicates that, even in the case of NPs doped with a low concentration of $Nd^{3+}$ ions, a certain generation of heat will occur under optical excitation. The energy transfer processes also provide additional mechanisms of non-radiative de-excitation:

- In the case of cross-relaxation processes between two $Nd^{3+}$ ions, which are schematically represented in **Figure 2.1b**, the $^4F_{3/2} \rightarrow {}^4I_{15/2}$ de-excitation of one of them is achieved through the excitation of the other from the ground state ($^4I_{9/2}$) to the state $^4I_{15/2}$. Both ions are then de-excited through multiphonon processes to the ground state.
- The energy migration processes consist, as shown in **Figure 2.1c**, in the relaxation of one of the ions by transferring its energy to an adjacent ion. This energy transfer between nearby ions continues until a non-radiative center is reached (usually associated with host defects), which is de-energized by heat generation. The greater the presence of this type of defects in the surface of materials, the more relevant are these processes for nanometric systems (QUINTANILLA et al., 2013). Additionally, in the case of NPs dispersed in aqueous media, which is the case of the systems used in this thesis, it is necessary to take into account the interactions between the optically active ions located on the surface and the solvent molecules. In this aspect, the hydroxyl groups (-OH) play a significant role due to the high energies of vibrational, so that the $Nd^{3+}$ ions can be de-excited by a non-radiative interaction with them (KUMAR et al., 2007; ORLOVSKII et al., 2013). The NPs doped with a high concentration of $Nd^{3+}$ ions will therefore present a high probability of energy transfer processes due to the small distance between ions. These processes will frequently result in non-radiative de-excitations both within the NP and its surface and in the subsequent production of heat.

The relevance of energy transfer processes in the case of NPs heavily doped with $Nd^{3+}$ ions is found in the decrease of the quantum yield, Φ, of their emitting level, which basically states the connection between the number of emitted photons and the number of absorbed photons. This indicates that the higher the proportion of doping ions, the greater the ability of heat generation by $Nd^{3+}$ doped NPs. Indeed, this was experimentally shown in $LaF_3$:$Nd^{3+}$ and $NaYF_4$:$Nd^{3+}$ NPs (doped with molar percentages in the 1-25% range) (BEDNARKIEWICZ et al., 2011; ROCHA et al., 2014a). For this reason, Chapter 4 explores NPs with high concentrations of $Nd^{3+}$ ions.

## 2.2. Luminescent thermometers

As briefly stated in the introduction, luminescence thermometry is based on the use of LNPs whose spectroscopic properties show appreciable temperature dependence in a certain range of interest. Historically, three main types of LNThs were used to determine temperature: (i) LNThs based on emission intensity, using the integrated intensity of a single transition or of a pair of transitions, (ii) LNThs based on the spectral shift of a given transition and (iii) lifetime based LNThs, using the decay profiles of emitting excited states (**Figure 2.2**).

**Figure 2.2. Classification of luminescent thermometers.**

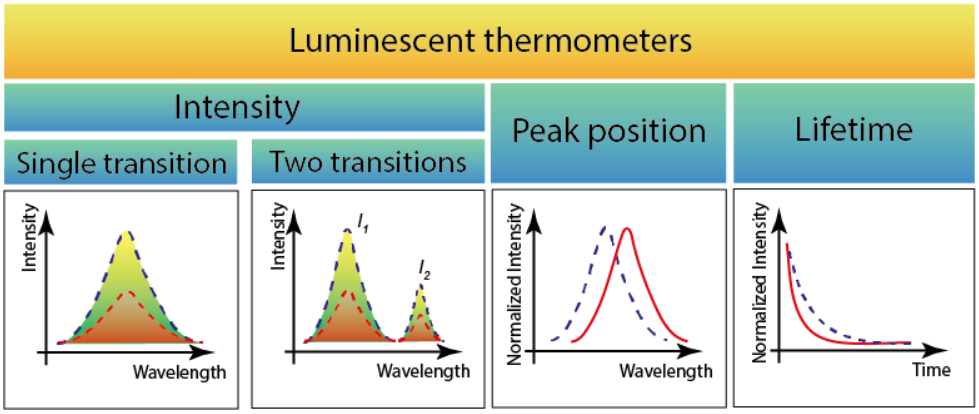


All the LNThs used throughout this thesis belonged to the first category. With the exception of PbS/CdS/ZnS QDs and Er-Yb@Nd $LaF_3$ NPs, the LNThs

here developed were based on the emission intensities of transitions of at least two different emitting centers. This, in turns, resulted in a reduction of the critical dependence of their performance on fluctuations of illumination or phosphor concentration (KUSAMA; SOVERS; YOSHIOKA, 1976; MIKKELSEN; WALLACH, 1977). As a complementary comment, it is worth noticing that even though lifetime-based sensing methods would not suffer from such disadvantages, they would instead require longer acquisition times, postprocessing techniques and a complex instrumentation (BERTHOU; JÖRGENSEN, 1990; BRITES et al., 2012; PENG; HUANG; WOLFBEIS, 2010). Thus, the path to *in vivo* applications would present a lot of impediments.

With the exception of Er-Yb@Nd $LaF_3$ NPs, whose thermal reading could be fully described in terms of optical parameters, the other LNThs here developed had to be referred to a well-known temperature for their calibration (BRITES et al., 2012). The usual calibration procedure requires an independent measurement of the temperature (using, for example, a heating plate or a thermographic infrared camera) in order to relate it to its thermometric parameter (in this case, luminescence intensity or luminescence intensity ratio). The necessity of an independent measurement of temperature, in turns, implies in a new calibration procedure for every new medium the thermometer will operate in. However, since this is not always possible to achieve, a calibration performed on a very similar medium is often assumed to be valid. When using the Er-Yb@Nd $LaF_3$ NPs, on the other hand, one did not need to make this assumption as the calibration factor depended on easily obtainable spectroscopic quantities which, in turns, did not have any dependence with the medium (see subsection 2.2.1).

In order to present the physical mechanisms behind the thermal sensing capability of the NPs produced throughout this thesis, the section will be divided into three subsections: (i) thermal response rationalizing of single-center emission, (ii) thermal response rationalizing of dual-center emissios, (iii) QDs for luminescence thermometry.

### 2.2.1. Thermal response rationalizing of single-center emission

The emission intensity ratio of two distinct transitions from the same emitting center provides a robust approach for temperature measurement. The working principle is described in what follows.

**Figure 2.3. Schematic energy-level diagram of the three-level model of a typical luminescent ion. $W_{10}$ is the absorption rate from the ground state $|0\rangle$ to state $|1\rangle$.**

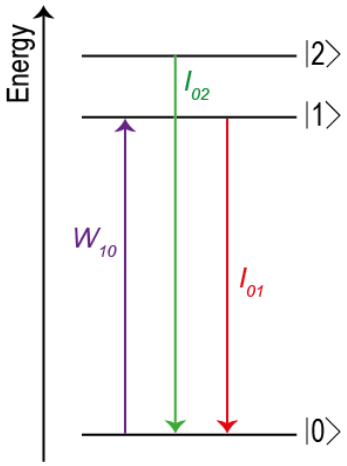


The ratio of two emission intensities, with close energies, can be rationalized assuming the simplest model of Boltzmann thermal equilibrium between two emitting states, $|1\rangle$ and $|2\rangle$ (see **Figure 2.3**). Let $I_{0i}$ be the emission intensity of the $|i\rangle \rightarrow |0\rangle$ transition (i=1 or 2). Its value can be estimated by (BRITES; MILLÁN; CARLOS, 2016):

$$I_{0i} \propto \hbar\omega_{0i} A_{0i} N_i$$

**Equation 2.1**

where $A_{0i}$ and $\omega_{0i}$ are, respectively, the total spontaneous emission rate and the angular frequency of the $|i\rangle \rightarrow |0\rangle$ transition, and $N_i$ is the population of the $|i\rangle$ state. If these two levels are thermally coupled (*i.e.,* the energy difference is of the order of the thermal energy), $N_1$ and $N_2$ are related by:

$$\frac{N_2}{N_1} = g_2 \, exp\left(-\frac{\Delta E}{k_B T}\right) / g_1$$

**Equation 2.2**

where $g_i$ is the degeneracy of the $|i\rangle$ level, $\Delta E$ is the energy difference between the barycenters of the $|2\rangle$ and $|1\rangle$ emission bands and $k_B$ is the Boltzmann's constant. The ratio, $R$, between the $|2\rangle \rightarrow |0\rangle$ and $|1\rangle \rightarrow |0\rangle$ emission intensities is then given by:

$$R = \frac{I_{02}}{I_{01}} = \omega_{02} A_{02} N_2 / \omega_{01} A_{01} N_1 = B\, exp\left(-\frac{\Delta E}{k_B T}\right)$$

**Equation 2.3**

where B is a constant.

Traditionally, in order to consider two emitting levels as thermally coupled, the value of $\Delta E$ has to be found in the 200-2000 $cm^{-1}$ range. These empirical limits guarantee both the spectral separation of the levels and the existence of thermalization. From equation **Equation 2.3**, the absolute temperature is estimated from:

$$T = \frac{\Delta E}{k_B} \frac{1}{\ln\left(\frac{B}{R}\right)}$$

**Equation 2.4**

in which $\Delta E$ is calculated using the formal definition of the barycenter of a $J$–$J'$ transition or by fitting the envelope of the $I_1$ and $I_2$ transitions (BALABHADRA et al., 2015). The constant $B$, on the other hand, is determined from the extrapolation of the $R$ vs pump power curve to the limit of zero pump power which, in turns, corresponds to room temperature (CARLSON; KHAN; RICHARDSON, 2011; DEBASU et al., 2013).

The most common example of thermally dependent single-center emissions is found in the rare-earth based ratiometric thermometers comprising $Yb^{3+}$ ions as sensitizers and $Er^{3+}$ ions as upconverter activators (ALENCAR et al., 2004; MAESTRO et al., 2010a; SAVCHUK et al., 2015; SEDLMEIER et al., 2012; SINGH; KUMAR; RAI, 2009; VETRONE et al., 2010a). This two-photon process occurs via

energy transfer from $Yb^{3+}$ ions to the fluorescent $Er^{3+}$ ions. The $Er^{3+}$ ions are excited to their $^4F_{7/2}$ state via two successive energy transfers from $Yb^{3+}$ ions in close proximity, promoting them from their ground state ($^4I_{15/2}$) to an intermediate state ($^4I_{11/2}$) and subsequently to the excited state ($^4F_{7/2}$). It is a well-known fact that the $Er^{3+}$ green emission consists of two distinct bands between 515 and 55 nm (centered at 525 nm) and 535 and 570 nm (centered at 545 nm) emanating from transitions from two excited states ($^2H_{11/2}$ and $^4S_{3/2}$, respectively) to the ground state (**Figure 2.4**). Since those two states are thermally coupled, they are governed by **Equation 2.4**. In Section 4.1, we put some complexity into this system by inserting a heavily $Nd^{3+}$-doped shell in order to have $Nd^{3+}$ions as sensitizers instead of $Yb^{3+}$. This, in turns, allows the use of an excitation wavelength around 808 nm and turns $Yb^{3+}$ ions into bridges towards the activators, *i.e.*, $Er^{3+}$ ions. The working principles of thermometry with $Er^{3+}$ green emission, nonetheless, remain the same.

**Figure 2.4. Simplified energy level diagram showing the relevant states of the $Yb^{3+}$ and $Er^{3+}$ ions and the two-step up conversion excitation mechanism.** The temperature sensitivity of the NaYF4:$Er^{3+}$,$Yb^{3+}$ NPs occurs as a result of the closely spaced $^2H_{11/2}$ and $^4S_{3/2}$ energy states.

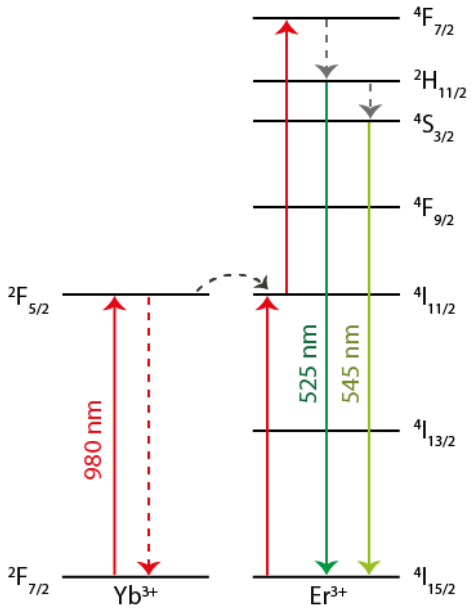

### 2.2.2. Thermal response rationalizing of dual-center emissions

For some rare-earth-based luminescent thermometers utilized in this thesis, the thermometric parameter involved the intensity ratio between two transitions belonging to two different emitting centers. In those systems, two $Ln^{3+}$ ions could be indistinguishably employed as the probe or the reference and ion–ion energy transfer regulated the intensity ratio variations.

Similar to what was described in Section 2.2.1, it is also possible to rationalize the emission intensity ratio, *R(T),* dependence for dual-center-based LNThs. In order to do so, it is necessary to use the extended classical Mott–Seitz model (MOTT, 1938; SEITZ, 1939) developed by Cooke and co-authors (COOKE et al., 1998, 2004). This model describes the total transition probability of an emitting level by the sum of radiative and nonradiative transition probabilities ($A_R$ and $A_{NR}$, respectively) which, in turns, can be evaluated by the inverse of the lifetime $\tau$ of the emitting level:

$$\tau = \frac{\tau_0}{1 + \sum_i \alpha_i \, exp\left(-\frac{\Delta E_i}{k_B T}\right)}$$

**Equation 2.5**

where $\tau_0$ is the lifetime intensity at $T = 0\ K$, $\alpha_i$ is the $A^i_{NR}/A_R$ ratio for the i-th quenching process and $\Delta E_i$ is the activation energy of the same thermal quenching process. The integrated luminescence intensity, *I*, may be related with equation Equation 2.5 by (BRITES; MILLÁN; CARLOS, 2016; DUARTE et al., 1999; STALDER; BASS; CHAI, 1992):

$$\frac{I}{\Gamma_0} = \frac{\tau}{\tau_0}$$

**Equation 2.6**

where $\Gamma_0$ is the beam intensity at T = 0 K. Combining **Equation 2.5** and **Equation 2.6**, one arrives at:

$$I = \frac{\Gamma_0}{1 + \sum_i \alpha_i \exp(-\Delta E_i / k_B T)}$$

**Equation 2.7**

Therefore, if a system has two emitting centers, the luminescence intensity ratio must be given by:

$$R = \frac{I_1}{I_2} = \frac{\Gamma_{01}}{\Gamma_{02}} \frac{\left(1 + \sum_i \alpha_i^{(2)} \exp\left(-\Delta E_i^{(2)} / k_B T\right)\right)}{\left(1 + \sum_i \alpha_i^{(1)} \exp\left(-\Delta E_i^{(1)} / k_B T\right)\right)}$$
$$= R_0 \frac{\left(1 + \sum_i \alpha_i^{(2)} \exp\left(-\Delta E_i^{(2)} / k_B T\right)\right)}{\left(1 + \sum_i \alpha_i^{(1)} \exp\left(-\Delta E_i^{(1)} / k_B T\right)\right)}$$

**Equation 2.8**

where $R_0$, $\alpha^{(1)}{}_i$, $\alpha^{(2)}{}_i$ stand for the ratio between the non-radiative and radiative probabilities of the i-th deactivation channel of transitions with intensity $I_1$ and $I_2$, while $\Delta E^{(1)}{}_i$ and $\Delta E^{(2)}{}_i$ are the activation energies for the thermal quenching process of transitions with intensity $I_1$ and $I_2$, respectively.

By observing **Equation 2.8** one can easily wonder if, in some cases, it would actually be viable to identify how many non-radiative and radiative probabilities are involved. This problem is, of course, avoided if one is not mainly interested in knowing the values of $\alpha_i$ but instead in the general thermal dependence of $R$. Usually the investigator finds a temperature interval in which $R$ presents a linear (or quasi-linear) behavior and then calculates its thermal sensitivity (defined in detail in the next subsectin 2.2.4). Finding this interval is always possible since, according to **Equation 2.8**, $R$ has an asymptotic value when $T \rightarrow \infty$. This means that there will always be a region where $dR/dT$ will be approaching zero. The pace of this approaching, however, decreases as T approaches infinity. Its value, therefore, can be reasonably considered as a nonzero constant. The limits of this interval are going to depend on the values of $\alpha_i$ and $\Delta E_i$. Thus, they can only be estimated by means of experiments. With the exception of Er-Yb@Nd $LaF_3$ NPs, all LNTh calibration curves were assumed to be linear in the physiological

temperature range. This assumption not only facilitated the discussions but was also supported by experimental results.

### 2.2.3. QDs for luminescence thermometry

Prior to the development of this thesis, the possibility of using QDs as luminescent thermometers had already been demonstrated (WALKER et al., 2003). The analysis of the fluorescence generated by QDs allowed the detection of temperature variations thanks to the thermal sensitivity of their emission intensity, lifetime and peak position (JAQUE GARCÍA; GARCÍA SOLÉ, 2015).

The thermal sensitivity provided by the analysis of their emission intensity, however, allows us to achieve thermal sensing by means of a much simpler experimental apparatus. The temperature induced variation of emission intensity in QDs has been studied in a great variety of systems, including simple QDs, core/shell and core/shell/shell QDs (ANDREAKOU et al., 2013; JING et al., 2009; VALERINI et al., 2005). The thermal dependence of emission intensity is not uniform but varies with temperature range. For instance, in the case of PbS (simple) QDs, three well-defined ranges can be distinguished: for temperatures between 180 and 250 K, the intensity increases with increasing temperature, while for temperatures below 180 K or greater than 250 K, it decreases (ANDREAKOU et al., 2013). In this thesis, the interest in the thermal sensitivity of the QDs is limited to the range of temperatures relevant for biomedical applications. In this range, a reduction in fluorescence intensity (quenching) is generally observed with increasing temperature, which indicates an increase in the probability of non-radiative exciton recombination at higher temperatures (WALKER et al., 2003).

This increase in the probability of non-radiative recombination with increasing temperature (within the physiological range) can be attributed to two mechanisms: entrapment of charge carriers in trapping states and thermal escape of charge carriers in phonon-assisted processes, specifically, longitudinal optical phonons (KLIMOV; BOLIVAR; KURZ, 1996; YANG et al., 1997). Taking

these two processes into account, the temperature dependence of the emission intensity of QDs, *I(T)*, can be expressed as:

$$I(T) = \frac{I_0}{1 + A(e^{-E_a/k_B T}) + B(e^{E_{LO}/k_B T} - 1)^{-m}}$$

**Equation 2.9**

where $I_o$ is the emission intensity at 0 K, $E_a$ stands for the activation energy of the trapping states and *m* is the number of longitudinal optical phonons. The constants A and B indicate the probabilities of the non-radiative relaxation processes (VALERINI et al., 2005).

By fitting the experimental data, obtained for the emission intensity as a function of temperature, to **Equation 2.9**, one can study the relevance of each one of these processes for different types of QDs (MORELLO et al., 2007; VALERINI et al., 2005). The actual values of those parameters depend both on the composition of the QD as well as its structure and size. For core/shell and core/shell/shell QDs, the thickness of the shells also play an important role in the non-radiative processes (JING et al., 2009).

Additionally, it has been demonstrated that QDs thermal quenching is only reversible in a certain range of temperature. Thus, if one exceeds a threshold temperature ($T_q$), the loss in fluorescence is irreversible. This process has been exhaustively studied in core/shell/shell QDs of CdSe/CdS/ZnS and in core/shell QDs of CdTe/CdSe dispersed in liquid solvents as well as in solid hosts (ZHAO et al., 2012). The authors attributed the thermal quenching irreversibility (for temperatures higher than $T_q$) to structural changes in QDs which, in turns, lead to the creation of permanent trapping states. For temperatures below $T_q$, the charge carriers can be kept in previously existing trapping states or in thermally created trapping states that can relax with decreasing temperature. This, in turns, makes quenching a totally reversible process. The authors also observed that both the temperature induced intensity variation and the value of $T_q$ were strongly not only with the type of QDs but also with the medium they were

dispersed. In fact, a more perceptible thermal quenching and a much lower value of $T_q$ were observed for CdSe/CdS/ZnS QDs dispersed in liquid medium than when dispersed in a solid host. This result can be attributed to the appearance of superficial defects due to the loss of ligand molecules coating the surface of QDs which, in turns, cannot occur for QDs dispersed in solid hosts (BULLEN; MULVANEY, 2006).

Taking into account the wide variety of factors possibly altering the thermal sensitivity of the QDs, when it comes to using them for luminescent thermometry, it is especially important to calibrate the thermal dependence of the fluorescence over the entire temperature range of interest through repeated ramps of cooling and heating. Also, it is critical to perform the calibration with the dispersed QDs in the medium in which they will be used to consider the possible effect of the environment on the thermal sensitivity.

### 2.2.4. Performance of luminescent thermometers

Here the main parameters utilized in the quantification of performance of ratiometric LNThs will be presented. The comparison between distinct LNThs is made using the following:

#### *2.2.4.1. Relative thermal sensitivity*

The relative thermal sensitivity, $S_R$, stands for the relative change of $R$, the thermometric parameter, per degree of temperature change and is defined as:

$$S_R = \frac{1}{R}\left|\frac{dR}{dT}\right|$$

**Equation 2.10**

This parameter is usually expressed in units of % change per Kelvin (or Celsius), % $K^{-1}$. Compared to the absolute thermal sensitivity, $S_a = dR/dT$, $S_R$ presents the advantage of being independent of the thermometer's nature.

*2.2.4.2. Temperature uncertainty*

The temperature uncertainty (sometimes called temperature resolution), $\delta T$, is defined as the smallest temperature change detectable in a certain measurement. Assuming that the temperature uncertainty of a thermometer results only from changes in $R$, $\delta T$ is given by the Taylor's series expansion of the temperature as a function of $R$:

$$\delta T = \frac{\partial T}{\partial R}\delta R + \frac{1}{2!}\frac{\partial^2 T}{\partial R^2}(\delta R)^2 + \cdots$$

**Equation 2.11**

where $\delta R$ is the uncertainty in the determination of $R$, usually determined by the experimental conditions. Considering only the first term of the expansion, $\delta T$ becomes (BAKER; MCCLESKEY; BAKER, 2005):

$$\delta T = \frac{\partial T}{\partial R}\delta R$$

**Equation 2.12**

The $\delta T$ values are experimentally determined from the distribution of temperature readouts of a luminescence thermometer when at a certain reference temperature. $\delta T$ is then defined as the standard deviation of the resulting temperature histogram. For typical portable detection systems, $\delta R/R$ can reach, in the best case scenario, the value of 0.1%, meaning that typical sensitivities of 1–10% $K^{-1}$ (BRITES et al., 2012) correspond to temperature uncertainties of 0.01–0.1 K, respectively.

*2.2.4.3. Spatial and temporal resolution*

If the temperature is measured in different spatial positions, then it is possible to define a parameter that defines the minimum distance between points presenting a temperature difference higher than $\delta T$. This parameter is called the spatial resolution of the measurement ($\delta x$) (KIM et al., 2012):

$$\delta x = \frac{\delta T}{|\nabla T_{max}|}$$

**Equation 2.13**

where $|\nabla T_{max}|$ is the maximum temperature gradient of the mapping.

If, on the other hand, the temperature is measured with time, then it is possible to define a parameter that defines the minimum time interval between measurements presenting a temperature difference higher than $\delta T$. This parameter is called the temporal resolution of the measurement ($\delta x$):

$$\delta t = \frac{\delta T}{\left|\frac{dT}{dt}_{max}\right|}$$

**Equation 2.14**

Both temporal and spatial resolutions are important parameters in the evaluation of applicability of a thermometer for dynamic temperature measurements.

## 2.3. Heat distribution in biological systems

Since during the development of this thesis a great deal of experiments were carried out in small animals, it would be proper to dedicate a whole section of this chapter to the description of heat distribution in biological systems. This is, in fact, the purpose of Section 2.3.

In a biological system, heat transfer is characterized by the effects of blood flowing through the vascular circulatory system. As the blood moves through the microcapillary system, a stabilizing effect takes place, *i.e.*, the perfuse tissue returns to the natural equilibrium reference state (when there is no externally applied fluxes). This is what is commonly known as blood perfusion. In an exchange of thermal energy between the microcapillary network and the tissue, perfusion contributes in bringing the local tissue temperature closer to the body's core temperature. For instance, when a tissue's thermal energy is increased by an externally applied heat flux, perfusion aims to cool down the

tissue by removing blood at the elevated temperature and by replacing it with a blood whose temperature is closer to the one of the core.

If one considers the distribution of microcapillaries to be uniform and the relative size scale of the capillary diameter to be small when compared to the length scale characterizing heat transport, then perfusion can be viewed as a volumetric phenomenon. In other words, any local fluctuations in blood temperature resulting from the thermal exchange between an individual capillary and the tissue cannot be distinguished. The idea is that the network's blood flow, when viewed from a scale much larger than the diameter of an individual capillary, has no particular direction and permeates the tissue in a generally homogenous manner.

In mathematical terms, conduction of heat into a perfuse tissue is commonly represented by Penne's bioheat equation (PENNES, 1948):

$$\rho c_p \frac{\partial T_p}{\partial t} = \nabla \cdot \left(k_p \nabla T_p\right) - \rho_b c_b \omega_p \left(T_p - T_a\right) + g$$

**Equation 2.15**

where $\rho$, $c_p$, and $k_p$ stand for the density, specific heat and thermal conductivity of the tissue, respectively. The $g$ term stands for volumetric heat generation, which can be a function of both time and position. Heat generation can be a result of (i) low levels of metabolic sources or (ii) some higher intensity externally induced source. The variable $\omega_p$ stands for the blood perfusion rate and is representative of the volume rate at which blood passes through the tissue per unit volume of tissue ($m^3$ blood $s^{-1}$ )/($m^3$ tissue). The terms $c_b$ and $\rho_b$ refer to the specific heat and the density of blood, respectively. The symbol $T_a$ stands for the temperature of the blood at the body's core; hence, in simple words, the perfusion term aims to bring the local tissue temperature closer to the body's core temperature. The reason why Penne's bioheat equation is widely used by the scientific community lies on its simplicity and accuracy provided in numerical analysis, despite many alternative improved models in literature. For

all purposes, we assume the validity of **Equation 2.15** for the *in vivo* applications of the LNThs here developed. This thesis will not address the relative strengths and shortcomings of Pennes' bioheat equation. Notwithstanding, it is very much likely that, in the long-run, when studying biological systems with a highly complex heat distribution via blood flow, LNThs will shed some light on the extent of validity of **Equation 2.15**.

### 2.3.1. Biological systems under the influence of a heating source

Penne's bioheat equation can, in principle, be used to describe a diverse set of *in vivo* and *ex vivo* thermal experiments. In this subsection, however, we will narrow the discussion to the thermal dynamics of (i) a non-perfused tissue under the presence of heating NPs and (ii) a perfused tissue subject to laser-induced heating. With this, we aim to present the governing equations for each of those situations.

#### *2.3.1.1. Non-perfused tissue under the presence of heating NPs*

The subcutaneous thermal dynamics of a tissue with negligible blood perfusion can reasonably be expressed by the heat conduction equation. In fact, this is easily verified if one looks at **Equation 2.15**. If there's no blood perfusion, $\omega_p = 0$, the bioheat equation becomes:

$$\rho c_p \frac{\partial T_p}{\partial t} = \nabla \cdot \left(k_p \nabla T_p\right) + g$$

**Equation 2.16**

In the experimental conditions established throughout this thesis, the region where the heating NPs were being excited was much smaller than the heat dissipation length inside the tissue. Therefore, it was reasonable to assume the whole NP injection as a single heating point source. The time dependent temperature rise, due to a heating point source located at $\overrightarrow{r'}$, in a homogeneous medium with no perfusion was obtained using the Green's function formalism (NYBORG, 1988). The result was:

$$\Delta T(\vec{r},t) = \left(\frac{Q}{4\pi\alpha|\vec{r}-\overrightarrow{r'}|}\right) erfc\left(\frac{|\vec{r}-\overrightarrow{r'}|}{\sqrt{4\alpha t}}\right)$$

**Equation 2.17**

where $\alpha$ is the thermal diffusivity of the medium and Q is the volumetric heat generation rate. The average temperature over a sphere of radius R around the heating point source is, in turns, found to be:

$$\Delta T_{avg}(t) = \Delta T_{\infty}\left(1 + \left(\frac{t}{2\tau} - 1\right)\mathrm{erf}\left(\sqrt{\frac{t}{\tau}}\right) - \sqrt{\frac{t}{\pi\tau}}\left(e^{-\frac{\tau}{t}}\right)\right)$$

**Equation 2.18**

where $\Delta T_{\infty}$ is the steady temperature increment and $\tau$ is the relaxation time given by $R^2/4\alpha$.

**Equation 2.18** will be useful in the discussions of Section 4.2.4, where nanoheaters were injected into an *ex vivo* tissue.

*2.3.1.2. Perfused tissue subject to laser-induced heating*

For practical purposes, when one wants to insert the contribution of a laser beam in **Equation 2.15**, it is more suitable to write the bioheat equation in cylindrical coordinates:

$$\frac{\partial T(r,z,t)}{\partial t} = D\nabla^2 T(r,z,t) - b\,T(r,z,t) + \frac{1}{\rho c_p} g(r,z,t)$$

**Equation 2.19**

where $D = k_p/\rho c_p$, b = $\omega_p\rho_b c_{b/}\rho c_p$ and $T = T_p - T_a$. Since, throughout the development of this thesis, we frequently used a multimode laser fiber as a heating source, the *S(r,z,t)* term was expressed as an exponentially decaying function in the z direction:

$$S(z,t) = \begin{cases} \dfrac{2\alpha E_o}{\pi a^2 t_o}\,\Theta(\mathrm{a}-\mathrm{r})\mathrm{e}^{-\alpha \mathrm{z}}, & for\ z \geq 0\ and\ 0 \leq t \leq t_o \\ 0, & otherwise \end{cases}$$

**Equation 2.20**

where $\Theta(a\text{-}r)$ is the Heaviside function, $a$ is the beam radius, $t_o$ is the heating pulse duration, $\alpha$ is the absorption coefficient of the tissue and $E_o$ is the total energy of the heating pulse. Using the Green's function formalism to solve the bioheat equation in cylindrical coordinates, one finds that the thermal dynamics of the tissue is governed by the following equation (for more details see **Appendices 1**):

$$T(r,z,t) = C \int_0^{Min[t,t_o]} \left[ \int_0^a e^{-\frac{r'^2+r^2}{4D(t-t')}} I_o\left(\frac{rr'}{2D(t-t')}\right) r'^2 dr' \right] \times \frac{e^{-\alpha z+\alpha^2 D(t-t')}}{D(t-t')} Erfc\left(\frac{2D\alpha(t-t')-z}{\sqrt{4D(t-t')}}\right) dt'$$

**Equation 2.21**

where $I_o$ is the modified Bessel function of order zero and $C = \alpha E_o / 2\pi a^2 t_o \rho c$. **Equation 2.21** will be useful in the discussions of Section 5.3, where LNThs were used to subcutaneously monitor the laser-induced temperature incremente in a living mouse.

### 2.3.2. Thermal relaxation of a tissue

When retrieving the references related to the thermal dynamics of a tissue, one can find a frequent reference to what is called thermal relaxation. Traditionally, the thermal relaxation of a tissue is defined as the process by which a biological tissue recovers its initial temperature. Usually the experiment is comprised of two consecutive phases: (i) the tissue is submitted to a heating cycle generated by an external source of energy and (ii) the tissue cools down its temperature in the absence of heat source. For didactical purposes, this procedure is illustrated in **Figure 2.5**.

In the current subsection, the problem of thermal relaxation will be discussed under different conditions. The conclusions will be useful for further discussions of Chapter 5.

**Figure 2.5. Depiction of a common thermal relaxation process.**

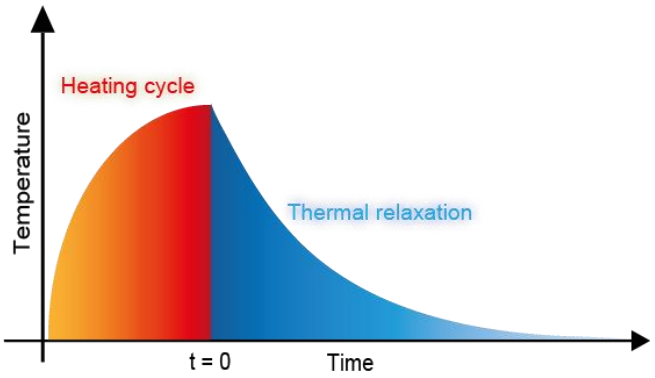


*2.3.2.1. Thermal relaxation of a non-perfused tissue*

The subcutaneous thermal relaxation of a tissue with negligible blood perfusion can reasonably be considered as a process mainly governed by heat conduction. In fact, this is easily verified if one looks at **Equation 2.15**. If there's no blood perfusion and no volumetric heat generating source (the heating cycle is supposed to be over in a thermal relaxation), then the bioheat equation becomes the well-known heat equation:

$$\nabla^2 T_{np} = \frac{1}{\alpha_{np}} \frac{\partial T_{np}}{\partial t}$$

**Equation 2.22**

where $\alpha_{np} = k/c_{np}\rho$ is the thermal diffusivity of the tissue with k and ρ being the thermal conductivity and density, respectively, and $T_{np}$ is the subcutaneous temperature. Taking the one-dimensional problem, $T_{np}$(z,t), and noticing that α has the dimensions of (length)$^2$ (time)$^{-1}$, the suitable correspondence $T_{np}(z,t) = T_{np}(z^2/\alpha t) = T_{np}(\eta)$ can be used. Therefore, Equation 2.15 becomes:

$$4\eta T''_{np}(\eta) + (2+\eta)\, T'_{np}(\eta) = 0$$

**Equation 2.23**

Which is a straightforward ordinary differential equation that leads to the Gauss error function (erf) solution:

$$T_{np}(\eta) = T_S + \Delta T \operatorname{erf}\left(\sqrt{\frac{\eta}{4}}\right)$$

**Equation 2.24**

with integration constants $T_S$ and $\Delta T$ corresponding to the final temperature (reached at $t \to \infty$) and the initial temperature increase, respectively. Moreover, regarding the definition of $\eta$, we can write (WELCH; GEMERT, 2011):

$$T_{Sc}(z,t) = T_S + \Delta T \operatorname{erf}\left(\sqrt{\frac{z^2}{4\alpha t}}\right) = T_S + \Delta T \operatorname{erf}\left(\sqrt{\frac{\tau_{cond}}{t}}\right)$$

**Equation 2.25**

where $\tau_{cond} = z^2/4\alpha$ is the thermal relaxation time (also called diffusion time) constant. Thus, the subcutaneous thermal profile could be described by an *erf* function if it is considered that a conductive heat transfer dominates the process.

*2.3.2.2. Thermal relaxation of a perfuse homogeneous tissue*

Following the discussion of Section 2.3.1.2, we express the bioheat equation in cylindrical coordinates, as in **Equation 2.19**, and the source for the heating cycle as a multimode laser fiber. When doing this, one can find the following expression for the tissue's thermal relaxation of a perfuse homogeneous tissue (for more details see **Appendices 1**):

$$T(r,z,t) = C \int_0^t \left[ \int_0^a e^{-\frac{r'^2 + r^2}{4D(t-t')}} I_o\left(\frac{rr'}{2D(t-t')}\right) r'^2 dr' \right]$$

$$\times \frac{e^{-\alpha z + \alpha^2 D(t-t')}}{D(t-t')} Erfc\left(\frac{2D\alpha(t-t') - z}{\sqrt{4D(t-t')}}\right) dt'$$

**Equation 2.26**

The main difference between **Equation 2.26** and **Equation 2.21** relies on the consideration of the dependence of the thermal relaxation on the previous heating cycle. **Equation 2.26** will also be used in the discussions of Section 5.3.

*2.3.2.3. Thermal relaxation of a perfuse composite material*

Here we describe the solution to **Equation 2.15** corresponding to the system depicted in **Figure 2.6** where four composite layers are presented: epidermis, papillary dermis, reticular dermis and muscle. These layers simulate the composition of a real biological tissue. Each layer has its own physical properties and, as a consequence, the parameters of equation **Equation 2.15** may experience a discontinuity at the interfaces. The top surface of the first layer (epidermis) is exchanging thermal energy by convection with a flow field ($h_o$) whose ambient temperature is $T_o$. On the other hand, the interface between muscle and bone (bottom of layer 4) is assumed to be at constant core body temperature, $T_{core}$ (BHARGAVA; CHANMUGAM; HERMAN, 2014; ÇETINGÜL; HERMAN, 2010). Additionally, both temperature and heat flux are required to be continuous throughout the tissue.

**Figure 2.6. Composite system representation of the perfuse tissue slab.**

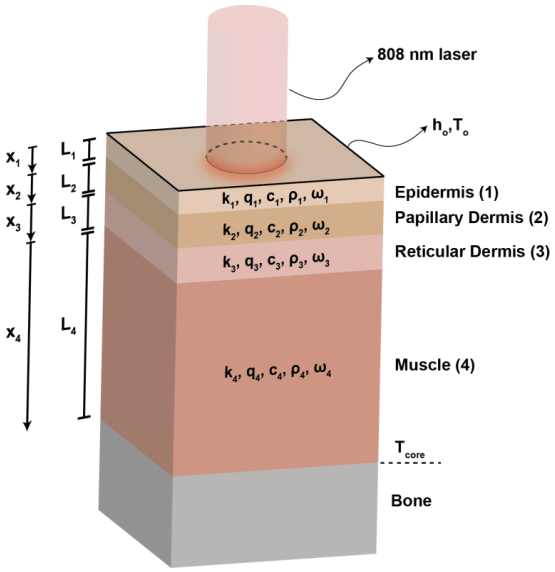

When considering the one-dimensional problem and by discretizing the solution in four parts (designated by the *i* index) corresponding to the temperature in each one of the layers, one can find the following temporal dependence for the tissue temperature (for more details see **Appendices 2**):

$$\frac{T_i(z_i,t) - T_i(z_i,\infty)}{T_i(z_i,0) - T_i(z_i,\infty)} = \exp\left(-\frac{\mathrm{t}}{\tau_{\mathrm{eff}}}\right)$$

**Equation 2.27**

where $\tau_{eff} = L_R^2/4\alpha_{eff}$ is the characteristic thermal relaxation time, $\alpha_{\mathrm{eff}}=(k_R\mu_R^2 + \rho_b c_b \omega_R L_R^2)/4\rho_R c_R$ is the effective thermal diffusivity of the system. The $k_R$, $\omega_R$ and $L_R$ terms stand for the thermal conductivity, perfusion rate and characteristic length of the so-called reference layer – *i.e.*, the layer presenting the minimum value for perfusion rate. The $\mu_R$ term corresponds to the eigenvalue obtained by the solution of algorithmic relations describing the problem.

Equation 2.27 will be useful in the discussions related to the effects induced by hindlimb ischemia in a living mouse as measured by LNThs.

# 3. Experimental Techniques

# 3.1. Optical Spectroscopy

In this section we will describe the instruments and experimental setups used to characterize the spectroscopic properties of the materials studied in this thesis, namely their photoluminescence and lifetimes.

## 3.1.1. Photoluminescence spectroscopy

**Figure 3.1. Schematic representation of the experimental setup used for photoluminescence spectroscopy**. An excitation laser beam is focused into a sample and its luminescence is collected by the same focusing objective. The luminescence is spectrally analyzed by a monochromator and finally collected by a CCD camera

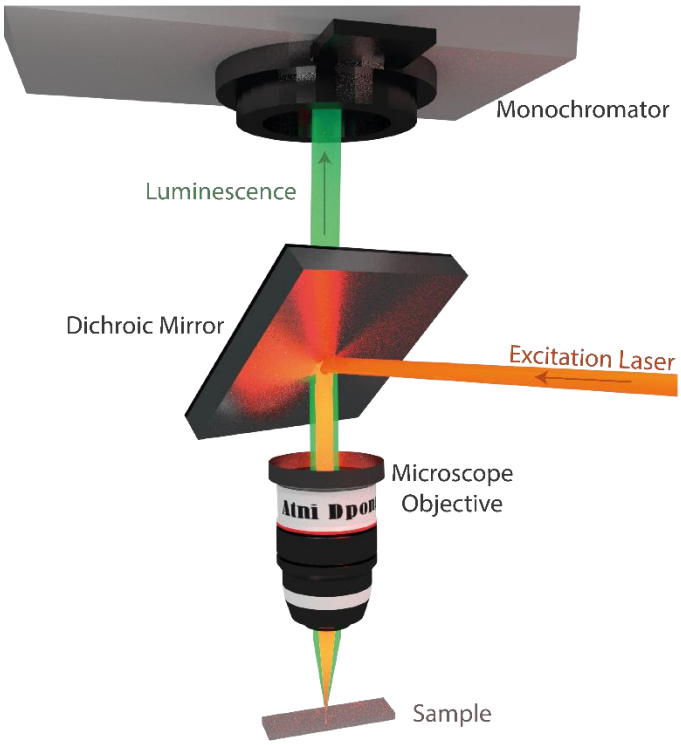


A homemade microscope was used to obtain the infrared emission spectra of different NPs. A laser diode was coupled to a fiber and connected to a collimator (Thorlabs PAFA-X-4-B). The laser diode was selected according to the wavelength that was more suitable for the investigation. Throughout this thesis, 690, 808 and 980 nm were the excitation wavelengths that were used. The laser

beam after being reflected in a dichroic mirror, was focused on the sample by means of a microscope objective (50X IR, numerical aperture 0.55). Luminescence was collected by the same microscope objective and, after passing through the dichroic mirror, which filtered the radiation corresponding to the excitation laser, was spectrally analyzed by a monochromator and finally collected by a CCD camera. The experimental setup is depicted in **Figure 3.1**. For the spectral analysis of the emission of Er-Yb@Nd $LaF_3$ NPs, a HORIBA iHR500 monochromator and a Synapse HORIBA CCD camera with silicon detector were used. The remaining emission spectra were recorded using a system composed of an Andor Shamrock 193i monochromator and an InGaAs Andor iDus DU490A CCD camera. For the recording of the spectra, we used the software provided by manufacturers: LabSpec5 and Andor SOLIS.

A thermoelectrically cooled Peltier plate (Linkam PE120) was mounted on the microscope stage in experiments that required a constant temperature for the sample. This system allowed the selection, with an accuracy of 0.1 ° C, of temperatures between and -25 and 120 °C.

### 3.1.2. Time resolved spectroscopy

For luminescence lifetime measurements, an optical parametric oscillator (Spectra Physics MOPO-730, generating pulses of 10ns with a repetition rate of 10 Hz) operating at 808 and 980 nm was used as the pump source. A pulsed Nd: YAG laser (Quanta Ray CG-230) operating at 355 nm was used to pump MOPO. The emission was spectrally filtered using a Spex 500 M monochromator. The detection of emission was achieved in this case by means of a GaAs photomultiplier (Hamamatsu R636, R5108 and R2949). A Lecroy Waverunner LT372 digital oscilloscope with a bandwidth of 500 MHz was used to measure the luminescence decay curves.

## 3.2. Infrared fluorescence imaging

For infrared imaging experiments, the setup schematically shown in **Figure 3.2a** was used. The setup was constituted of an excitation laser and an InGaAs

camera responsible for image collection. To minimize the noise, the system was isolated by means of a black box. The system included a heating plate at the base, responsible for keeping the animals at normal temperature.

**Figure 3.2. Infrared imaging system. (a)** Schematic representation of the basic infrared imaging system, consisting of an excitation diode laser and an infrared camera for detection. A heating plate and a methacrylate box complete the system. **(b)** Sensitivity curve of the InGaAs detector.

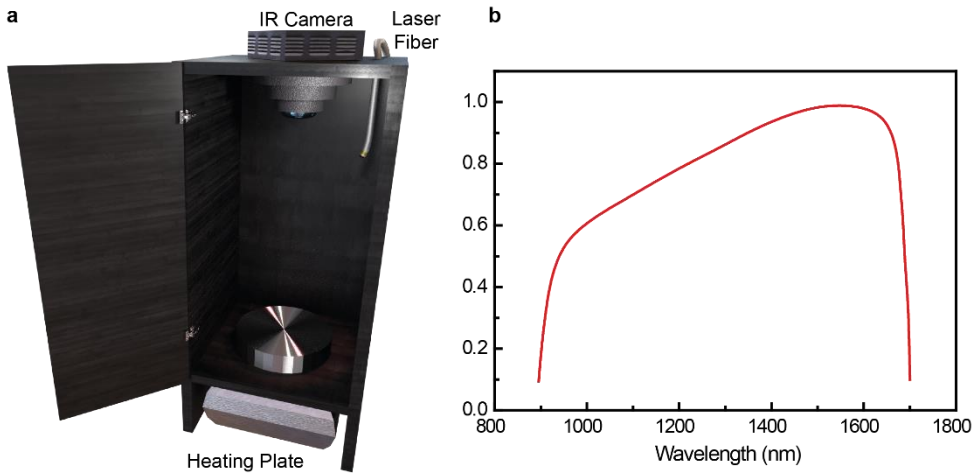


The laser diode, coupled to a 0.22 aperture fiber, was used as the excitation source. This laser was able to provide powers of up to 10 W and to operate in continuous or pulsed mode. In all the experiments, the desired power density was selected by regulating both the electric current applied to the diode (5-20 A) and the distance between the fiber and the surface to be irradiated.

As shown in **Figure 3.2b**, the detector of the InGaAs camera, Xeva-1.7-320 model, allows the detection of radiations with wavelengths within the 900-1700 nm range. To focus the image on the detector, a specific lens for near infrared (NIR) wavelengths (Optics Kowa LM 35mm SWIR) was used. An 850 nm high pass filter (Thorlabs FEL850) was placed between this lens and the camera to avoid any background signal coming from the 690 or 808 nm excitation lasers.

### 3.2.1. Spectrally filtered infrared imaging

**Figure 3.3. Spectrally filtered infrared imaging system.** A motorized filter wheel was added in front of the optics to the experimental system depicted in Figure 3.2 in order to filter the range of wavelengths detected by the infrared camera.


The spectral filtering technique, which allowed the acquisition of ratiometric thermal images in Section 5.3, is based on restricting the range of wavelengths detected by the camera. In order to do this, the previous setup was modified by adding a motorized filter wheel (Thorlabs FW102C) in the detection path. As shown in **Figure 3.3**, the filter wheel was placed in front of the optics used to focus the image on the InGaAs detector. This filter wheel, whose movement was remotely controlled through the manufacturer's software, allowed the insertion of up to six different filters. In the experiments in which this technique was applied, three band-pass filters with upper and lower cut-off wavelengths of (i) 980 and 1020 nm, (ii) 1200 and 1240 nm and (iii) 1530 and 1570 nm were used. In this sort of experiment, the 690 nm laser diode was working in continuous mode.

## 3.3. Infrared thermography

During the development of this thesis, infrared thermography was used to easily determine the surface temperature of living tissues. Additionally, this technique was used to study the photothermal effect of different NPs not only in dispersions but in *ex vivo* conditions as well. The thermographic camera utilized for the acquisition of thermal images was FLIR E40 bx. This camera was remotely controlled through FLIR Tools software and had an accuracy of 2 ° C in the -20-120 ° C range.

## 3.4. *In vivo* experiments

During the development of this thesis, several experiments have been carried out in animal models, *i.e. in vivo* tests in mice (*Mus musculus*), for various purposes:

- To study the thermal dynamics of a living tissue.
- To numerically evaluate the thermal properties of a living tissue.
- To evaluate the possibility of using core/shell NPs for *in vivo* subcutaneous thermal imaging.
- To observe ischemia induced variations in the physical properties of living tissues.

All the *in vivo* experiments were conducted in accordance with the European Union directives 63/2010UE and Spanish regulation RD 53/2013. The use of animals was also approved by the Animal Ethics Committee of Universidad Autónoma de Madrid.

The procedures to which the mice were subjected in the course of the investigation were supervised by designated investigators (Dr. Francisco Sanz, Dr. Nuria Fernández Monsalve, Dr. Luiz Monge and Dr. Maria de Carmen Iglesias de la Cruz, who are certified to manage animals for scientific experimentation, Certificate category C) as well as by the veterinary staff of the facilities. To

minimize the adverse effects suffered by animals, anesthesia (isoflurane) and analgesia were used. Regarding the application of inhaled isoflurane, sedation was induced with 5% isoflurane in a methacrylate chamber, in order to subsequently keep the animal asleep with 2% isoflurane until the end of the experiment.

In all experiments, some severity criteria were applied to minimize or eliminate adverse conditions (weight loss, edema, pain), sacrificing the animal in the most humane way. By the end of the experiments, the animals were sacrificed either by cervical dislocation or by inhalation of $CO_2$.

In the following subsections, we will describe the procedures followed on each *in vivo* experiment. Their main subsequent results are presented in Chapter 5.

### 3.4.1. Bioimaging

#### *3.4.1.1. Infrared bioimaging (PbS/CdS/ZnS QDs and Nd@Yb $LaF_3$ NPs)*

In order to get a deeper understanding on tissue modifications induced after artery ligation (described in subsection 3.4.2), long-term studies were conducted on 12 CD1 mice and the luminescence provided by PbS/CdS/ZnS QDs had to be observed for 30 days after surgery. This task was accomplished by using the same setup described in Section 3.2, the only difference being the anesthesia system incorporated by means of a controlled flow of isoflurane, as shown in **Figure 3.4**. The 808 nm excitation laser diode was kept in continuous mode, providing a power density of 0.5 $W \cdot cm^{-2}$ in all experiments. Furthermore, the presence of Nd@Yb $LaF_3$ NPs in Section 5.1.5 was also evidenced by this system.

These experiments were performed on a single CD1 mouse, in which 200 μL of a concentrated PBS dispersion of Er-Yb@Yb-Tm $LaF_3$ NPs (1% in mass) were subcutaneously injected. Immediately after the injection, the mouse was taken to the bioimaging system shown in **Figure 3.4**, where it was kept anesthetized throughout the whole experiment. For the recording of luminescence images, the

690 nm laser diode was used in continuous mode at a power density of 0.3 W ·cm$^{-2}$.

**Figure 3.4. In order to keep the mice anesthetized, a circular hole was made on one of the sides of the methacrylate box of the infrared imaging system through which a plastic tube, connected to the isoflurane flow, was incorporated.**


*3.4.1.2. Spectrally filtered infrared bioimaging*

## 3.4.2. Induction of unilateral hindlimb ischemia

In this experiment, a total of 12 CD1 mice were used. The goal was to investigate the correlation between the physical properties of a living tissue and the presence of ischemia. The results are described in detail in Section 5.2. The surgical procedure followed for the induction of unilateral hindlimb ischemia was first presented by Niiyama and coauthors (NIIYAMA et al., 2009). The corresponding steps are described in what follows:

**Figure 3.5. Induction of unilateral hindlimb ischemia. (a)** Incision made of the skin from the knee towards the medial thigh**. (b)** Occlusion of double knots on the femoral artery**. (c)** Closing of the incision**.**

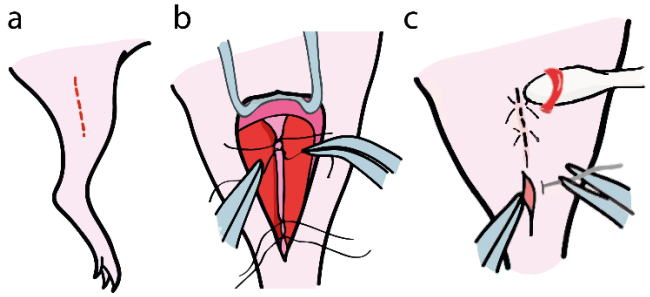


1. After being anesthetized with a continuous flow of isoflurane in 100% oxygen, the mice were placed in the supine position on the operating table.

2. The hair was removed from both hindlimbs with an electric shaver and a hair removal cream. Control infrared thermal images were then taken to point out the quasi-instantaneous difference in temperature between the hindlimbs.

3. The hindlimb was extended and secured with a piece of tape. Once the hindlimb was secure, the skin was wiped with three alternating betadine and alcohol scrubs. For the remainder of the surgical procedure, a dissection microscope at 10X or 20X magnification was used to obtain an enlarged view of the hindlimb region.

4. Using fine forceps and surgical scissors, an incision, approximately 1 cm long, was made of the skin from the knee towards the medial thigh (see **Figure 3.5a**).

5. Using phosphate buffered saline (PBS)-moistened fine pointed cotton swabs, subcutaneous fat tissue surrounding the thigh muscle was gently brushed away.

6. The cautery was transversely applied to incise and dissect through the subcutaneous fat tissue to reveal the underlying femoral artery.

7. A retractor was used to open the wound and to obtain a better view of the lower extremity vasculature.

8. Using fine forceps and a fine pointed cotton swab, the membranous femoral sheath was gently pierced through to expose the neurovascular bundle.

9. Then, using a clean set of fine forceps and cotton swab, the femoral artery was dissected and separated from the femoral vein and nerve at the proximal location near the groin. After the dissection, a strand of 7-0 silk suture was passed underneath the proximal end of the femoral artery. The proximal femoral artery was then occluded using double knots (**Figure 3.5b**). The tie was placed on the vessel as proximal to the wound as possible in order to leave space for the second tie and an intervening segment that would still be transected.

10. The femoral artery was separated from the femoral vein at the distal location close to the knee. A strand of 7-0 suture was passed underneath the distal end of the femoral artery proximal to the popliteal artery.

11. The vessel was occluded using double knots. The distal femoral artery was occluded with a second set of double knots just proximal to the first set of knots.

12. This second set of sutures was used to grip the artery during the transaction procedure. Similarly, for gripping purposes, the proximal femoral artery was occluded with a second set of double knots just distal to the first set of knots.

13. The retractor was removed and the incision was closed using 5-0 Vicryl sutures (**Figure 3.5c**). These sutures did not need to be removed at a later time, as they dissolved on their own.

14. Once the incision was closed, the animal was placed on top of a draped heated pad in the recovery cage and monitored continuously until awake.

### 3.4.3. Metabolic cage experiments (phenomaster)

In order to measure the possible adverse effects of PbS/CdS/ZnS QDs on different physiological and metabolic processes in mice, *in vivo* metabolic cage experiments were carried out in the Veterinary Office of the "Alberto Sols"

Biomedical Research Institute (CSIC-UAM). In these experiments, a total of 6 female CD1 (Harlan) mice were used. They were kept in individual TSE Phenomaster cages (TSE systems) for five days. Those cages allowed to measure, every hour, different parameters related to the physical and metabolic activity of mice, including:

- Amount of food and drink ingested by mice
- Movement of mice in the center and on the periphery of the cage, which was measured from cuts in light beams in the plane of the floor of the cage. From these data, the system automatically determined the total distance traveled by the mice.
- Temperature.
- Expired $CO_2$ and consumed $O_2$ volumes. The quotient of both allowed determining the respiratory exchange rate (RER).
- Heat production ($W \cdot kg^{-1}$)

**Table 3.1. Distribution of mice for metabolic cage experiments.**

| NP | Administration route | Inoculated doses | Number of mice |
|---|---|---|---|
| **PbS/CdS/ZnS QDs** | Oral | 200 µL (0.1 mg $ml^{-1}$ in water) | 3 |
| | Intravenous | 100 µL (0.1 mg $ml^{-1}$ in PBS) | 3 |

The first of the 5 days of experiments was used for the acclimation of mice to the metabolic cages. On the second day, the mice were orally or intravenously inoculated with QDs of PbS/CdS/ZnS, following the detailed scheme found in **Table 3.1**. Oral inoculations were performed without anesthetizing the mice by using a metal cannula with olive tip. For the case of intravenous administration, the NPs were retro-orbitally injected in the mice after being anesthetized. After

administration of the NPs, the mice returned to their respective cages to carry out the study of their physical and metabolic activities for 4 full days. The results are summarized in Figures 3.5, 3.6 and 3.7.

**Figure 3.6. Cumulative drink and food intake in the mice treated with NPs as compared to the control mice**. A slightly lower food intake was observed for the IV (intravenous administration) group (left column) with respect to the control case, although the difference is not significant. The water intake was markedly lower in the PO (oral administration) group (right column) than in the IV group, but no differences were observed betweeen the control mouse and those inoculated with NPs, which indicates that this difference is likely related to the oral administration procedure.

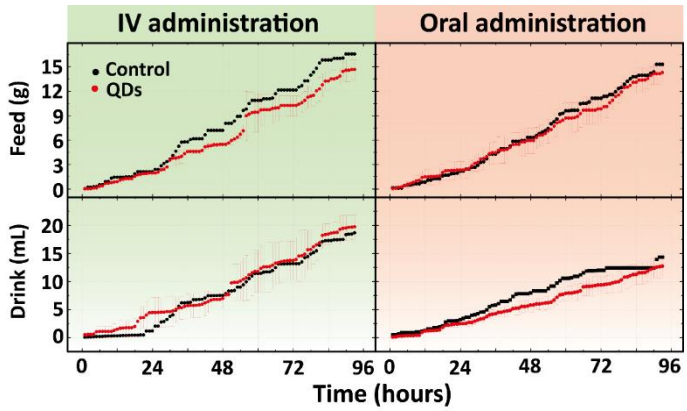


**Figure 3.7. Movement-related parameters (cumulative distance, sum of central movements and sum of peripheral movements) measured during the metabolic studies.** In the PO group, a substantial difference exists between the mice which received QDs and the control mouse, which showed a much higher degree of activity. However, all remaining mice showed very similar activity parameters, including the control mouse in the IV group, which indicates that most likely, the control mice presented an abnormally high movement.

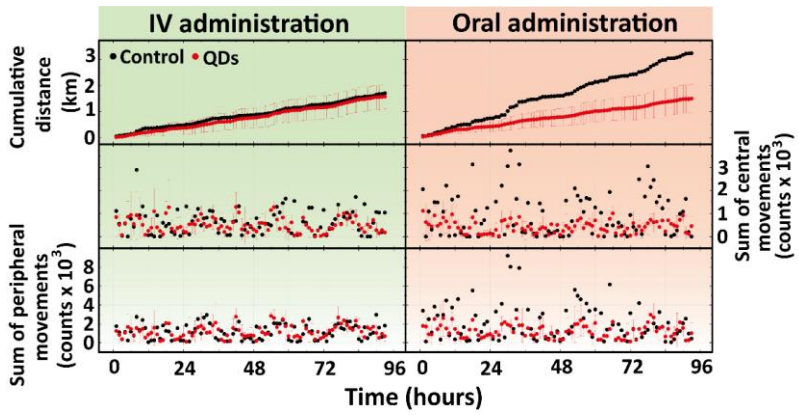

**Figure 3.8. Thermodynamic parameters (temperature, respiratory exchange rate –RER- and heat production measured during the metabolic studies for IV (left column) and PO (right column) administered mice.** Circadian variations of temperature were recorded in all mice. These variations are related to daily cycles of light and activity and were in the range of normal rythms (1 °C-4 °C) for all animals. RER indirectly shows the muscle's oxidative capacity to get energy and is modified by mouse physical activity during light cycles. Heat production (H) by indirect gas calorimetry was calculated by Phenomaster software using measurements of the animal's oxygen consumption (VO2) and carbon dioxide production (VCO2). All these parameters yielded very similar values for all mice, revealing no change due to the administration of NIR-QDs.

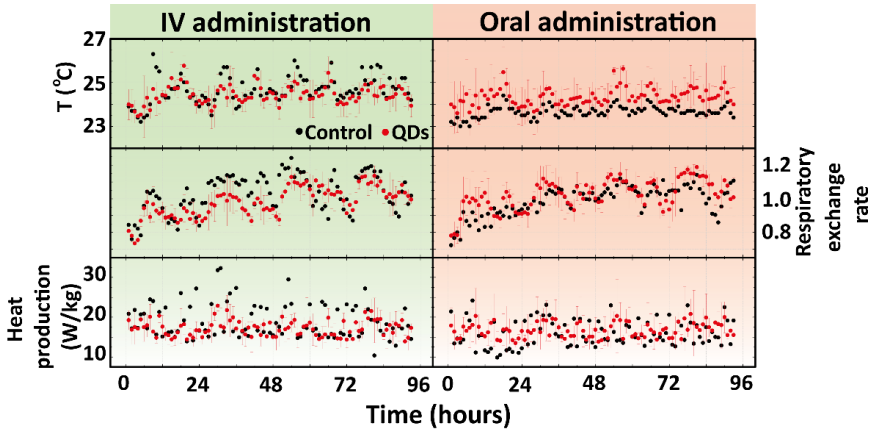


## 3.5. Programmed tools

In order to better analyze the experimental data obtained under the development of this thesis, some useful codes were written. In this section, they will briefly be described.

### 3.5.1. Evaluating the calibration parameters in ratiometric thermal sensors

A program was made to calculate the thermal sensitivity (S) that best fits the calibration data (see subsection 2.2.4.1). This task was achieved by analyzing the intensity ratio (R) between two lines of emission, $\lambda_1$ and $\lambda_2$.

The resulting output files were:

- All the spectra normalized by I($\lambda_1$);

- Temperature dependence of the ratio R;

- Temperature dependence of the relative thermal sensitivity, $S_R$, assuming a linear relation between R and T and

- Temperature dependence of $S_R$ assuming an exponential relation between R and T (used for Er-Yb@Nd $LaF_3$ NPs).

### 3.5.2. Building up a ratiometric thermal video

Once fluorescence images obtained at two different wavelengths $\lambda_1$ and $\lambda_2$ were obtained through the experimental setup described in Section 3.4.1.2, a home-made developed program was used to calculate, pixel by pixel, the ratio between emitted intensities at $\lambda_1$ and $\lambda_2$. The resulting ratiometric fluorescence image was then converted into temperature units by using the corresponding calibration parameters. The flow diagram followed by the program to build up a thermal video from fluorescence images is depicted in **Figure 3.9**.

**Figure 3.9. Flowchart followed by the home-made software to build up a thermal image from fluorescence images.** m×r stands for the resolution of the fluorescence images, while n_total corresponds to the total number of fluorescence images obtained at each wavelength range.

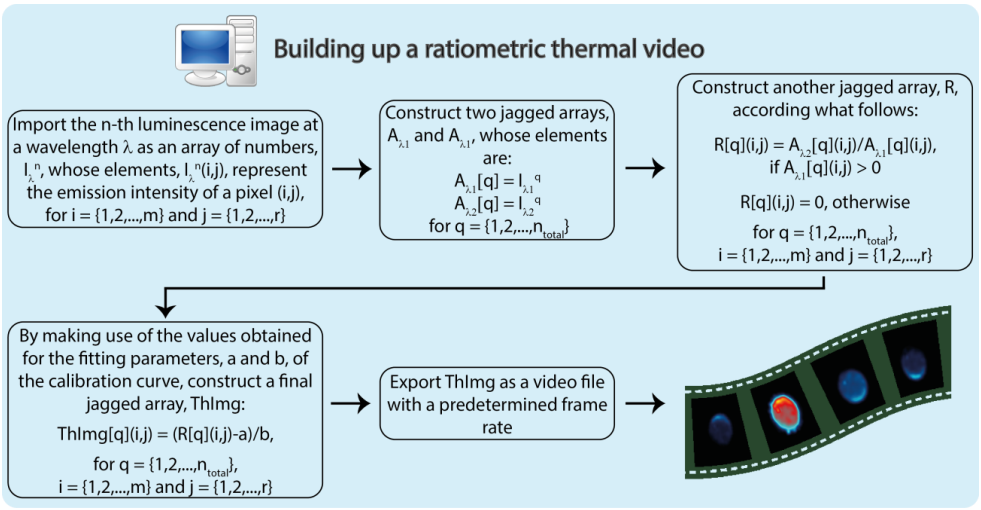


## 3.6. Transmission Electron Microscopy

The evaluation of geometry and size of the NPs used throughout this thesis was obtained by means of a transmission electron microscope (TEM, TECNAI G2

with resolution 0.2 nm) from the medical center of Universidad Autónoma de Madrid. In order to visualize the samples in the TEM, it was necessary to follow some steps. First of all, the samples were diluted (1/10 or 1/100). Then, a small amount of the dilution was dropped on a copper grid and left in contact with the air for 5 minutes until all liquid had evaporated. Afterwards, the grids were placed on a sample holder which, in turns, was inserted in the observation chamber of the equipment. TEM images were captured in randomly selected regions of the surface of each plate. The evaluation of the average size of the NPs was made through the analysis of those images on the *Image J* software.

**Figure 3.10. (a)** FEI Tecnai G2-F20. **(b)** Grid on the parafilm (the copper side has to be oriented upwardly). **(c)** Deposition of NPs dilution on the grid.

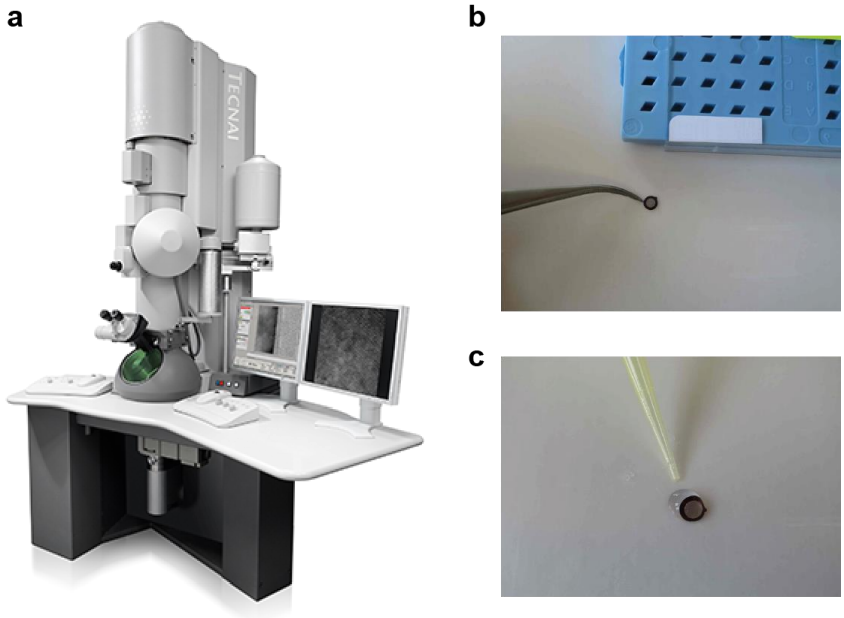


## 3.7. Electron paramagnetic resonance (EPR)

Electron Paramagnetic Resonance (EPR) spectra of annealed nanometric-sized powders were recorded by means of a Bruker ESP 300E spectrometer working in the X-band with field modulation of 100 kHz. The temperature of the sample was controlled with a continuous-flow helium cryostat (Oxford Instruments ESR 900). Accurate values of the resonance magnetic fields and

microwave frequencies were measured with a NMR gaussmeter (Bruker ER 035 M) and a frequency meter (Hewlett-Packard 5342A) respectively.

## 3.8. Energy dispersive X-Ray (EDX)

Energy dispersive X-Ray spectroscopy is a measuring technique that provides accurate elemental analysis with high spatial resolution. Energy dispersive X-ray (EDX) spectroscopy was performed using a JEOL JEM 3000F scanning electron microscope, operated at 300kV. The samples for EDX analyses were prepared just as for the TEM measurements.

## 3.9. NPs synthesis

**Table 3.2. Main characteristics of the NPs used throughout this thesis.** The table includes the sizes obtained through transmission electron microscopy (TEM) images and surface coating if they have one. In addition, for the doped with $Ln^{3+}$ ions, the molar percentage of the doping ions is shown.

| NPs | % of doping ions (mol %) | Superficial coating | Average size TEM (nm) | Provenance |
|---|---|---|---|---|
| Er-Yb@Nd $LaF_3$ | $Er^{3+}$ - 2, $Yb^{3+}$ - 10, $Nd^{3+}$ - 10 | -- | $30 \pm 4$ | UFAL |
| Yb@Nd $LaF_3$ | $Yb^{3+}$ - 10, $Nd^{3+}$ - 10 | -- | $24 \pm 5$ | UFAL |
| Yb@Nd* $LaF_3$ | $Yb^{3+}$ - 10, $Nd^{3+}$ - 40 | -- | $24 \pm 5$ | UFAL |
| PbS/CdS/ZnS QDs | -- | MPA | $5.6 \pm 0.6$ | INRS |
| Er-Yb@Yb-Tm $LaF_3$ | $Er^{3+}$- 2, $Yb^{3+}$ - 10, $Tm^{3+}$ - 10 | -- | $32 \pm 1$ | UFAL |

In this section, we will describe the synthesis routes followed to produce the NPs studied throughout this thesis. The main properties (composition, surface coating, size, hydrodynamic diameter and potential zeta) of the NPs are indicated

in Table 3.2. The transmission electron microscopy (TEM) images, from which the size was determined, are shown in **Erro! Autoreferência de indicador não válida.**. The synthesis and basic characterization of the physicochemical properties of the NPs was carried out by different groups (see Table 3.2), which mostly aims not at manufacturing but at studying different systems for biological applications.

**Figure 3.11. TEM images of the NPs used in this doctoral thesis provided by the correspondent group in charge of the synthesis. (a)** Er-Yb@Nd $LaF_3$ NPs, **(b)** Yb@Nd* $LaF_3$ NPs, **(c**) Yb@Nd $LaF_3$ NPs, **(d)** Nd@Yb $LaF_3$ NPs, **(e)** PbS/CdS/ZnS QDs and **(f)** Er-Yb@Yb-Tm $LaF_3$ NPs.

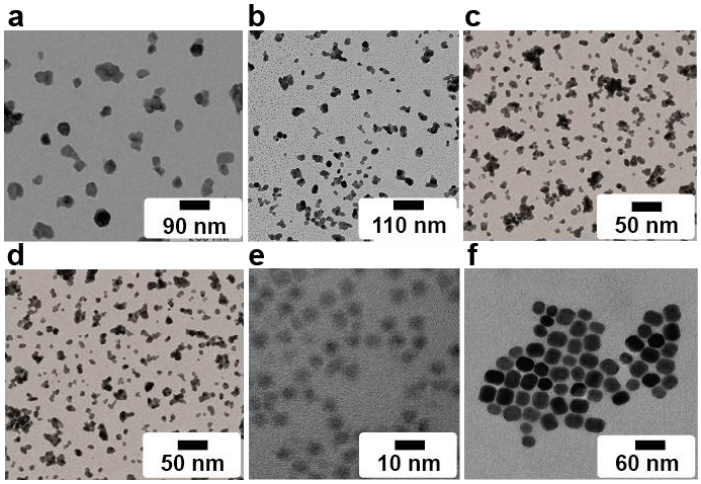


### 3.9.1. PbS/CdS/ZnS QDs

The PbS/CdS/ZnS QDs used in this thesis were synthesized by Dr. F. Ren, from the group of Prof. D. Ma in Centre Énergie Matériaux Télécommunications of the Institut National de la Recherche Scientifique (INRS) in Québec (Canada).

Lead chloride (98%), sulfur (100%) ,oleylamine (OLA) (technical grade, 70%), cadmium oxide (99%), methanol (anhydrous, 99.8%), octadecene (ODE), mercaptopropyl acid (MPA) (≥99.0%), 1-methyl-2-pyrrolidinone (NMP) (≥99%), butylamine(99.5%), phosphorous pentasulfide (99%), and zinc chloride (99.999%) were obtained from Sigma-Aldrich Inc. Hexane, PBS (pH 7.4),

oleicacid (OA), toluene, and ethanol were purchased from Fisher Scientific Company. All chemicals were used as purchased.

The core of QDs, made of PbS, was synthesized using OLA as the surface coating. First, a mixture of 10 g of lead chloride ($PbCl_2$) and 24 mL was heated to 160 °C using an oil bath, keeping this temperature for 1 hour under nitrogen. Then, the solution was allowed to cool to 120 °C and, in order to remove the remains of water and organic solvents, was subjected to vacuum for 30 minutes. The dispersion of 115 mg of sulfur in 4 mL of OLA was rapidly injected in the $PbCl_2$-OLA mixture at room temperature with vigorous stirring. After maintaining the reaction cell at 100 °C for 10 minutes, the cell was cooled using cold water.

A CdS shell was added onto the PbS core obtained from the previous reaction by following a method reported by Ren and coauthors (REN et al., 2013). In order to start the synthesis, a mixture of 3 g of cadmium oxide, 15 mL of OA and 20 mL of ODE was heated using an oil bath until the dispersion became colorless (200-250 °C). At that time, the dispersion was cooled to 100 °C and degassed in vacuum for 30 minutes. The temperature was again reduced to 20 °C, to then inject 12 mL of the dispersion of PbS QDs. Finally, 20 mL of this mixture was introduced into a 35 mL reaction tube and put in a microwave reactor (Discover, CEM Corporation) at 100 °C for 3 minutes.

Finally, to add the ZnS shell together with the surface coating made of MPA, the method reported by Benayas and coauthors was followed (BENAYAS et al., 2015). In a typical reaction, 0.045 mmol of phosphorus pentasulfide, 0.4 mL of MPA and 0.3 mL of butylamine in 10 mL of NMP were mixed and heated at 110 ° C for 20 minutes in a sealed vial to dissolve the sulfur. In a separate vial, 0.51 mmol of zinc chloride, 0.4 mL of MPA and 0.3 mL of butylamine were mixed with 10 mL of NMP and heated in the same manner to dissolve the zinc chloride. After allowing to cool it down to room temperature, 0.007 g of the core/shell OLA-PbS/CdS QDs obtained above were dispersed in the phosphorus pentasulfide

solution and then mixed with the zinc chloride solution. This mixture was heated at 70 °C for 30 minutes, giving as a final product the core/shell/shell QDs of PbS/CdS/ZnS with a surface coating of MPA.

### 3.9.2. Rare-earth doped $LaF_3$ NPs

Those samples were all synthesized in the Institute of Physics of the Universidade Federal de Alagoas by the co-precipitation technique in aqueous solution. Lanthanum (III) chloride ($LaCl_3$, >99.99%), Neodymium (III) chloride ($NdCl_3$, ≥99.99%), Ytterbium chloride ($YbCl_3$, 99.99%), erbium chloride ($ErCl_3$, 99.99%), thulium chloride ($TmCl_3$, 99.99%) and ammonium fluoride ($NH_4F$, ≥99.99%), were purchased from Sigma-Aldrich. All reagents were used directly without further purification.

The choice of $LaF_3$ as the host matrix was motivated by several reasons. Firstly, the reduced phonon energy of $LaF_3$ leads to large fluorescence efficiencies (STOUWDAM; VAN VEGGEL, 2002). In addition, the inclusion in the crystalline network of an important number of ions, required to achieve large efficiencies of energy transfer and pump-to-fluorescence conversion, should be performed without inducing deformation of the crystal lattice. The preservation of the original network parameters is necessary to preserve the luminescent properties of the ions used for thermal sensing. For instance, a remarkable increment of lattice disorder would lead to an increment in the linewidth of luminescence lines making ratiometric measurements difficult.

#### *3.9.2.1. Er-Yb@Nd $LaF_3$ NPs*

For the synthesis of core/shell Er-Yb@Nd $LaF_3$ NPs, a two-step procedure was used. 0.29 g of lanthanum chloride, 3.42 mg of erbium chloride and 13.97 mg of ytterbium chloride were added to 80ml of distilled water under stirring at 75°C, followed by a dropwise addition of a solution of 0.30g of ammonium fluoride in 5ml of water. For the formation of shell around the core particles a solution of 15ml of water containing 0.22g of lanthanum chloride and 78mg of neodymium chloride was added dropwise to the reaction mixture while stirring

after 90 min. The reaction was allowed to continue for 2h. Afterwards the NPs were precipitated in distilled water. They were collected by centrifugation and dried for 48h at ambient atmosphere. The powder was then annealed at 500 $^{o}$C for 3 hours.

In the core/shell structures minimum perturbation of the host lattice due to a "massive" incorporation of neodymium ions is required to ensure a good "epitaxial" match between core and shell units. In this sense $LaF_3$ has demonstrated to be an ideal host as the ionic radius of $La^{3+}$ is just slightly larger than that of $Nd^{3+}$ and this makes possible to introduce a larger concentration of $Nd^{3+}$ impurities in the $LaF_3$ matrix without deformation of the lattice. Note that in the case of other host matrices in which the neodymium ions replace lattice ions with quite different ionic radius (such as $Y^{3+}$ in $NaYF_4$ or in YAG) the incorporation of high concentration of neodymium could lead to large lattice distortions (ZHANG et al., 2013).

*3.9.2.2. Yb-Nd, Nd@Yb, Yb@Nd and Yb@Nd* LaF3 NPs*

Preparation of single-core 10% $Yb^{3+}$-10% $Nd^{3+}$ $LaF_3$ Shell NPs (Yb@Nd):

The Yb-Nd $LaF_3$ NPs were prepared by wet-chemistry method. Typically, (1-x-y) mmol of $LaCl_3$ , x mmol of $NdCl_3$ ( x = 0.1) and ymmol $YbCl_3$ (y = 0.05, 0.1, 0.2 and 0.3) were added to 80 mL distilled (DI) water in a round bottom single neck flask under continuous stirring for 15 min, and heated to 75ºC. Then, 3 mmol of $NH_4F$ was diluted in 3 mL DI water and added dropwise to the above mixed chemical solution. The mixture was kept at 75°C for 3 hours at ambient pressure under continuous stirring. A white suspension was formed gradually upon stirring. The obtained NPs were collected by centrifugation at 8,000 rpm for 7 min. The precipitate was washed with distilled water several times and finally centrifuged at 12,000 rpm for 12 min and dried at 60°C at ambient atmosphere for 2 days and then annealed at 500oC for 3 hours.

Preparation of 10% $Yb^{3+}$:$LaF_3$ Core-10% $Nd^{3+}$:$LaF_3$ Shell NPs (Yb@Nd):

0.9mmol of $LaCl_3$ and 0.1mmol of $YbCl_3$ were added to 80 mL DI water in a round bottom single neck flask under continuous stirring for 15 min, and heated to 75ºC. In contrast to the synthesis of the simple core, a solution of 6.6 mmol of $NH_4F$ was diluted in 6 mL DI water and added dropwise to the above mixed chemical solution. The reaction was allowed to continue for 2 hours at 75°C. Then a solution of 0.9mmol of $LaCl_3$ and 0.1mmol of $NdCl_3$ was added dropwise. The reaction was allowed to continue for another 2 hours at 75°C and then allowed to cool to room temperature. The core/shell nanoparticles were precipitated and separated by centrifugation. The precipitate was washed with DI water several times and dried 60 $^oC$ at ambient atmosphere for 2 days and then annealed at 500 $^oC$ for 3 hours.

In these core shell nanoparticles synthesis, a sufficient amount of fluoride was readily mixed in the first step, so as a part of fluoride forms the core and the excessive fluoride is absorbed on the core surface. When the shell solution containing $Ln^{3+}$ (Ln = La, Nd) ions is added, the $Ln^{3+}$ interacts with the $F^-$ ions gradually. A similar procedure was followed to prepare 10%$Nd^{3+}$:$LaF_3$ core-10%$Yb^{3+}$:$LaF_3$ shell nanoparticles (Nd@Yb $LaF_3$ NPs) and 10% $Yb^{3+}$:$LaF_3$ core-40%10%$Nd^{3+}$:$LaF_3$ shell except that in the former $Nd^{3+}$ ions were incorporated in the core and $Yb^{3+}$ ions in the shell and in the latter a solution of 0.6mmol of $LaCl_3$ and 0.4mmol of $NdCl_3$ was added dropwise.

*3.9.2.3. Tm3+-Yb3+-Er3+ LaF3 and Er3+-Yb3+@Yb3+-Nd3+ LaF3 NPs*

Preparation of single core $Tm^{3+}$/$Yb^{3+}$/$Er^{3+}$:$LaF_3$ nanoparticles:

The $Tm^{3+}$/$Yb^{3+}$/$Er^{3+}$codoped $LaF_3$ NPs used in this work were prepared by wet chemistry method. Typically, (1-x-y-z ) mmol of $LaCl_3$ , x mmol of $TmCl_3$ ( x = 0.1),y mmolof YbCl3 (y = 0.1) and z mmol of ErCl3 (z =0.02) were added to 80 mL distilled (DI) water in a round bottom single neck flask under continuous stirring for 15 min, and heated to 75$^oC$. Then, 3 mmol of $NH_4F$ was diluted in 3 mL DI water and added dropwise to the above mixed chemical solution. The mixture was kept at 75°C for 3 hours at ambient pressure under continuous

stirring. A white suspension was formed gradually upon stirring. The obtained NPs were collected by centrifugation at 8,000 rpm for 7 min. The precipitate was washed with distilled water several times and finally centrifuged at 12,000 rpm for 12 min and dried at 60°C at ambient atmosphere for 2 days and then annealed at 500°C for 3 hours.

Preparation of 2%$Er^{3+}$/10%$Yb^{3+}$:$LaF_3$ Core - 10%$Yb^{3+}$/10%$Tm^{3+}$:$LaF_3$Shell nanoparticles (Er-Yb@Yb-Tm$LaF_3$ NPs):

0.88mmol of $LaCl_3$, 0.1mmol of $YbCl_3$ and 0.02mmol of $ErCl_3$ were added to 80 mL DI water in a round bottom single neck flask under continuous stirring for 15 min, and heated to 75°C. In contrast to the synthesis of the simple core, a solution of 6.6 mmol of $NH_4F$ was diluted in 6 mL DI water and added dropwise to the above mixed chemical solution. The reaction was allowed to continue for 2 hours at 75°C. Then a solution of 0.8mmol of $LaCl_3$, 0.1mmol of $YbCl_3$and 0.1mmol of $TmCl_3$ was added dropwise. The reaction was allowed to continue for another 2 hours at 75°C and then allowed to cool to room temperature. The core/shell nanoparticles were precipitated and separated by centrifugation. The precipitate was washed with DI water several times and dried 60°C at ambient atmosphere for 2 days and then annealed at 500°C for 3 hours.

In these core shell nanoparticles synthesis, a sufficient amount of fluoride was readily mixed in the first step, so as a part of fluoride forms the core and the excessive fluoride is absorbed on the core surface. When the shell solution containing $Ln^{3+}$ (Ln = La, Tm, Yb) ions is added, the $Ln^{3+}$ interacts with the $F^-$ ions gradually.

# 4. Core/shell NPs for self-controlled heating

As explained in the introduction, it is extremely necessary to have a temperature reading in order to have a better control of a treatment during PTTs. In this sense the design and synthesis of a single NP capable of both heating and thermal sensing appeared to be especially interesting but, at the same time, quite challenging. First it was required that the heating and sensing particle operated under single beam excitation. Secondly, the optical excitation wavelength should avoid nonselective cellular damage. The first requirement was related to the complexity of the system of measurement – *i.e.* it should be as simple as possible. The second one had to do with avoiding undesired effects that could be produced by the excitation laser. If one looks into literature, one will find out 808 nm as the optimum excitation wavelength as it minimizes both the laser-induced thermal loading of the tissue and the intracellular photochemical damage (HONG et al., 2012; LI et al., 2013; NYK et al., 2008; ZHANG et al., 2012). Additionally, the existence of high power, cost-effective laser diodes operating at 808 nm made this specific wavelength interesting from the technical point of view (ZHAN et al., 2011).

In this sense, two single NPs capable of remote heating and thermal sensing under single 808 nm optical excitation are presented in the following sections,. The first one was specifically designed to introduce the concept of a single multifunctional NP. Its importance, therefore, was not so much on whether its emission was found in one of the BWs but rather on the fact that it was indeed possible to construct a simultaneous nanoheater and nanothermometer in a single NP by means of the core/shell engineering. The second one, on the other hand, was meant to present a broader applicability. Its focus was not only placed on the light-to-heat conversion efficiency but also on the spectral position of its thermal-sensitive emission (specifically in BW-II).

## 4.1. Self-monitored photothermal nanoparticles based on core-shell engineering (Er-Yb@Nd $LaF_3$ NPs)

When retrieving the existing literature prior to the development of this thesis, it was possible to find many examples of heating NPs that, when excited at 808nm, presented large light-to-heat conversion efficiencies, including carbon nanotubes (CNTs), gold nanorods (GNRs), quantum dots (QDs), organic nanoparticles (ONPs) and NPs heavily doped with neodymium (Nd:NPs, see discussion in Section 2.1.1) (BEDNARKIEWICZ et al., 2011; CHENG et al., 2012; JING-LIANG LI; MIN GU, 2010; KANG et al., 2010; KUCSKO et al., 2013; LAMBERT et al., 2007; MAESTRO et al., 2013a, 2013b; MARCINIAK et al., 2015). Despite the great list of examples, only Nd:NPs had shown some ability for remote thermal sensing. Notwithstanding, achieving temperature resolutions below 1 °C was extremely hard due to their relatively low thermal sensitivity ($10^{-3}$ $°C^{-1}$) (see discussions in Section 2.2.4.2 concerning temperature uncertainty) (LI et al., 2013; ROCHA et al., 2013, 2014a; SMITH; MANCINI; NIE, 2009; WANG et al., 2013a; WEBER, 1971; WEISSLEDER, 2001; ZHAO et al., 2015). At the time, different routes had been proposed to overcome this problem. For instance, some of the routes that had been tried were: the combination with other emitting units such as quantum dots (QDs), the co-doping with other rare earth ions and the structural improvement by post-synthesis processes (CERÓN et al., 2015; MARCINIAK et al., 2015; SIDIROGLOU et al., 2003). Although some improvements had in fact been achieved, their application in sub-degree measurements was still something unattainable.

### 4.1.1. Proposed NPs (Er-Yb@Nd $LaF_3$ NPs)

By realizing the limitations imposed on Nd:NPs, we started to explore the alternative of improving their thermal sensitivity by means of the core/shell engineering. The motivation came from the fact that different distributions of rare earth dopants in core/shell units could be used to tailor their optical properties - something that was clearly observed in the many works dealing with

the tuning of upconversion luminescence (VETRONE et al., 2009; WANG; LIU, 2008; WEN et al., 2013). Our proposal was ignited by the $Nd^{3+}$ ions ability of acting as sensitizers of rare earth ions commonly used in highly sensitive luminescence thermometry (whose thermal sensitivity lied was of the order of $10^{-2}$ °C) - specifically, $Yb^{3+}$ and $Er^{3+}$ (BARBOSA-GARCÍA et al., 1997; ROTMAN, 1990; WANG et al., 2013b). It was well known in literature that the combination of $Nd^{3+}$, $Yb^{3+}$ and $Er^{3+}$ into a single NP provided an efficient green emission generated by $Er^{3+}$ ions under single 808 nm optical excitation of $Nd^{3+}$ ions thanks to both $Nd^{3+} \rightarrow Yb^{3+}$ and $Yb^{3+} \rightarrow Er^{3+}$ energy transfer (ET) processes, with efficiencies superior to 50% (HUANG; LIN, 2015). Notwithstanding, some requirements had to be satisfied. In fact, the efficient excitation of the thermosensitive $Er^{3+}$ ions could only be achieved if they were spatially separated from the $Nd^{3+}$ sensitizing ions (see **Appendices 3**). This spatial separation avoided the $Er^{3+}$ luminescence quenching due to ET between erbium and neodymium states (CHEN et al., 2012; ROCHA et al., 2014a; WANG et al., 2013b). In the NPs that we proposed, this spatial separation was achieved by means of the core/shell nano-engineering. These NPs are schematically drawn in **Figure 4.1a** where we have a $Nd^{3+}$ doped shell surrounding an $Er^{3+}$,$Yb^{3+}$ co-doped core. Under this approach, the shell acts as a donor unit absorbing the 808 nm radiation through the $^4I_{9/2} \rightarrow {}^4F_{5/2}$ $Nd^{3+}$ absorption (see **Figure 4.1b**). Then, non-radiative ET between $Nd^{3+}$ and $Yb^{3+}$ ions at the core/shell interface results in the $^2F_{7/2} \rightarrow {}^2F_{5/2}$ excitation of $Yb^{3+}$ ions inside the core (OSTROUMOV et al., 1998; TU et al., 2011). Finally, ET between $Yb^{3+}$ and $Er^{3+}$ ions allocated at core leads to the excitation of erbium ions up to their $^2H_{11/2}$, $^4S_{3/2}$ thermally coupled states (**Figure 4.1b**), from which the thermal sensitive luminescence is generated (see subsection 2.2.1). Under this scheme, if the concentration of $Nd^{3+}$ ions was sufficiently high enough, the non-radiative delivered energy (waving arrows in **Figure 4.1a**) was enough to make the shell behave as a heating unit (see subection 2.1.1) (KUMAR et al., 2007; PAVEL et al., 2008). The $Er^{3+}$ green luminescence, in turns, provided a large thermal sensitivity to the core (DEBASU

et al., 2013; DU et al., 2014; MAURICE et al., 1995; VETRONE et al., 2010b). Thus, core/shell nano-engineering was used to combine in a single structure a heating shell (constituted by $LaF_3$ heavily doped with $Nd^{3+}$) and a thermosensitive core (consisting of an $Er^{3+}$,$Yb^{3+}$ co-doped $LaF_3$ core).

**Figure 4.1. (a)** Schematic diagram of the active-core/active-shell nanoparticles specifically designed for simultaneous heating and thermal sensing activated by 808 nm light. In this design, the shell acts as a heating center whereas the core provides thermal sensitivity to the structure. **(b)** Detail of the energy level diagrams of $Nd^{3+}$, $Yb^{3+}$ and $Er^{3+}$ ions. The heat produced by $Nd^{3+}$ ions in the shell is represented by red/yellow wave arrows whereas the green emission, resultant of the subsequent energy transfer between (i) $Nd^{3+}$ and $Yb^{3+}$ ions and (ii) between $Yb^{3+}$ and $Er^{3+}$, is represented by green arrows.

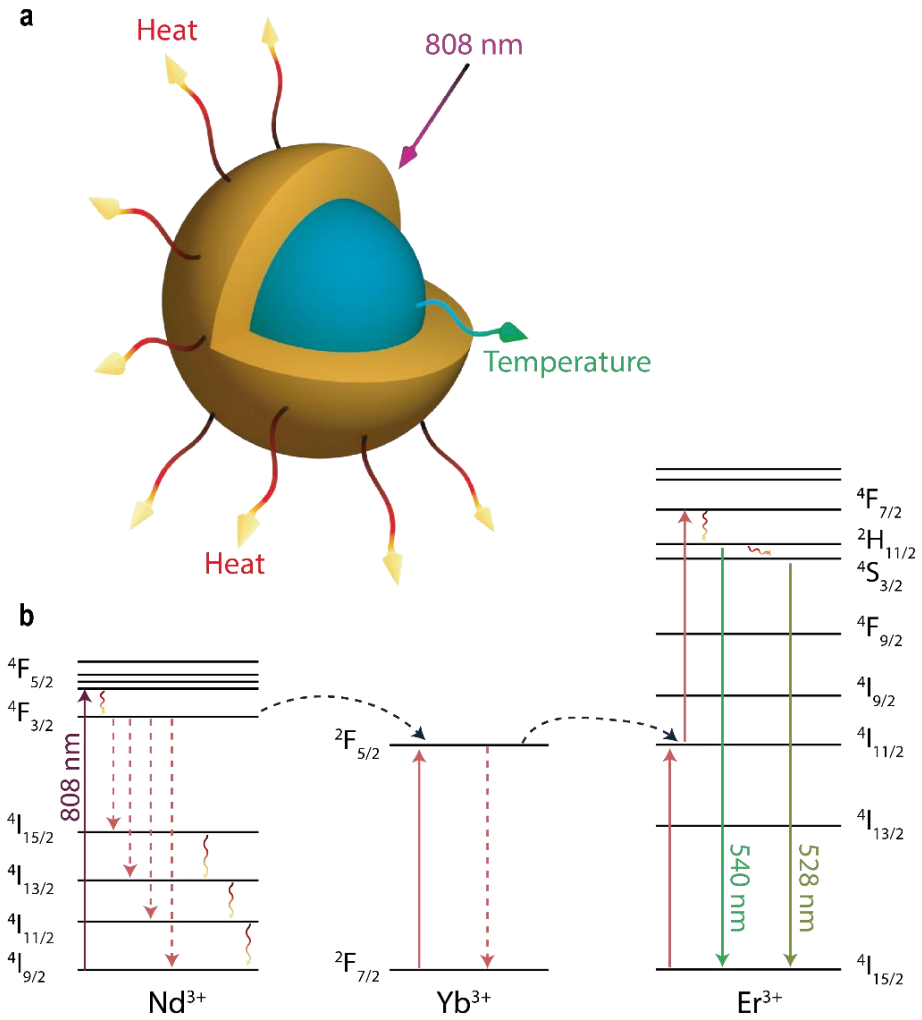

With this proposal in mind and looking for a thorough investigation, we have schematically studied the three different samples schematically drawn in **Figure 4.2**. The first sample (hereafter Er-Yb@Nd $LaF_3$ NPs) corresponded to the main proposal of this work, *i.e.* core/shell $LaF_3$ NPs in which the core was doubly doped with $Er^{3+}$ and $Yb^{3+}$ ions and the shell was singly doped with $Nd^{3+}$ ions. A second sample (hereafter Nd-Er-Yb $LaF_3$ NPs) corresponded to a simple $LaF_3$ NP triply doped with $Nd^{3+}$, $Er^{3+}$ and $Yb^{3+}$ ions (*i.e.* no ion was spatially separated from another). Finally, for the sake of comparison in time resolved fluorescence experiments, a third sample, a simple $LaF_3$ NP co-doped with $Er^{3+}$ and $Yb^{3+}$ ions (hereafter Er-Yb $LaF_3$ NPs), was also synthetized. In all of them the concentrations of $Nd^{3+}$, $Er^{3+}$ and $Yb^{3+}$ ions were respectively set to 25, 1 and 4 mol.%.

**Figure 4.2.** Schematic diagram of **(a)** Er-Yb@Nd $LaF_3$, **(b)** Er-Yb-Nd $LaF_3$ and **(c)** Er-Yb $LaF_3$ NPs.

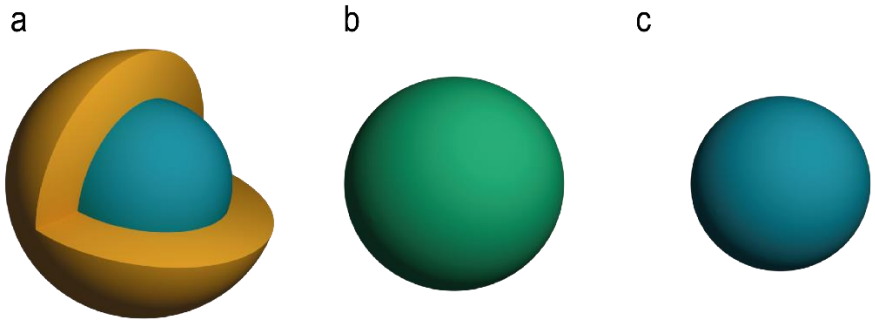


### 4.1.2. Composition and structure of Er-Yb@Nd $LaF_3$ NPs

As of first importance, we needed to experimentally verify the structure and composition of the NPs. Since the TEM images and the average diameter of the Er-Yb@Nd $LaF_3$ NPs were already included in **In this** section, we will describe the synthesis routes followed to produce the NPs studied throughout this thesis. The main properties (composition, surface coating, size, hydrodynamic diameter and potential zeta) of the NPs are indicated in Table 3.2. The transmission electron microscopy (TEM) images, from which the size was determined, are shown in **Erro! Autoreferência de indicador não válida.**. The synthesis and

basic characterization of the physicochemical properties of the NPs was carried out by different groups (see Table 3.2), which mostly aims not at manufacturing but at studying different systems for biological applications.

***Figure 3.11*a** and **Table 3.2**, we will not repeat this information here. Instead, we proceed to evidence the spatial separation between $Er^{3+}$-$Yb^{3+}$ and $Nd^{3+}$ ions by means of both EDX and EPR experiments (see Sections 3.7 and 3.8). **Figure 4.3a** shows a high resolution TEM image of a single Er-Yb@Nd $LaF_3$ NP analyzed by EDX compositional analysis. The concentration profiles corresponding to $Nd^{3+}$ and $Yb^{3+}$ ions have been superimposed to the TEM image. As it can be observed, the concentration of $Nd^{3+}$ ions remained virtually constant whereas the $Yb^{3+}$ concentration presents a clear maximum at the center of the NP. This is in excellent agreement with the expected locations of $Yb^{3+}$/$Nd^{3+}$ ions at the core/shell structure (remind **Figure 4.1a**). The EPR spectrum of the Er-Yb@Nd $LaF_3$ NPs is shown in **Figure 4.3b** together with the one corresponding to the Nd-Yb-Er $LaF_3$ NPs. As it can be observed, the Er-Yb@Nd $LaF_3$ core/shell NPs presented much more clearly resolved lines for the $Nd^{3+}$ ions than the Er-Yb-Nd $LaF_3$ NPs, and the g lines corresponding to the three ions ($Nd^{3+}$, $Yb^{3+}$, and $Er^{3+}$) can be clearly distinguished (BAKER; FORD, 1964). The relevant EPR line narrowing found for the core/shell nanoparticles, reveals a significant reduction in the magnitude of the spin coupling between the different ions and constitutes an additional proof of the spatial separation between $Nd^{3+}$ and $Er^{3+}$,$Yb^{3+}$ ions.

**Figure 4.3. (a)** High resolution TEM image of a single Er-Yb@Nd core-shell $LaF_3$ NP. The concentration profiles of both $Nd^{3+}$ and $Yb^{3+}$ ions as obtained by EDX are superimposed to the TEM image. **(b)** EPR spectra of both Er-Yb-Nd $LaF_3$ and Er-Yb@Nd $LaF_3$ NPs measured at 5 K. Dashed lines indicate the position of the g-values corresponding to $Nd^{3+}$, $Yb^{3+}$ and $Er^{3+}$ ions in $LaF_3$ single crystals.

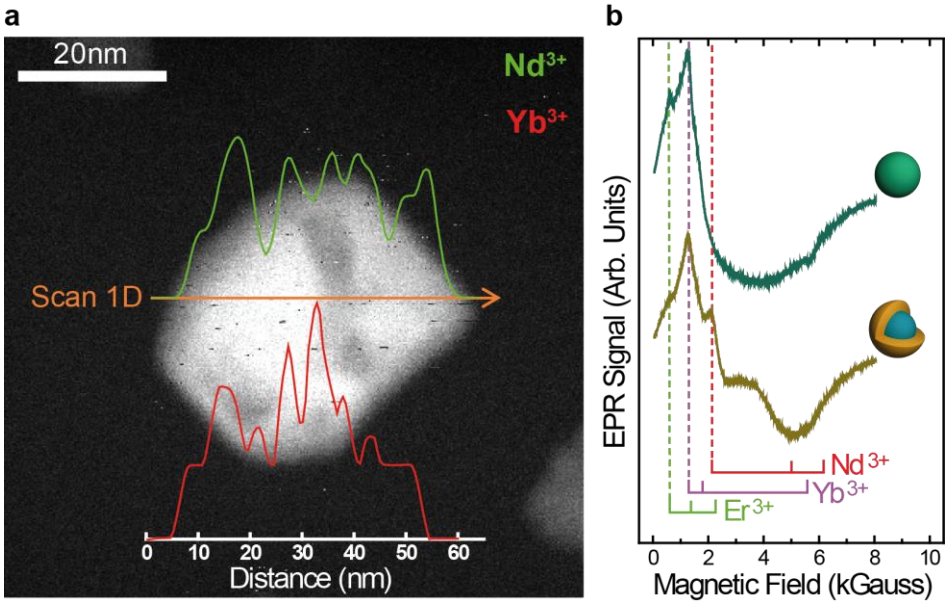


### 4.1.3. Core/shell engineering and energy transfer processes

Once the structure and composition of the NPs were verified, we investigated their spectroscopic properties. For this, we prepared two colloidal solutions containing either Er-Yb@Nd $LaF_3$ or Er-Yb-Nd $LaF_3$ NPs. At this point it is worth mentioning that they showed colloidal stability in distilled water up to particles concentrations of 2% in mass. Larger concentrations lead to particle precipitation. Consequently, all the optical measurements in aqueous solutions were performed with concentrations below 1% in mass. The solutions containing either Er-Yb@Nd $LaF_3$ or Er-Yb-Nd $LaF_3$ NPs were excited by an 808 nm laser and their subsequently generated up-conversion luminescence spectra are shown in **Figure 4.4a**.

The characteristic bands of $Er^{3+}$ ions at around 528 and 539 nm (corresponding to the $^2H_{11/2} \rightarrow {}^4I_{15/2}$ and $^4S_{3/2} \rightarrow {}^4I_{15/2}$ thermally coupled transitions) are clearly observed for Er:Yb@Nd $LaF_3$ NPs but hardly detected for Er:Yb:Nd $LaF_3$ NPs. The almost complete absence of up-converted visible luminescence of Nd-Er-Yb $LaF_3$ NPs is in agreement with the reported fluorescence quenching of $Er^{3+}$ ions caused by $Nd^{3+}$ ions in close proximity (SHAN

GUAN et al., 2012; ZHUANG et al., 2013). The core/shell NPs, on the other hand, do not provide the basis for the fluorescence-quenching of $Er^{3+}$ ions since, in this case, most of $Er^{3+}$ and $Nd^{3+}$ ions are spatially separated. In fact, fluorescence decay curves support this argument. **Figure 4.4b** includes the fluorescence decay curves corresponding to the $^4S_{3/2} \rightarrow {}^4I_{15/2}$ $Er^{3+}$ transition as obtained for Er-Yb-$LaF_3$ and Er-Yb@Nd $LaF_3$ NPs. For the sake of comparison, the decay curve obtained with Er:Yb:$LaF_3$ NPs has also been included. In the absence of $Nd^{3+}$ ions, the average fluorescence lifetime of the $^4S_{3/2}$ state was found to be $\tau_{Er}^{Er:Yb}$= 168 μs. This value decreases down to $\tau_{Er}^{Er:Yb:Nd}$ = 4 μs for those nanoparticles where $Er^{3+}$, $Yb^{3+}$ and $Nd^{3+}$ ions coexist in the same volume. In a first order approximation, the average $Er^{3+} \rightarrow Nd^{3+}$ ET efficiency in Er-Yb-Nd $LaF_3$ NPs ($\eta_t^{Er-Yb-Nd}$) was estimated to be:

$$\eta_t^{Er-Yb-Nd}(Er^{3+} \rightarrow Nd^{3+}) = 1 - \left(\tau_{Er}^{Er-Yb-Nd}/\tau_{Er}^{Er-Yb}\right) = 98\%$$

**Equation 4.1**

**Figure 4.4. (a)** Room temperature upconversion spectra generated by simple and core/shell samples when optically excited with an 808 nm focused laser beam. **(b)** Fluorescence decay curves corresponding to the emission from the $^2H_{11/2}$ : $^4S_{3/2}$ thermally coupled levels of erbium ions after 488 nm optical ($Er^{3+}$) excitation. **(c)** Fluorescence decay curves corresponding to the $^4F_{3/2}$ $Nd^{3+}$ level as obtained under 808 nm optical excitation.

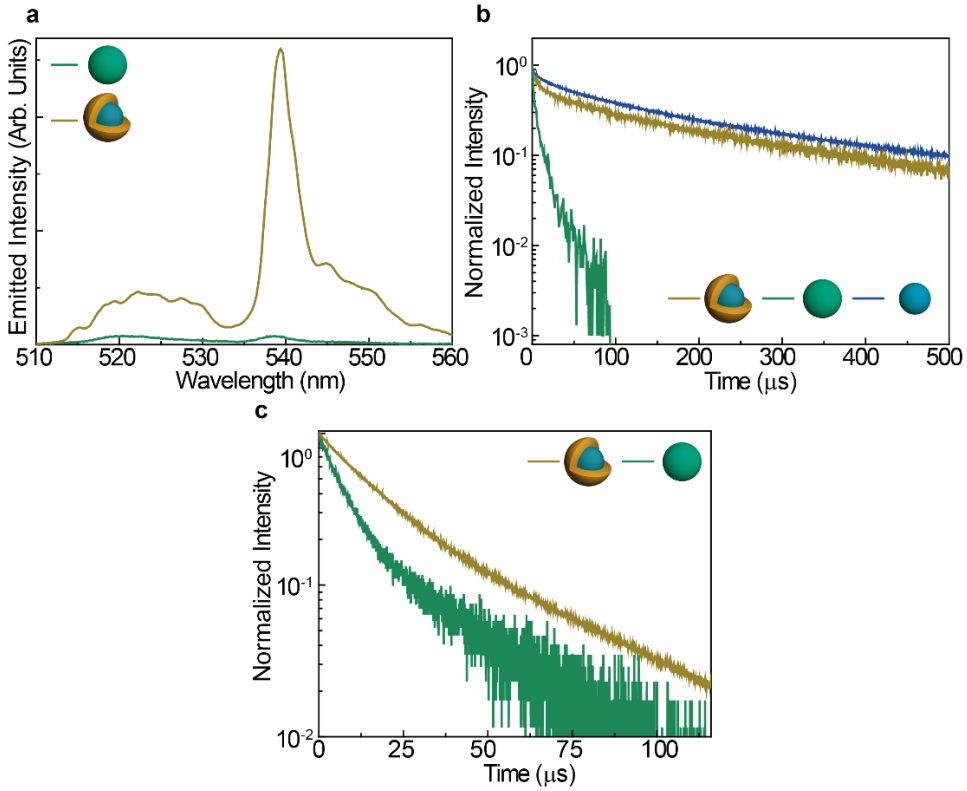


This value, in turns, indicated that an almost complete quenching of the erbium luminescence was taking place, which goes in agreement with **Figure 4.4a**. In the case of Er-Yb@Nd $LaF_3$ core-shell NPs, on the other hand, the erbium fluorescence lifetime was found to be $\tau_{Er}^{Er:Yb@Nd} = 122$ μs , so that the average $Er^{3+} \rightarrow Nd^{3+}$ ET efficiency was estimated to be:

$$\eta_t^{Er-Yb@Nd}(Er^{3+} \rightarrow Nd^{3+}) = 1 - \left(\tau_{Er}^{Er-Yb@Nd}/\tau_{Er}^{Er-Yb}\right) = 27\%$$

**Equation 4.2**

It is worth pointing out that this value corresponds to the average value over all the erbium ions inside the NPs. We must remind that only $Er^{3+}$ ions at the core/shell interface can efficiently interact with $Nd^{3+}$ ions (see **Figure 4.1a**), which explains the reduction in the value of $Er^{3+} \rightarrow Nd^{3+}$ ET efficiency.

Not only there is an $Er^{3+} \rightarrow Nd^{3+}$ ET but, according to the emission spectra and fluorescence images included in **Figure 4.4a** and **Figure 4.4b**, there is a

relevant ET from the 808 nm excited neodymium ions at the shell to the $Yb^{3+}$-$Er^{3+}$ ions within the core. In order to estimate the efficiency of such ET processes, the fluorescence lifetimes of the $^4F_{3/2}$ metastable state of $Nd^{3+}$ was measured. The decays curves obtained with both Er-Yb@Nd and Er-Yb-Nd $LaF_3$ NPs can be found in **Figure 4.4c**. From experimental data the average fluorescence lifetime of the $^4F_{3/2}$ metastable state of $Nd^{3+}$ in Er-Yb@Nd and Er-Yb-Nd $LaF_3$ NPs were found to be $\tau_{Nd}^{Er:Yb@Nd}$= 23 μs and $\tau_{Nd}^{Er:Yb:Nd}$= 10 μs, respectively while works in literature reported a fluorescence lifetime close to $\tau_{Nd}$ = 40 μs for 25 mol% $Nd^{3+}$ doped core/shell $LaF_3$ NPs. This lifetime reduction unequivocally indicated the presence of an ET process from neodymium ions to erbium and ytterbium ions. At this point it is worth stating that even though $Nd^{3+} \rightarrow Yb^{3+}$ ET processes are expected to be dominant, the existence of $Nd^{3+} \rightarrow Er^{3+}$ ET processes had been demonstrated and, therefore, cannot be disregarded (BARBOSA-GARCÍA et al., 1997; DOKE et al., 2013; ROTMAN, 1990). Hence, we estimate that both $Nd^{3+} \rightarrow Yb^{3+}$ and $Nd^{3+} \rightarrow Er^{3+}$ ET could take place in our structures and, consequently, hereafter we will talk about an overall $Nd^{3+} \rightarrow Er^{3+}$:$Yb^{3+}$ ET process. The overall $Nd^{3+} \rightarrow Er^{3+}$:$Yb^{3+}$ ET efficiencies in Er-Yb@Nd and Er-Yb-Nd $LaF_3$ NPs were estimated to be (in a first order approximation):

$$\eta_t^{Er-Yb@Nd}\,(Nd^{3+} \rightarrow Er^{3+} - Yb^{3+}) = 1 - (\tau_{Nd}^{Er-Yb@Nd}/\tau_{Nd}\,) \;= 42\%$$

**Equation 4.3**

$$\eta_t^{Er-Yb-Nd}\,(Nd^{3+} \rightarrow Er^{3+} - Yb^{3+}) = 1 - (\tau_{Nd}^{Er-Yb-Nd}/\tau_{Nd}\,) \;= 75\%$$

**Equation 4.4**

As it was also observed for the $Er^{3+} \rightarrow Nd^{3+}$ ET, the spatial coexistence of $Nd^{3+}$ and $Yb^{3+}$-$Er^{3+}$ ions in the Er-Yb-Nd $LaF_3$ NPs leads to a larger $Nd^{3+} \rightarrow Er^{3+}$-$Yb^{3+}$ ET efficiency if compared to the core/shell NPs. The reduced $Nd^{3+} \rightarrow Er^{3+}$-$Yb^{3+}$ ET efficiency in the core/shell structured NPs results in a more intense 808 nm excited up-converted emission due to the spatial separation between $Nd^{3+}$ (core) and $Er^{3+}$ (shell) ions which avoids the luminescence quenching of erbium ions, as discussed above.

### 4.1.4. Heating and thermal sensing capabilities of Er-Yb@Nd $LaF_3$ NPs

**Figure 4.5. (a)** Upconversion emission spectra generated by Er-Yb@Nd $LaF_3$ NPs under 808 nm laser excitation as obtained at two different temperatures. The inset shows the temperature variation of the ratio, R, between the emitted intensities at 528 and 539 nm. Dots are experimental data and the dashed line is a linear fit. **(b)** 808 nm laser induced heating produced in Er-Yb co-doped single, Er-Yb-Nd co-doped single and Er-Yb@Nd core/shell NPs as a function of the 808 nm laser power. Dots are experimental data and dashed lines are linear fits. The inset shows the thermal images of Eppendorf tubes containing either Er-Yb, Er-Yb-Nd or Er-Yb@Nd $LaF_3$ NPs as obtained under 808 nm, 1.38 W laser excitation power.

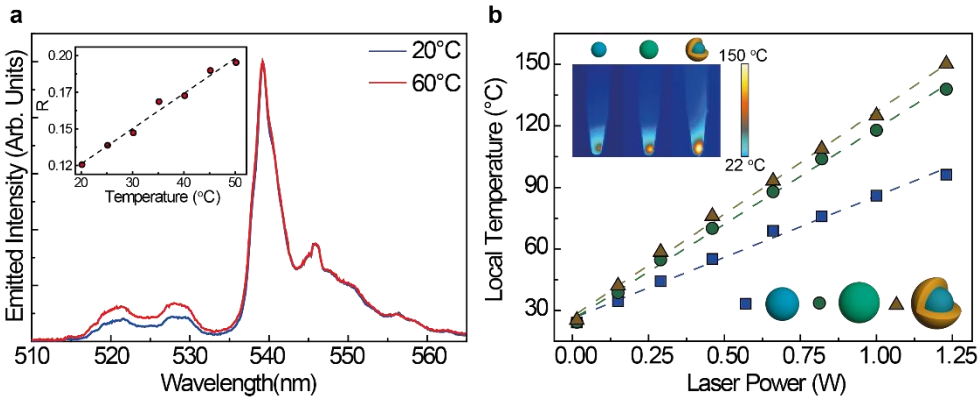


Once demonstrated the necessity of the core/shell engineering for the green emission of $Er^{3+}$ ions in a system triply doped with $Er^{3+}$, $Yb^{3+}$ and $Nd^{3+}$ under 808 nm excitation, the heating and sensing capabilities of the proposed Er-Yb@Nd $LaF_3$ NPs were investigated.

As previously mentioned, the thermal sensing capability of the core/shell Er-Yb@Nd $LaF_3$ NPs under single beam 808 nm excitation comes from the green up-converted emission generated from the $^2H_{11/2}$ and $^4S_{3/2}$ states of erbium ions. Due to the fact that these are thermally coupled states, the spectral shape of the luminescence spectrum is expected to be temperature dependent (see subsection 2.2.1). **Figure 4.5a** shows the green emission spectra as obtained at two different temperatures. As observed, the relative contribution of the 515-530 nm emission increases with temperature due to the thermally induced population of the $^2H_{11/2}$ state (SAÏDI et al., 2009; VETRONE et al., 2010b). Thus,

the graphical information suggests the intensity ratio between the 515-530 and 530-560 nm bands (hereafter denoted as R) as the most obvious thermometric parameter. Its temperature dependence is included as an inset in **Figure 4.5a** from which a pseudo-linear relation was found in the biophysical temperature range. From this data, the relative thermal sensitivity (see Section 2.2.4.1) of the core/shell structures was estimated to be $S_R$ = 1.6 x $10^{-2}$ $°C^{-1}$ at 30°C. This value was comparable to the thermal sensitivities widely reported for other $Er^{3+}$ doped systems successfully used for accurate intracellular thermal sensing (JAQUE et al., 2014b; SAVCHUK et al., 2014).

We now recall that the temperature sensitive $Er^{3+}$ doped core was surrounded by a heavily $Nd^{3+}$ doped shell that was specifically designed to behave as a double acceptor and a heating layer. At this point, previous works had already concluded that the pump-to-heat conversion efficiency of $Nd^{3+}$ doped $LaF_3$ nanoparticles was ascribed to the high concentration of neodymium ions inside the $LaF_3$ host (ROCHA et al., 2014a). In order to corroborate the dominant role played by the presence of $Nd^{3+}$ ions in the heating capacity of our structures we optically excited the three samples (in powder) described in Section 4.1.1 with an 808 nm laser beam. The inset in **Figure 4.5b** contains the thermal images (obtained with a thermographic camera as described in Section 3.3) corresponding to each one of those samples. For all cases, the temperature increment was linearly correlated to the laser power (see **Figure 4.5b**). The important role of $Nd^{3+}$ ions was evidenced after observing that the heating capacity of Er-Yb $LaF_3$ NPs was significantly smaller than the ones of Er-Yb-Nd $LaF_3$ and Er-Yb@Nd $LaF_3$ NPs. Still, the Er-Yb $LaF_3$ NPs presented a non-negligible slope in **Figure 4.5b**. We attribute this to the residual absorption of $Er^{3+}$ ions at 808 nm and to the subsequent activation of non-radiative (multiphoton) decay processes. In any case, even though heating was also possible in the absence of $Nd^{3+}$ ions, their presence proved to be an extremely necessary factor for the improvement of the light-to-heat conversion efficiency. Indeed, pump-induced heating was found to be 110% larger in $Nd^{3+}$ doped

core/shell structures than in single Er-Yb doped NPs. Hence, the experimental data revealed the $Nd^{3+}$ ions content as the main responsible source for the pump-induced heating.

Even though we safely attributed the heating capacity of the nanostructures to the high concentration of $Nd^{3+}$ ions, we still needed to address the question of why the light-to-heat conversion efficiency of Er-Yb@Nd $LaF_3$ NPs was slightly higher (≈10%) than the one of Er-Yb-Nd $LaF_3$ NPs (**Figure 4.5b**). A tentative explanation was given. As previously mentioned, heat production in our structures was ascribed to the presence of non-radiative de-excitations from the $^4F_{3/2}$ metastable state of $Nd^{3+}$ ions. The produced heat, therefore, could be assumed to be proportional to the non-radiative de-excitation rate and to the population of this level. The activation of $Nd^{3+} \rightarrow Yb^{3+}$,$Er^{3+}$ ET caused a net reduction in its population. If, in a first order approximation, the non-radiative de-excitation rate from the $^4F_{3/2}$ metastable state is assumed to be unaffected by the presence of $Er^{3+}$ and $Yb^{3+}$ ions, then the presence of $Nd^{3+} \rightarrow Yb^{3+}$,$Er^{3+}$ ET leads to a net reduction in the pump-to-heat conversion efficiency. The larger is the $Nd^{3+} \rightarrow Yb^{3+}$,$Er^{3+}$ ET efficiency the larger would be the reduction in the $^4F_{3/2}$ metastable state population and, hence, the larger will be the reduction in the heating efficiency. In other words, structures with larger $Nd^{3+} \rightarrow Yb^{3+}$,$Er^{3+}$ ET efficiencies would show reduced pump-to-heat conversion efficiencies. As it was demonstrated in **Figure 4.4**, the Er:Yb@Nd $LaF_3$ core-shell structures showed lower $Nd^{3+} \rightarrow Yb^{3+}$,$Er^{3+}$ ET efficiencies than those obtained for Er:Yb:Nd $LaF_3$ NPs. Consequently, they were expected to show larger pump-to-heat conversion efficiencies and, in fact, this was exactly what was found in the experimental data included in **Figure 4.5b**.

### 4.1.5. *In vitro* and *ex vivo* applicability of Er-Yb@Nd $LaF_3$ NPs in controlled photothermal processes

Once demonstrated the dual capability (heating + thermometry) of the Er:Yb@Nd $LaF_3$ core/shell NPs, their potential application in controlled

photothermal processes was evaluated. For this, two simple experiments, aiming to constitute clear proofs of concepts, were designed. The first experiment aimed to evaluate the performance of Er-Yb@Nd $LaF_3$ NPs in aqueous media in order to mimic *in vitro* conditions. For this purpose, an aqueous solution containing Er-Yb@Nd $LaF_3$ core/shell NPs was inserted in a 100 μm height micro-chamber (Ibidi GmbH) which, in turns, was placed on the experimental setup described in Section 3.1.1.

According to the discussion of the previous subsection, the Er-Yb@Nd $LaF_3$ NPs within the 808 nm beam could partially convert light into heat. Therefore, under the conditions of this first experiment, a well localized temperature increment in the colloidal solution was produced. However, since the Er-Yb@Nd $LaF_3$ NPs were also endowed with a thermal sensing capability, it was possible to estimate the amount of this heating at the laser focus by means of the green luminescence simultaneously generated by the Er-Yb@Nd $LaF_3$ NPs at the volume. **Figure 4.6a** shows the on-focus heating as a function of the 808 nm laser power. In good accordance with well-established models describing laser induced thermal loading effects in micro-fluidics, a pseudo-linear relation was observed (DEL ROSAL et al., 2014).

It is worth noting that this approach constituted a unique way of accessing the on-focus temperature in laser heated micro-fluidics. Conventional approaches, such as the use of infrared thermographic cameras, were not valid as they provided not the on-focus (intra-channel) temperature but, instead, the temperature on the surface of the micro-fluidic device. **Figure 4.6a** therefore, demonstrates how Er-Yb@Nd $LaF_3$ NPs could produce self-monitored local heating in aqueous media, revealing laser-induced temperature increments as large as 6 °C for sub-100 mW 808 nm laser powers. Such heating would be enough to perform real *in vitro* PTTs and, therefore, the proposed Er-Yb@Nd $LaF_3$ NPs emerged as very promising nanostructures for real *in vitro* controlled PTTs.

**Figure 4.6. (a)** On-focus temperature increment in the aqueous solution as a function of the 808 nm laser power. Dots are experimental data obtained from the spectral analysis of $Er^{3+}$ emission and the dashed line is a linear fit. **(b)** Surface and subcutaneous temperatures as obtained for different 808 nm laser powers. Dots are experimental data and dashed lines are linear fits. Notice that for laser power lower than 90mW, the NPs fluorescence was too weak to be considered.

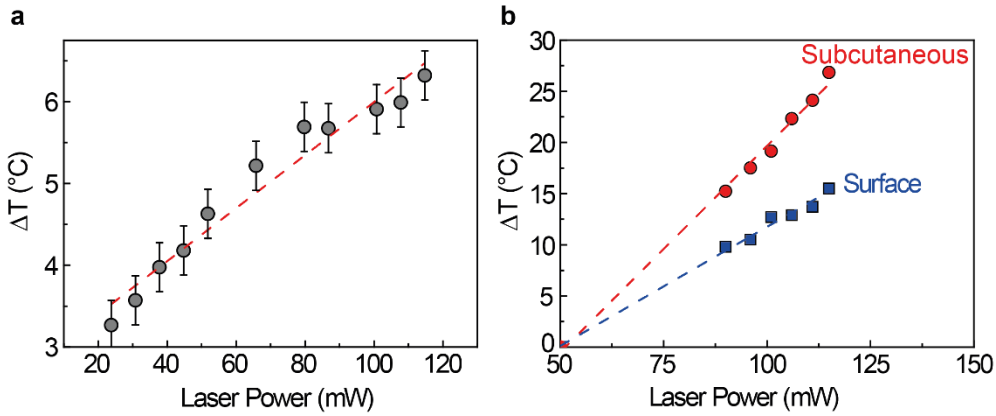


The second experiment, on the other hand, explored the potential use of Er-Yb@Nd $LaF_3$ NPs for *in vivo* applications by means of an *ex vivo* proof of concept. An amount of 0.2 ml of an aqueous solution containing Er-Yb@Nd $LaF_3$ NPs into a chicken breast. The injection depth was estimated to be around 1.0 mm. Optical excitation and subsequent visible luminescence collection were both performed by using a single long working distance objective (Section 3.1.1). Once again, the spectral analysis of the subcutaneous NPs fluorescence was used to estimate the injection's temperature. An infrared thermographic camera was coupled to the optical set-up (as in Section 3.3) with the aim of recording the superficial temperature of the tissue and to evidence its difference to the subcutaneous one (the former being expected to be lower due to heat diffusion processes) (CARRASCO et al., 2015; ROCHA et al., 2014a). The steady state subcutaneous and surface temperatures were recorded for different 808 nm laser powers and in both cases a linear relation was experimentally found (**Figure 4.6b**). As expected, there were remarkable differences between the subcutaneous and the superficial temperatures. In fact, this was found to be as large as 38%. Although experimental data included in **Figure 4.6b** reveals the potential of Er-Yb@Nd

$LaF_3$ for thermally controlled subcutaneous PTTs, it should be mentioned that their application would be limited by the optical penetration of the green $Er^{3+}$ fluorescence (1-2 mm depth) into tissues. For the performance of controlled PTTs at larger depths, the heating/sensing core/shell structure should work (emit) in any of the so-called biological windows (see Section 1.1.1). In fact, that was exactly the problem faced in the design of the NPs described in the following section.

## 4.2. Core/shell nanoparticles for subcutaneous heating and thermal sensing in BW-II

Even though we demonstrated the possibility of constructing single NPs capable of both heating and thermal sensing by means of the core/shell nanoengineering, their potential to work subcutaneously was still something disputed. And this was so because their operation spectral range was found in the visible spectrum domain, where optical penetration into tissues is minimal. As stated in Section 1.1.1, in order to avoid this limitation, it is necessary to shift their operation spectral range from the visible to the spectral infrared ranges known as biological windows. In particular, the applicability in BW-II would open up the possibility of not only deep tissue imaging but also of high contrast, auto-fluorescence free *in vivo* fluorescence thermal sensing (CASSETTE et al., 2013; GUI et al., 2015; HEMMER et al., 2016; HONG et al., 2012; QUEK; LEONG, 2012; ROBINSON et al., 2012; VAN VEGGEL, 2014; WELSHER; SHERLOCK; DAI, 2011). In this sense, the design and synthesis of a single multifunctional NP capable of simultaneous heating and thermal sensing, operating in BW-II under 808 nm laser excitation, appeared to be especially demanding. The manner by which one could achieve this is what will be described in the present section.

### 4.2.1. Proposed NPs (Yb@Nd* LaF3 NPs)

**Figure 4.7. (a)** Schematic representation of the proposed Yb@Nd* $LaF_3$ NPs. **(b)** Simplified energy scheme of the $Nd^{3+}$ and $Yb^{3+}$ emitting centers representing

excitation and radiative decays (full lines) and possible ion-ion energy transfer paths (curved lines).

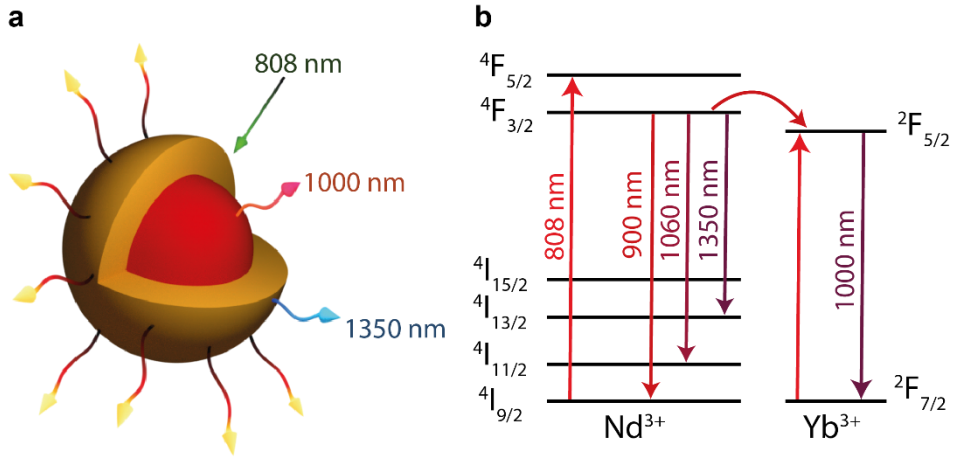


The multifunctional agent that we proposed aimed to join the heating capacity of heavily $Nd^{3+}$ doped $LaF_3$ NPs and the infrared luminescence thermal sensing of $Nd^{3+}$,$Yb^{3+}$ co-doped core/shell $LaF_3$ NPs (which is described in much more details in Section 5.1) in a single nanostructure. The proposed NPs were based on a core/shell structure with an $Yb^{3+}$ doped core (concentration of 10 mol. %) and a highly $Nd^{3+}$ doped shell (concentration of 25 mol. %). Both ions were spatially separated by selective doping during the synthesis procedure (Section 3.9.2.2). A schematic representation of those NPs (hereafter Yb@Nd* $LaF_3$ NPs) is depicted in **Figure 4.7a**.

Under this proposal the shell acted as a donor unit absorbing the 808 nm radiation through the $^4I_{9/2} \rightarrow {}^4F_{5/2}$ $Nd^{3+}$ absorption. Then, a rapid phonon-assisted relaxation to the metastable $^4F_{3/2}$ state took place. Once at the metastable state, it was possible to have radiative de-excitation (solid lines in **Figure 4.7b**) but since, in our case, a high concentration of $Nd^{3+}$ ions was present in the shell, non-radiative de-excitations were expected to be dominant over radiative ones and, consequently, the shell became a heating unit surrounding the core (indicated by the red contour in **Figure 4.7a**). Additionally, phonon-assisted cross relaxation and energy migration to killer impurities might have

played an important role in the heating process (CARRASCO et al., 2015). Simultaneously, energy transfer processes at the core/shell interface led to a relaxation of $Nd^{3+}$ ions down to their ground state and to a simultaneous excitation of $Yb^{3+}$ ions from the ground state to the $^2F_{5/2}$ excited state, from which infrared emission was produced (see dashed curved arrow in **Figure 4.7b**).

The attentive reader will notice that, under this proposal, the heating capacity of the NPs is conferred by the same principles described in Section 4.1 for the heating shell. The thermal sensing capability, on the other hand, has very different foundations. At this point, for the sake of prioritizing the focus of the present section, the foundations for the thermal sensing ability will only be briefly described. A lengthy and much more satisfying explanation for the temperature dependent ET processes is given in Section 5.1, where Yb@Nd $LaF_3$ NPs were used only for thermometry. In simple terms, the thermal sensing ability comes from the fact that the relative contribution of $Nd^{3+}$ and $Yb^{3+}$ emissions to the overall emission of the core/shell NPs depends on the $Nd^{3+} \rightarrow Yb^{3+}$ energy transfer efficiency as well as on the back transfer which are both expected to be temperature dependent (DE SOUSA et al., 2001; GONZÁLEZ-PÉREZ et al., 2007).

### 4.2.2. Structure and composition of Yb@Nd* $LaF_3$ NPs

By analyzing the results from TEM experiments carried out in both simple and core/shell $LaF_3$ NPs, we have estimated a core diameter of 24 nm (see **Table *3.2***). Additionally, the core/shell nature of the $LaF_3$ NPs synthetized by the adopted procedure was demonstrated by both Energy-dispersive X-Ray (EDX) and Electron Paramagnetic Resonance (EPR) techniques (see Section 5.1).

### 4.2.3. Heating and thermal sensing capabilities of Yb@Nd* $LaF_3$ NPs

In order to evaluate the thermal sensing capability of the Yb@Nd* $LaF_3$ NPs, the temperature dependence of their emission spectra generated under 808 nm excitation was investigated in the 15-50 $^oC$ range (**Figure 4.8a**). The fluorescence at each temperature was collected by using the optical setup described in Section

3.1.1. These measurements had to be performed under low excitation power density (0.2 W.cm$^{-2}$) in order to keep self-heating effects at minimum (a caution that must always be taken with NPs supposed to convert light into heat). As it can be seen, the contribution of $Yb^{3+}$ ions to the overall emission spectra decreased with increasing temperature - a result that goes in agreement with what is described in Section 5.1. This graphical information opens up the possibility of using the ratio between the emitted intensity of $Nd^{3+}$ ions at 1350 nm ($^4F_{3/2} \rightarrow {}^4I_{13/2}$) and that of $Yb^{3+}$ ions at around 1000 nm ($^2F_{5/2} \rightarrow {}^2F_{7/2}$) as a thermometric parameter. **Figure 4.8b** shows the temperature dependence of the intensity ratio $\Delta = I_{Nd}/I_{Yb}$ where $I_{Nd}$ and $I_{Yb}$ are defined as the emitted intensities at 1350 and 1000 nm, respectively. The error bars are associated with the experimental uncertainty in the determination of the luminescence intensity ratio. A linear fit to the experimental data allowed us to estimate the relative thermal sensitivity of our NPs (see Section 2.2.4.1) and provided a value of $S_r$ = 0.74 $\pm$ 0.02 % $^oC^{-1}$ at 20 $^o$C. A remarkable value if compared with the relative thermal sensitivities reported for other luminescent NThs operating in the II-BW prior to the development of this thesis (CERÓN et al., 2015; ROCHA et al., 2013; XIMENDES et al., 2016b).

According to the discussion of Section 4.1, a large concentration of $Nd^{3+}$ ions in the shell is expected to provide heating capabilities to the nanostructure. In order to corroborate this possibility for the NPs proposed in this section, a simple control experiment was conceived. Different core/shell NPs presenting the same $Yb^{3+}$ concentration into the core (10 mol. %) and different $Nd^{3+}$ concentrations into the shell (0, 25 and 40 mol. %) were exposed to an 808 nm laser radiation (with a power density of 3.4 W.cm$^{-2}$). The subsequent temperature variations were observed by infrared thermography (as described in Section 3.3). In order to have a control reference, a measurement using only the holder was also performed. The thermal images corresponding to the steady state temperatures of the NPs are presented in **Figure 4.8c**. As it can be seen, the temperature of the NPs, at a fixed laser power, increases with the $Nd^{3+}$ concentration into the shell.

This can be well explained by the fact that the larger the $Nd^{3+}$concentration in the system is, the greater is the non-radiative delivered energy (see Section 2.1.1) (PAVEL et al., 2008).

**Figure 4.8. (a)** Emission spectra of Yb@Nd* $LaF_3$ NPs obtained at 15, 30 and 50 °C under 808 nm excitation. **(b)** Calibration (red circles) and sensitivity (orange squares) curves of Yb@Nd* $LaF_3$ NPs. Dots are experimental values, and the line represent the best fit to the experimental data using a linear function. Power density used during calibration experiments was set to be 0.2 W/cm². Error bars are associated with the experimental uncertainty in the determination of the luminescence intensity ratio. **(c)** Thermal images of powder containing NPs with different $Nd^{3+}$ concentration as obtained under 808 nm excitation and a laser power density of 3.4 W/cm². Control corresponds to a microscope slide without Yb@Nd* $LaF_3$ NPs. **(d)** Temperature variation of Yb@Nd* $LaF_3$ NPs under different laser power densities obtained with infrared thermal camera and nanothermometer.

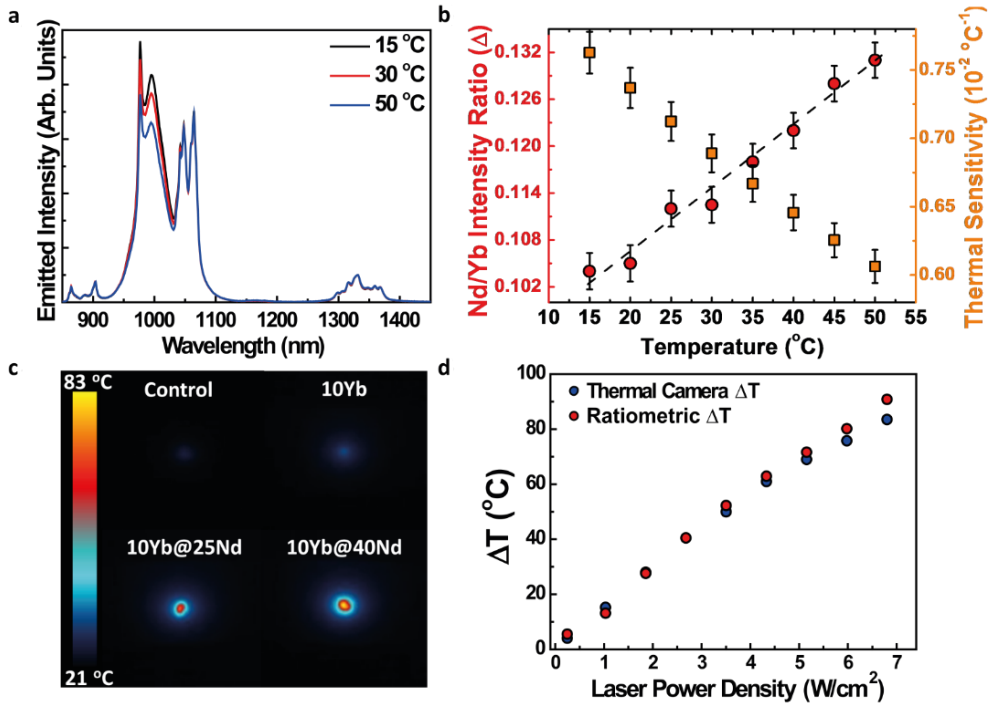


Thus, experimental data revealed the presence of $Nd^{3+}$ ions as the main responsible factor for heating. At this point, one might evaluate the extent of agreement between the values provided by the thermographic camera and by the nanothermometers themselves. For this, the Yb@Nd* $LaF_3$ NPs in powder (with concentrations of 10 mol.% for $Yb^{3+}$ ions into the core and 25 mol. % for

$Nd^{3+}$ ions into the shell) were exposed to an 808 nm laser radiation and the temperature provided by the analysis of the luminescence of the NPs and by the thermographic camera were recorded. The results are included in **Figure 4.8c**. The differences between those measurements started to appear only for high values of laser power density (between 5.1 and 6.8 $W/cm^2$ it is possible to see differences ranging from 2.5 to 7 $^oC$).

### 4.2.4. *Ex vivo* applicability in controlled photothermal processes

**Figure 4.9. (a)** Surface and subcutaneous temperatures as obtained for different 808 nm laser power densities. Dots are experimental data and dashed lines are linear fits. **(b)** Temperature stabilization of a tissue when exposed to an incident 808nm laser beam at constant power density (1.2 $W.cm^{-2}$ and 3.5 $W.cm^{-2}$ for blue squares and red circles, respectively).

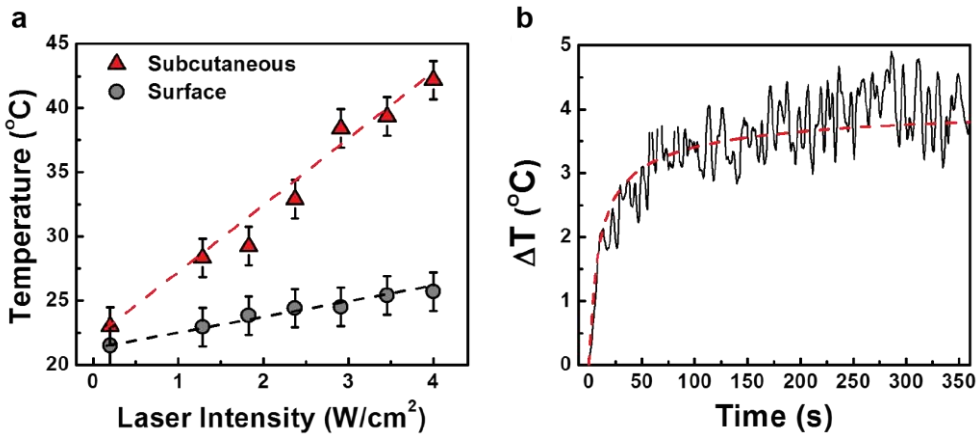


Once the multifunctionality of the Yb@Nd* $LaF_3$ core/shell NPs was experimentally evidenced, their potential application in controlled photothermal processes was evaluated. Two simple experiments, aiming to constitute clear proofs of concepts, were designed. In both experiments, an amount of 0.2 mL of an aqueous solution of Yb@Nd* $LaF_3$ NPs (10% in mass) was injected into a chicken breast sample (injection depth estimated to be close to 2 mm). An 808 nm laser beam was focused into the injection by using a single long-working distance microscope objective (40X, N.A. 0.25). The Yb@Nd* $LaF_3$ NPs would partially convert the 808 nm laser radiation into heat, producing a well localized temperature increment inside the tissue. The amount of this heating at the

injection volume was estimated by means of the intensity ratio Δ (as defined above), from the infrared spectra generated at the injection volume. For this purpose, the luminescence generated by Yb@Nd* $LaF_3$ NPs was collected using the optical setup described in Section 3.1.1.

For the first experiment, an infrared thermal camera was coupled to the optical set-up in order to record the superficial temperature of the tissue and to contrast its value with the one obtained subcutaneously. The steady state subcutaneous and surface temperatures were recorded for different 808 nm power densities and in both cases, a linear relation was experimentally found (**Figure 4.9a**). As expected, remarkable differences between subcutaneous and surface temperatures were observed. Revealing, therefore, that one cannot assume a subcutaneous temperature value equal to the one provided by the infrared thermographic camera. Thus, to achieve a reliable remote control over PTTs, the use of LNThs becomes extremely necessary.

Additionally, the same experimental set-up was used to demonstrate the capability of Yb@Nd* NPs for real time subcutaneous thermal measurements. The second experiment consisted in taking the luminescence spectra generated by the core/shell NPs in intervals of 400 ms for a time period of approximately 3 min (when thermal stabilization was achieved) at a fixed laser power density, starting on the moment the 808 nm laser was turned on. **Figure 4.9b** shows the time dependence of the subcutaneous temperature variation under two different excitation laser power densities. This temperature was obtained by computing the time evolution of the intensity ratio Δ from the subcutaneous emission spectra. In our experimental conditions, the laser spot size was orders of magnitude smaller than the heat dissipation length inside the tissue. Therefore, it was reasonable to consider the whole NP injection as a single heating point source. According to literature, the temperature rise at a distance *r* from a small source of volume generating heat at a rate Q located in a homogeneous medium without perfusion is given by $\Delta T(\vec{r}, t) = (Q/4\pi\alpha r) erfc\left(r/\sqrt{4\alpha t}\right)$, where $\alpha$ is the

thermal diffusivity of the medium (see Section 2.3.1.1). Hence, the average temperature over a sphere of radius R around the heating point source is given by **Equation 2.18**:

$$\Delta T_{avg}(t) = \Delta T_{\infty}\left(1 + \left(\frac{t}{2\tau} - 1\right)\mathrm{erf}\left(\sqrt{\frac{\tau}{t}}\right) - \sqrt{\frac{t}{\pi\tau}}\left(e^{-\frac{\tau}{t}}\right)\right)$$

Fitting the experimental data, obtained with low (1.2 W.cm$^{-2}$) and high laser power densities (3.5 W.cm$^{-2}$), to **Equation 2.18**, provided the values of ($6.6 \pm 0.6$) and ($6.0 \pm 0.3$) s for $\tau$, respectively. Considering $\alpha$ = 0.15 mm$^2$ s$^{-1}$ as the thermal diffusivity of the tissue, we obtain R = $2.0 \pm 0.1$ for 1.2 W.cm$^{-2}$and R= $1.9 \pm 0.1$ mm for 3.5 W.cm$^{-2}$ (HUANG; LIU, 2009). These values are, indeed, close to the estimated depth of injection, *i.e.* the distance between the heating source (NP injection) and the heat sink (tissue-air interface). Thus, R defines the region where the set of NPs are simultaneously sensing temperature and meaningfully heating the medium.

Data included in **Figure 4.9** demonstrates that our core/shell NPs are capable of providing a steady state and time resolved thermal reading over a subcutaneous heating process activated by themselves, constituting, therefore, a proof for the potential of Yb@Nd* $LaF_3$ NPs for thermally controlled subcutaneous PTTs.

# 5. Core/shell NPs for studying *in vivo* subcutaneous thermal dynamics

As mentioned in the introduction, *in vivo* applications of luminescence thermometry were very limited prior to the development of this thesis. In most part this was because the majority of LNThs operated in the visible spectral range, where optical penetration into tissues is minimal. To overcome this problem, one would have to shift their operation spectral range from the visible to one or more of the three traditionally known BWs (see Section 1.1.1). According to what was previously discussed, it has been demonstrated that BW-I was suitable for effective near infrared (NIR) laser excitation while BW-II and BW-III were significantly better suited for NIR imaging at greater tissue depth, providing high signal-to-noise ratio for *in vivo* imaging by effectively filtering out autofluorescence (BENAYAS et al., 2015; CARRASCO et al., 2015; ROCHA et al., 2013; WAWRZYNCZYK et al., 2012).

With this in mind, three core/shell NPs capable of luminescent thermometry in BW-II and/or BW-III under BW-I excitation were produced and are described in the following sections. Each one of them was specifically designed to overcome a certain problem found in the field of luminescence thermometry. By successfully solving those problems, the core/shell nanoparticles clearly presented an expansion of applicability of the field.

## 5.1. Core/shell NPs for unveiling fundamental properties of living tissues

Prior to the development of the work described in this section, there weren't many LNThs operating in BW-II. As a consequence, the possibility of accessing the fundamental properties of living tissues by means of luminescence thermometry was yet to be explored. At this point, even though the suitability of BW-III had already been proposed, all the efforts of the scientific community were being directed to LNThs whose emissions were found within BW-II. The reason for that relied on the fact that this particular BW had not been extensively explored and it could just as well open up the possibility of deep tissue imaging and high spatial resolution *in vivo* thermal sensing. The requirement of emitting

in BW-II, however, was not sufficient to produce a LNTh capable of operating at a subcutaneous level. Additionally, the excitation wavelength should be optimal for biological applications. In this sense, 808 nm has been considered as the main option in this work.

Two different strategies could then be followed to synthesize 808 nm excited LNThs operating in the II-BW. The first consisted in utilizing infrared-emitting QDs with thermal reading based on either their marked thermal quenching or on their temperature-induced spectral shift (CERÓN et al., 2015; LI et al., 2007). Alternatively, single or multiple rare earth-doped NPs could also be used. In this case, however, thermal reading would be achieved by the so-called ratiometric approach, in which temperature is determined from the analysis of the relative intensities of their different emission bands/lines (see Section 2.2.2). At the this this work was still in development, subcutaneous thermal sensing with rare earth-doped LNThs in the infrared had already been demonstrated with single $Nd^{3+}$-doped NPs (BENAYAS et al., 2015; CARRASCO et al., 2015; ROCHA et al., 2013, 2014a, 2014b; WAWRZYNCZYK et al., 2012). The thermal sensing, however, was performed by analyzing emission lines found within BW-I so that the potential advantages of working in BW-II (including larger penetration depths, improved resolution and autofluorescence free measurements) were yet not fully exploited.

### 5.1.1. Proposed NPs

With this in mind, we have designed and synthesized a LNTh based on a $Nd^{3+}/Yb^{3+}$ double-doped core/shell structure in which both ions were spatially separated by selective doping during synthesis procedure (see Section 3.9.2.2). The infrared thermal sensitivity was conferred to the system due to the interaction between $Nd^{3+}$ and $Yb^{3+}$ ions at the core/shell interface.

In order to have a better understanding of the working principles behind the proposed NPs, we have synthesized three different samples (which are depicted in **Figure 5.1**): one corresponding to a simple NP and the other two

corresponding to active-core/active-shell NPs. In the simple NP (hereafter Nd-Yb $LaF_3$ NPs) both $Nd^{3+}$ and $Yb^{3+}$ ions coexisted in the same volume, whereas in the core/shell structures they were spatially separated. While the first core/shell structure had the core doped with $Nd^{3+}$ ions and the shell with $Yb^{3+}$ ions (hereafter Nd@Yb $LaF_3$ NPs), the second was constituted by a $Yb^{3+}$-doped core and a $Nd^{3+}$-doped shell (Yb@Nd $LaF_3$ NPs). The $Nd^{3+}$ and $Yb^{3+}$ concentrations were both fixed to 10 mol. % in all structures. These concentrations were chosen to optimize the overall luminescence brightness of the NPs and to get similar emission intensities from both $Nd^{3+}$ and $Yb^{3+}$ ions.

**Figure 5.1.** Scaled model of **(a)** Nd:Yb $LaF_3$ (single-core), **(b)**Yb@Nd $LaF_3$ (core/shell) and **(c)** Nd@Yb $LaF_3$ (core/shell) NPs. Upon 808 nm excitation, all the NPs present the emission bands ascribed to $Nd^{3+}$ (900, 1060, 1350 nm) and to $Yb^{3+}$ (1000 nm).

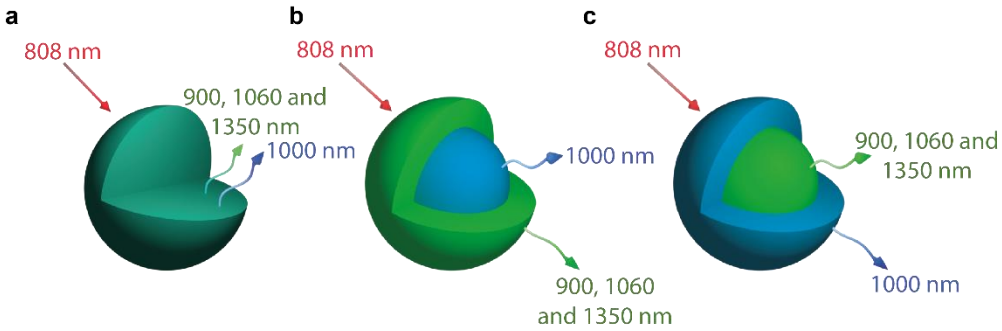


## 5.1.2. Structure and composition of Yb@Nd and Nd@Yb $LaF_3$ NPs

Size histograms were obtained by analysis of TEM images (included in **In this** section, we will describe the synthesis routes followed to produce the NPs studied throughout this thesis. The main properties (composition, surface coating, size, hydrodynamic diameter and potential zeta) of the NPs are indicated in Table 3.2. The transmission electron microscopy (TEM) images, from which the size was determined, are shown in **Erro! Autoreferência de indicador não válida.**. The synthesis and basic characterization of the physicochemical properties of the NPs was carried out by different groups (see Table 3.2), which mostly aims not at manufacturing but at studying different systems for biological applications.

***Figure 3.11*c** and **In this** section, we will describe the synthesis routes followed to produce the NPs studied throughout this thesis. The main properties (composition, surface coating, size, hydrodynamic diameter and potential zeta) of the NPs are indicated in Table 3.2. The transmission electron microscopy (TEM) images, from which the size was determined, are shown in **Erro! Autoreferência de indicador não válida.**. The synthesis and basic characterization of the physicochemical properties of the NPs was carried out by different groups (see Table 3.2), which mostly aims not at manufacturing but at studying different systems for biological applications.

***Figure 3.11*d**) and they provided values close to 24 nm for their average diameters (see **Table 3.2**).

The core/shell nature of the NPs was further evidenced by high resolution TEM and EDX studies. **Figure 5.2a** shows a high resolution TEM image of a characteristic Yb@Nd $LaF_3$ NP. The EDX concentration profiles corresponding to both $Nd^{3+}$ and $Yb^{3+}$ ions have been superimposed so that the location of the specific elements within the NP are identified. As it can be seen, the $Yb^{3+}$ ions are well localized at the central part of the profile, indicating their sole presence at the core. On the other hand, the presence of $Nd^{3+}$ ions has been found to be maximum at the edges of the NP, in accordance with the existence of a $Nd^{3+}$-doped shell. Note that, as expected, the EDX scan also reveals the existence of $Nd^{3+}$ ions at the center of the profile due to the tridimensional nature of the sample.

**Figure 5.2. (a)** High resolution TEM image of an illustrative core/shell Yb@Nd $LaF_3$ NP. The EDX concentration profiles corresponding to Nd (green) and Yb (blue) have been super-imposed so that the elements localization within the NP have been identified. **(b)** Typical EPR spectra for simple (top spectrum) and core/shell NPs (medium and bottom spectra). The g values reported for $Nd^{3+}$ (green) and $Yb^{3+}$ (blue) ions in $LaF_3$ crystals have been also included as vertical dashed lines.

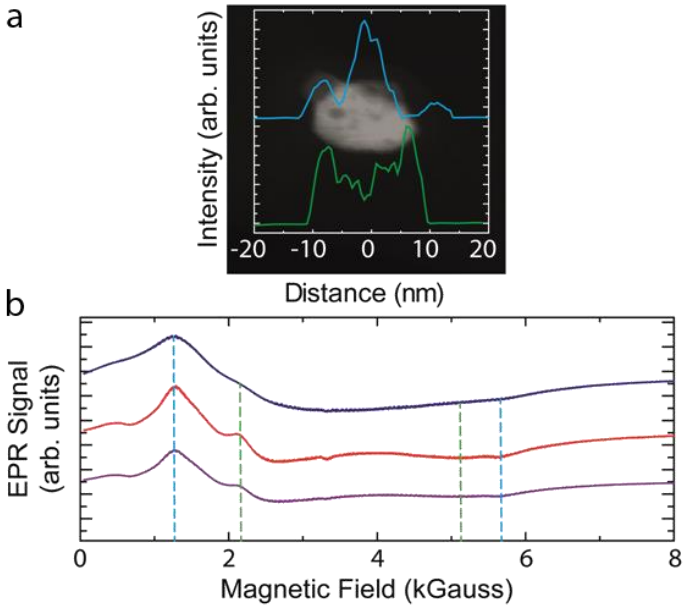


To reinforce the core/shell structure of our samples, EPR experiments were also carried out. **Figure 5.2b** shows typical spectra for simple and core/shell NPs. The *g* values reported for both $Nd^{3+}$ and $Yb^{3+}$ ions in $LaF_3$ crystals were also included, allowing for the identification of the different contributions to the net EPR spectra (BAKER; FORD, 1964). In the case of simple NPs, where there was a spatial coexistence between $Nd^{3+}$ and $Yb^{3+}$ ions, an additional contribution to the linewidth of EPR lines is observed due to the spin-spin interaction between dissimilar ions. In the core/shell structures, on the other hand, EPR lines appeared much better defined and narrower due to the reduction of spin-spin interactions as a consequence of the spatial separation between $Nd^{3+}$ and $Yb^{3+}$ ions. In this case, the EPR linewidth is mostly due to spin-spin interactions between similar ions at either the core or the shell. Thus, both EDX and EPR measurements included in **Figure 5.2** demonstrated the successful synthesis of core/shell structures with selective $Yb^{3+}$ and $Nd^{3+}$ doping.

### 5.1.3. Emission spectra and energy transfer processes

The room temperature emission spectra generated from simple and core/shell NPs under infrared 808 nm laser excitation are included in **Figure**

**5.3a**. The emission spectra included in **Figure 5.3a** have been normalized to the emission intensity at 1350 nm generated by $Nd^{3+}$ ions. Due to the negligible absorption of $Yb^{3+}$ ions at this particular wavelength, $Nd^{3+}$ ions act as the only sensitizer units. For all three NPs, the emission spectra include the characteristic emission bands of $Nd^{3+}$ ions centered at 900, 1060, and 1350 nm, assigned to the $^4F_{3/2}\rightarrow{}^4I_{9/2}$, $^4F_{3/2}\rightarrow{}^4I_{11/2}$, and $^4F_{3/2}\rightarrow{}^4I_{13/2}$ transitions, respectively. The $Nd^{3+}\rightarrow Yb^{3+}$ energy transfer is evidenced by the appearance of the $Yb^{3+}$ characteristic 970-1030 nm emission band that corresponds to the $^2F_{5/2}\rightarrow{}^2F_{7/2}$ transition. The energy transfer processes taking place under 808 nm excitation are summarized in **Figure 5.3c**. The absorption of 808 nm laser photons promotes the excitation of $Nd^{3+}$ ions from their ground state to the $^4F_{5/2}$ state. Then, a rapid phonon-assisted relaxation to the metastable $^4F_{3/2}$ state takes place. Once at the metastable state, energy diffusion between $Nd^{3+}$ ions could take place until non-radiative energy transfer processes are produced. Energy transfer leads to a relaxation of $Nd^{3+}$ ions down to their ground state and to a simultaneous excitation of $Yb^{3+}$ ions from their ground state up to the $^2F_{5/2}$ state, from which infrared emission is produced.

Although both $Nd^{3+}$ and $Yb^{3+}$ bands are present in the 850-1500 nm emission range for all three structures, their relative contribution varies from simple NPs to core/shell NPs. The emission spectrum obtained from simple Nd:Yb $LaF_3$ NPs shows dominant contribution of $Yb^{3+}$ emission, revealing an expected large $Nd^{3+}\rightarrow Yb^{3+}$ energy transfer. This, in turns, could be explained by the fact that, in simple NPs, each $Nd^{3+}$ ion is, in a good approximation, in direct contact with at least one $Yb^{3+}$ ion, leading to large ET efficiencies.

**Figure 5.3. (a)** The room temperature emission spectra of Nd@Yb $LaF_3$ (red), Yb@Nd $LaF_3$ (purple) and Nd:Yb $LaF_3$ (blue) NPs under 808 nm laser excitation (97 mW). The transitions ascribed to $Nd^{3+}$ and $Yb^{3+}$ are identified in green and blue, respectively. Spectra are normalized to their intensity at 1350 nm**. (b)** Fluorescence lifetime of the $^4F_{3/2}$ $Nd^{3+}$ emitting level of Nd@Yb (red), Yb@Nd (purple) and Nd:Yb $LaF_3$ (blue) NPs. The decay curve obtained for Nd $LaF_3$ NPs (black) is included for comparison. **(c)** Simplified energy scheme of the $Nd^{3+}$ and $Yb^{3+}$ emitting centers

representing excitation and radiative decays (full lines), non-radiative decays (curved line) and possible ion-ion energy transfer paths (dashed lines).

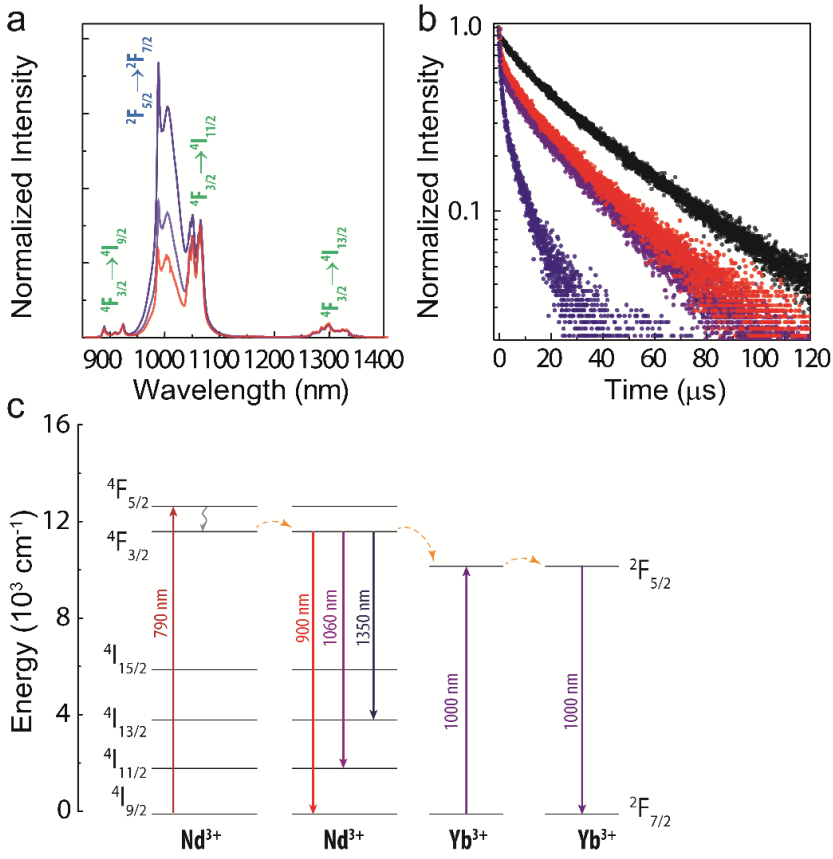


In fact, this argument is supported by the measurements of fluorescence lifetimes from the $^4F_{3/2}$ $Nd^{3+}$ emitting level (**Figure 5.3b**). For the sake of comparison, the decay curve obtained with simple $LaF_3$ NPs singly doped with $Nd^{3+}$ (hereafter Nd:$LaF_3$ NPs) is also included. Nd:$LaF_3$ NPs showed the longest lifetime ($\tau_{Nd}$= 33 μs), as well as a non-pure single-exponential decay that very likely revealed the presence of self-quenching due to $Nd^{3+}$-$Nd^{3+}$ interactions. The Nd-Yb $LaF_3$ NPs, on the other hand, presented a strong reduction in the fluorescence lifetime, $\tau_{Nd}^{Nd:Yb}$ = 3 μs, indicating an overall $Nd^{3+}$→$Yb^{3+}$ ET efficiency of $\eta_{Nd:Yb}(Nd \rightarrow Yb) = 1 - \tau_{Nd}^{Nd:Yb}/\tau_{Nd} = 90\%$. Additionally, it was evident that the fluorescence lifetime of the ($^4F_{3/2}$) state of $Nd^{3+}$ ions was substantially longer

for the core/shell structures than for the Nd:Yb simple $LaF_3$ NPs. The fluorescence lifetimes in Nd@Yb and Yb@Nd core/shell NPs have been found to be $\tau_{Nd}^{Nd@Yb}$= 24 μs and $\tau_{Nd}^{Yb@Nd}$= 25 μs, respectively. These values yielded virtually the same overall $Nd^{3+}\rightarrow Yb^{3+}$ energy transfer efficiency, *i.e.*,$\eta_{Nd@Yb}(Nd \rightarrow Yb) \cong \eta_{Yb@Nd}(Nd \rightarrow Yb) = 1 - \tau_{Nd}^{Nd@Yb}/\tau_{Nd} \cong 24\%$. Looking again at **Figure 5.3a**, one can see that the contribution of $Yb^{3+}$ ions to the infrared fluorescence was reduced in the core/shell structures. Once again confirming the of **Figure 5.3b**.

### 5.1.4. Thermal sensing capability of $Nd^{3+}/Yb^{3+}$ double-doped $LaF_3$ NPs

The ability of the $Nd^{3+}/Yb^{3+}$double-doped $LaF_3$ NPs for luminescence thermometry in BW-II was investigated by analyzing their emission spectra under 808 nm excitation as a function of temperature in the physiological temperature range. Results are summarized in **Figure 5.4**, in which the emission spectra of Nd@Yb, Yb@Nd and Nd:Yb $LaF_3$ NPs (as obtained at 10 and 50 $^{o}$C) are displayed (**Figure 5.4a**, **b** and **c**, respectively). Whereas for core/shell NPs the contribution of ytterbium ions to the overall emission spectra decreased with increasing temperature, simple Nd:Yb $LaF_3$ NPs showed an opposite behavior. The observed variations opened the avenue to use the ratio between the emitted intensity of $Nd^{3+}$ ions at ≈1.3μm ($^4F_{3/2}\rightarrow{}^4I_{13/2}$, hereafter in this chapter $I_{Nd}$) and that of $Yb^{3+}$ ions at around 1000 nm ($^2F_{5/2}\rightarrow{}^2F_{7/2}$, hereafter $I_{Yb}$) as a thermometric parameter.

**Figure 5.4d** shows the temperature variation of the intensity ratio $\Delta=I_{Nd}/I_{Yb}$ as obtained for the three samples investigated in this work. A linear calibration relation between $\Delta$ and $T$ was obtained in all three cases. A positive slope was found for the core/shell NPs whereas a negative one was found for the simple NPs. A tentative explanation for this difference is given in what follows. Previous works have evidenced that, even in the same system, temperature could either enhance or decrease the net $Nd^{3+}\rightarrow Yb^{3+}$ energy transfer efficiency depending on the precise balance between direct transfer and phonon-assisted $Nd^{3+}\leftarrow Yb^{3+}$

back transfer. When $Nd^{3+} \rightarrow Yb^{3+}$ energy transfer dominates, the $\Delta$ ratio is expected to increase with temperature (JAQUE et al., 2003). On the other hand, when phonon assisted $Nd^{3+} \leftarrow Yb^{3+}$ back transfer is the dominant mechanism then $\Delta$ is expected to decrease with temperature. According to this argument, the temperature-induced decrease of $\Delta$ in simple NPs suggests $Nd^{3+} \leftarrow Yb^{3+}$ back transfer as the dominant mechanism in these structures.

A linear fit to the experimental data included in **Figure 5.4d** allowed the estimation of the relative thermal sensitivities. The values of (0.41 ± 0.01), (0.36 ± 0.02) and (0.1 ± 0.02) % $^{o}C^{-1}$ were respectively obtained for Nd@Yb, Yb@Nd and Nd:Yb $LaF_3$ NPs at 10 $^{o}C$. A figure of merit is then included in **Figure 5.4d** to compare the performance of different thermometers operating in II-BW up until the development of this particular work (BRITES et al., 2012; COLLINS et al., 1998). At this point it should be highlighted that the same values were found when the intensity ratio $\Delta$ was computed by using the $Nd^{3+}$ emission intensity at 890 nm ($^4F_{3/2} \rightarrow {}^4I_{9/2}$ transition) or at 1060 nm ($^4F_{3/2} \rightarrow {}^4I_{11/2}$ transition).

Prior to the development of this thesis, some works had already demonstrated core/shell engineering could be used to enhance the luminescence brightness of the NPs and to tailor their spectral properties by activating or deactivating energy transfer processes between rare earth ions at core and/or shell (VETRONE et al., 2009; XIE et al., 2013). In addition to these benefits, the results obtained in the present work demonstrate that core/shell engineering can also be used to enhance the thermal sensitivity of rare earth-doped NPs (in this case, a fourfold improvement on the value of the thermal sensitivity).

**Figure 5.4.** Emission spectra of **(a)** Nd@Yb $LaF_3$, **(b)** Yb@Nd $LaF_3$, and **(c)** Nd:Yb $LaF_3$ NPs obtained at 10 and 50 °C under 808 nm excitation. **(d)** Calibration curves of Nd@Yb $LaF_3$ (red), Yb@Nd $LaF_3$ (purple), and Nd:Yb $LaF_3$ (blue) NPs. Dots are experimental Δ values, and the lines represent the best fit to the experimental data using straight lines (r2 > 0.913). **(e)** Sensitivity curves of Nd@Yb $LaF_3$ (red), Yb@Nd $LaF_3$ (purple), and Nd:Yb $LaF_3$ (blue) NPs. The sensitivity of the two other luminescent thermometers reported until now emitting in the II-BW are also

included in green and orange for comparison (CERÓN et al., 2015; MARCINIAK et al., 2015).

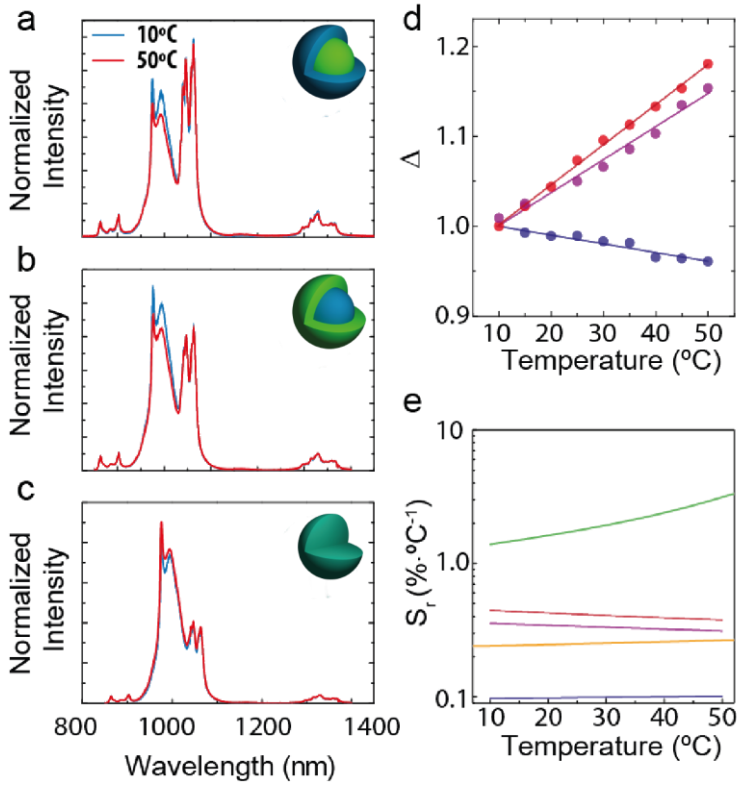


### 5.1.5. Estimation of physical properties of a living tissue by means of Nd@Yb $LaF_3$ NPs

The potential use of Nd@Yb $LaF_3$ NPs (*i.e.* the ones showing the largest thermal sensitivity) for real-time subcutaneous *in vivo* thermometry was also evaluated. In particular, their ability for an accurate measurement of subcutaneous thermal transients as a potential future theranostics tool was explored. In this subsection, subcutaneous thermal reading was not thought of as a control tool during photothermal treatments but, instead, as an alternative diagnosis tool. The basic idea behind the work is that when a tissue is undergoing a thermal relaxation (cooling in the absence of any heating source), the cooling dynamics strongly depends on the tissue properties (FURZIKOV, 1987). Thus, accurate measurements of thermal relaxation profiles would provide

information on the tissue status and, hence, could be used to detect anomalies caused by incipient diseases.

Since, the conditions of the experiment to be described imposed a low value of blood perfusion at the injection place, we assumed, as explained in Section 2.3.2.1, that the thermal relaxation of the subcutaneous tissue was governed by **Equation 2.25**:

$$T_{scut}(t) = T_s + \Delta T_{scut}\,\mathrm{erf}\left(\sqrt{\frac{\tau_{cond}}{t}}\right)$$

We note that $\tau_{\mathrm{cond}}$ is determined by the tissue's thermal properties, so that it is given by (FURZIKOV, 1987; WELCH; GEMERT, 2011):

$$\tau_{cond} = \frac{L^2}{4\,.\,\alpha_{tissue}}$$

**Equation 5.1**

where $L$ and $\alpha_{\mathrm{tissue}}$ are the characteristic length and thermal diffusivity of the tissue undergoing the thermal relaxation, respectively. The thermal diffusivity of a given tissue, in turns, depends on its thermal conductivity ($k_{tissue}$), density ($\rho_{tissue}$), and specific heat capacity ($c_{\mathrm{tissue}}$) according to (DEL ROSAL et al., 2014; VALVANO; COCHRAN; DILLER, 1985):

$$\alpha_{tissue} = \frac{k_{tissue}}{\rho_{tissue}\,c_{tissue}}$$

**Equation 5.2**

Thus, as we will address, a proper analysis of subcutaneous thermal relaxation dynamics would make possible accessing the fundamental properties of a tissue. In addition, detection of small variations in $\tau_{cond}$ would allow for the identification of possible alterations in the thermal diffusivity, specific heat, thermal conductivity or density. These variations, in turns, could be associated, for instance, with the presence of cancer tumors and other diseases.

**Figure 5.5. (a)** Fluorescence top-image of the CD1 mouse (delimited by the dashed line) where the subcutaneous injection of Nd@Yb core/shell $LaF_3$ NPs is evidenced by the bright fluorescence spot. **(b)** Digital picture of the CD1 mouse during in vivo thermal relaxation experiments.

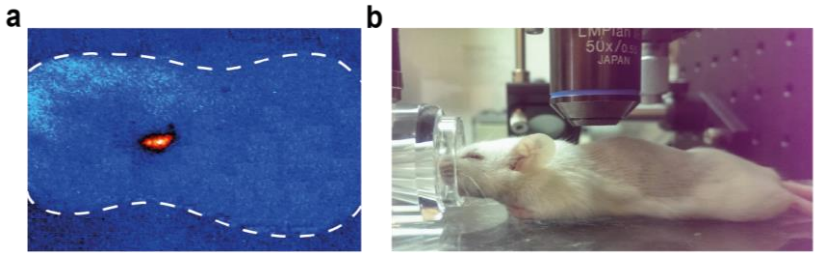


In order to demonstrate the potential use of Nd@Yb $LaF_3$ NPs for the measurement of subcutaneous thermal relaxation dynamics, a simple *in vivo* experiment was designed. A total volume of 200 μL of a PBS dispersion of Nd@Yb $LaF_3$ NPs (1 % in mass) was subcutaneously injected in a CD1 mouse. The mouse was then anesthetized and placed in a small animal chamber. The efficient subcutaneous incorporation of the Nd@Yb $LaF_3$ NPs was then confirmed by infrared (1100–1700 nm) fluorescence *in vivo* imaging. The fluorescence image included in **Figure 5.5a** was obtained by illuminating the whole mouse with an 808 nm laser beam at 0.35 W/cm$^2$. Experimental details about the small animal imaging setup can be found in Section 3.4.1.1. Even though the presence of infrared auto-fluorescence was evidenced (it is possible to intuit the shape of the CD1 mouse), its intensity was remarkably lower than that generated by the subcutaneously injected core/shell NPs, as expected when measuring in the 1100-1700 nm range (VILLA et al., 2015). Once thermal stabilization was achieved and the subcutaneous presence of the Nd@Yb $LaF_3$ NPs was confirmed, we proceeded to induce a moderate temperature increment at the injection site. Such local heating was induced by an 808 nm laser radiation incident on the CD1 mouse. The heating was mainly attributed to $Nd^{3+}$ and/or skin absorption at particular this wavelength (MAESTRO et al., 2013a). The illumination area over the skin was estimated to be $A_{808nm}$ = 5.0 ± 0.5 cm$^2$. An infrared thermographic camera was added to the setup to monitor the skin temperature. Hence, it would

be possible to differentiate the relaxation profiles at the surface and at a subcutaneous level.

**Figure 5.6. (a)** Schematic representation of the subcutaneous thermal relaxation experiments. Thermal infrared images of the CD1 mouse before **(b)** and at the end **(c)** of the heating stimulus.

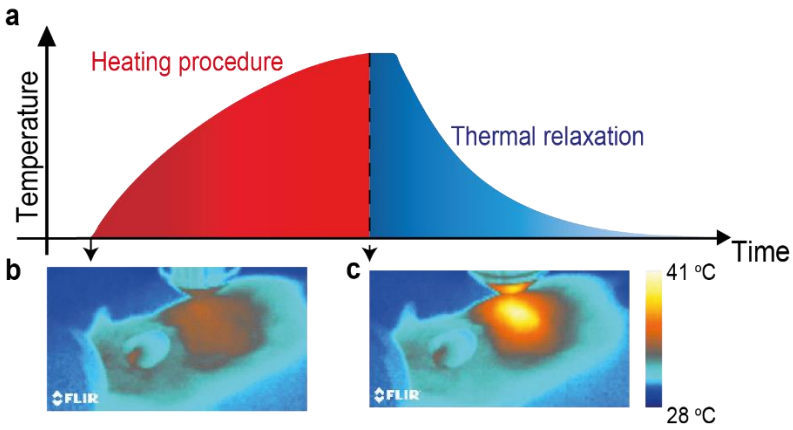


Safe heating was performed by setting the power density of the 808 nm laser beam at 0.7 W/cm$^2$ and extending the thermal treatment for 4 minutes (**Figure 5.6a**). Under these irradiation conditions the mouse surface temperature increased from 34.2 up to 40.5 $^{o}$C (**Figure 5.6b**). During the heating procedure, the strong background created by the high intensity 808 nm laser beam precluded accurate measurement of the luminescence generated by the subcutaneously injected Nd@Yb $LaF_3$ NPs. Thus, they could not be used as thermal sensors during the heating procedure. Once the heating cycle was finished (*i.e.* 808 nm laser was turned off), the thermal relaxation started and the mouse tissues gradually recovered their initial temperature (**Figure 5.6a**).

**Figure 5.7**. Time evolution of the temperatures measured by the subcutaneous luminescent thermometer (grey) and the IR thermal camera (orange). Dots are experimental subcutaneous (circles) and skin (squares) temperatures, whereas the solid line is the best fit to Equation 2.25.

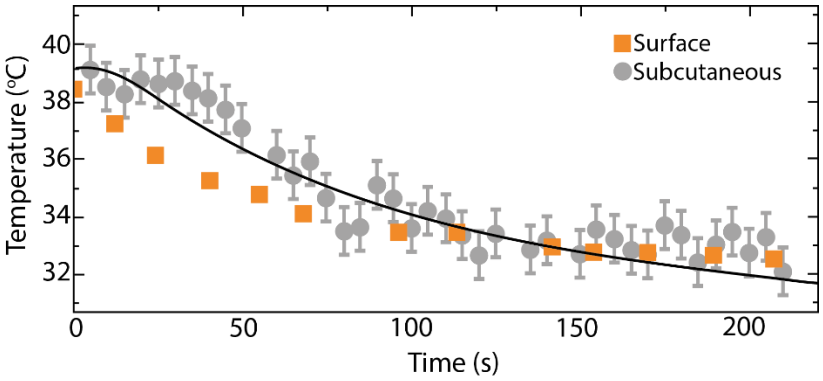


In the absence of heating 808 nm radiation, the luminescence of Nd@Yb $LaF_3$ NPs was then used to monitor the thermal dynamics of the tissue. The subcutaneous luminescence generated by Nd@Yb $LaF_3$ NPs was collected and its subsequent spectral analysis provided us the time evolution of the subcutaneous temperature through the $\Delta=I_{Nd}/I_{Yb}$ intensity ratio that, in this case, was computed with the $Nd^{3+}$ emitted intensity at 1060 nm. At this point we should note that for subcutaneous thermal measurements the calibration curve obtained for Nd@Yb $LaF_3$ NPs in aqueous medium has been used. This is a valid approach as the fluorescence properties of rare earth doped $LaF_3$ NPs are not modified when incorporated into a tissue (CARRASCO et al., 2015). Data included in **Figure 5.7** constituted the first time that thermal relaxation dynamics was measured in a living animal by luminescence thermometry. Just after the end of the heating cycle, the subcutaneously injected Nd@Yb $LaF_3$ NPs provided a thermal reading of 41±1 $^{o}$C which was in good agreement with the skin temperature provided by the thermographic camera (40.5 $^{o}$C as obtained from **Figure 5.6c**).

The time evolution of the subcutaneous temperature could be well fitted to an *erf* decay as indicated in **Equation 2.25**. **Figure 5.7** includes as solid lines the best fit of experimental data to **Equation 2.25** with $\tau_{cond}$ = 39 ± 8 s ($r^2$>0.909). Then, with this value in mind, we could compute the thermal diffusivity of the mouse tissue by setting the characteristic length/dimension, *L*. Previous works dealing with laser-induced tissue heating experiments concluded that the characteristic length of the tissue corresponded to the optical penetration depth

of the heating radiation into the tissue (KIM; GUO, 2006). In our experiments, heating was produced by an 808 nm laser beam so that $L$ could be assumed to be the penetration depth of the 808 nm radiation into tissues, $l_{808\ nm}$, so that $L \approx l_{808\ nm}$ (KIM; GUO, 2006). A value of to $L$ = 4.5 ± 0.5 mm for the penetration length at 808 nm could be found in literature (BASHKATOV et al., 2005). Hence, according to **Equation 5.1**, a tissue thermal diffusivity of $\alpha_{tissue}$ = (0.13 ± 0.04) $mm^2 \cdot s^{-1}$ was obtained. This value was in very good agreement with the one calculated through **Equation 5.2**, $\alpha$ = 0.135 $mm^2 \cdot s^{-1}$, using published data for thermal conductivity ($k_{tissue}$ = 0.5 $W \cdot m^{-1} \cdot {}^{o}C^{-1}$), density ($\rho_{tissue}$ = $10^3$ $kg \cdot m^{-3}$) and specific heat ($c_{tissue}$ = $3.7 \cdot 10^3$ $J \cdot kg^{-1} \cdot {}^{o}C^{-1}$) of animal tissues (GIERING et al., 1995). Moreover, the calculated thermal diffusivity agreed with the one reported for breast tissue at 810 nm, $\alpha$ = 0.142 $mm^2 \cdot s^{-1}$ (SHAH et al., 2001).

Besides using the thermal relaxation profile to elucidate the thermal diffusivity of tissues, one could also estimate the total thermal energy dose absorbed by the tissue. According to the definition of heat capacity, the thermal energy dose, $Q_{tissue}$, required to cause a temperature increment $\Delta T$ in a tissue of mass $m_{tissue}$ is given by:

$$Q_{tissue} = m_{tissue} \times c_{tissue} \times \Delta T$$

**Equation 5.3**

In our conditions, the mass of the tissue was estimated by assuming a tissue volume equal to the irradiated area ($A_{tissue}$ = 5.0 ± 0.5 $cm^2$) multiplied by the penetration length, $l_{808}$ nm, so that $m_{tissue} = \rho_{tissue} \times A_{tissue} \times L \cong (2.2 \pm 0.3) \times 10^{-3}$ kg. From the thermal transients included in **Figure 5.7** we approximated the total temperature increment ($\Delta T$) to ~6 $^{o}C$. Hence, a total thermal dose of $Q_{tissue}$ = 54 ± 8 J was estimated. This value can be compared to the total 808 nm laser energy deposited in the tissue, calculated as $Q_{deposited} = I_{808nm} \times \Delta t \times A_{808nm}$= 560 ± 63 J, where $I_{808nm}$ = 0.7 $W \cdot cm^{-2}$ is the 808 nm laser intensity, $\Delta t$ =160 s is the effective irradiation time and $A_{808nm}$ = (5.0 ± 0.5) $cm^2$ is the 808 nm laser spot. The effective irradiation time, in simple terms, was the time required for thermal stabilization.

Thus, the tissue absorbed only 54 J of the 560 J of the deposited laser energy, which yielded a tissue absorbance at 808 nm equal to 10 ± 2 %.

The absorption coefficient of the tissue measured in *in vivo* conditions was then estimated by applying the Lambert-Beer law (GARCÍA SOLÉ; BAUSÁ; JAQUE, 2005):

$$\alpha_{tissue}^{abs}(808nm) = \frac{1}{L}\ln\left(\frac{Q_{808nm}}{Q_{808nm} - Q_{tissue}}\right)$$

**Equation 5.4**

With this expression, a tissue absorption coefficient of $\alpha_{tissue}^{abs}$= (0.23 ± 0.05)$cm^{-1}$ was obtained. This value was in good agreement with previously published works where the same parameter was estimated to be found in the range of 0.1 to 0.4 $cm^{-1}$ depending on the fat, water and melanin content (JACQUES, 2013). Additionally the value was also close to the absorption coefficient at 808 nm of human skin, 0.35 $cm^{-1}$, as measured under *ex vivo* conditions, by A.N. Bashkatov and coauthors (BASHKATOV et al., 2005).

The attentive reader will notice that, in this section, we have used LNThs very similar to the ones described in Section 4.2. Yet their thermal sensitvity was much lower. If the intention was having an accurate thermal reading in *in vivo* conditions, why didn't we use the Yb@Nd* $LaF_3$ NPs? The answer relies on the fact that Yb@Nd* $LaF_3$ NPs were also nanoheaters. Had we injected them on a living tissue, we might have had undesired heating effects that could permanently damage the tissue and, consequently, change its fundamental properties. Additionally, on a chronological note, the work described in the presente section predated the one of 4.2.

In few words, this work demonstrated, for the first time, the possibility of using LNThs in the numerical estimation of fundamental properties of a living tissue. The next step in the path of extending the applicability of LNThs in nanomedicine would, of course, be making the connection between incipient

diseases and observed variations in these properties. This was exactly the goal of the work described in the next section.

## 5.2. Core/shell NPs for the detection of ischemic diseases in small animals

Following the principle suggested in Section 5.1, *i.e.* the estimation of physical properties of living tissues by LNThs, we went further to explore the real and important problem of disease detection in a living animal. The motivation was obvious: if demonstrated it would constitute a step towards the actual applicability of LNThs in diagnosis and clinical stages. In order to demonstrate this possibility, we had narrowed our efforts to the detection of ischemic tissues, *i.e.* tissues affected by a temporal or permanent restriction in blood supply (BROWN; WILSON, 2004). The reasons for investigating this particular problem were manifold: ischemic damages in tissues are reliable indicators of the present or past existence of cardiovascular dysfunction; their detection and imaging constitute valuable indicators of the damage produced after a cardiovascular accident etc. Nevertheless, one reason stood out: when a tissue experiences an ischemic episode, most of its biophysical parameters are affected including blood perfusion, water content, volume and metabolic activity (BECKER, 2013; BHARGAVA; CHANMUGAM; HERMAN, 2014; ELTZSCHIG; ECKLE, 2011; JENNINGS et al., 1978). Now, as we recall from Section 2.3, the thermal dynamics of a tissue is governed by Penne's bioheat equation. Hence, according to **Equation 2.15**, any biological malfunction affecting either blood perfusion, metabolic activity or chemical composition of tissues would modify their thermal dynamics and, thus, would be detectable by LNThs operating in BW-II.

### 5.2.1. Utilized NPs (PbS/CdS/ZnS QDs)

**Figure 5.8.** Depiction of the core/shell PbS/CdS/ZnS quantum dots utilized in the work described in this section.


The platform for *in vivo* detection of ischemic tissues was based on the outstanding properties of the already established PbS/CdS/ZnS QDs. Their intense and easily detectable emission was based on the synergistic action of the PbS emitting core, the large reduction of trap states resulting from the presence of a thin, epitaxial CdS shell, and the complete isolation from the outside environment provided mainly by the robust biocompatible outer shell of ZnS (**Figure 5.8**). Aside from a remarkable emission intensity, the PbS/CdS/ZnS QDs could also be tuned to possess NIR emission lying within the second biological window.

### 5.2.2. Characterization of PbS/CdS/ZnS QDs

The NIR-LNThs used in this work for ischemia detection were PbS/CdS/Zns quantum dots (NIR-QDs). These NIR-QDs showed a unique combination of properties (such as high fluorescence brightness and high thermal sensitivity at the NIR-excitation and emission, long term stability and low cytotoxicity) and because of that they have been previously used for dynamic *in vivo* imaging as well as for deep tissue *in vivo* luminescence thermometry during photothermal therapies (BENAYAS et al., 2015; DEL ROSAL et al., 2016a). Hence, the PbS/CdS/ZnS were already well described in literature. For this reason, we will just briefly state their characteristics.

**Figure 5.9. Characterization of the NIR-QDs. (a)** Emission spectrum (color coded) of a colloidal solution of NIR-QDs as a function of temperature. **(b)** Integrated emitted intensity generated from a colloidal solution of NIR-QDs as a function of

temperature. Dots are experimental data obtained from b and the solid line is the linear fit.

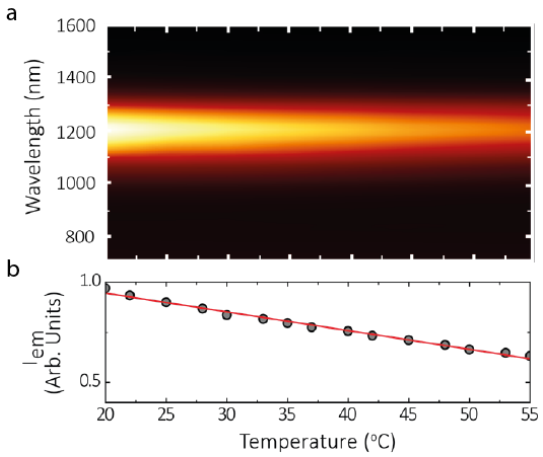


For a detailed description of the working principles of QDs as nanothermometers, see Section 2.2.3. A TEM image of the NIR-QDs used in this work is shown in **In this** section, we will describe the synthesis routes followed to produce the NPs studied throughout this thesis. The main properties (composition, surface coating, size, hydrodynamic diameter and potential zeta) of the NPs are indicated in Table 3.2. The transmission electron microscopy (TEM) images, from which the size was determined, are shown in **Erro! Autoreferência de indicador não válida.**. The synthesis and basic characterization of the physicochemical properties of the NPs was carried out by different groups (see Table 3.2), which mostly aims not at manufacturing but at studying different systems for biological applications.

***Figure 3.11*e**, from which an average diameter of 5.6 nm has been estimated (**Table 3.2**). The NIR-QDs showed outstanding colloidal stability in PBS without showing signs of precipitation over a period of one year. The Z-Potential of our NIR-QDs was found to be -27 mV, in agreement with the good observed colloidal stability. When optically excited by 808 nm laser radiation, these QDs showed a single-peak broadband emission centered at around 1200 nm whose intensity was strongly dependent with temperature, as shown in **Figure 5.9a**. Integrated intensity decreased linearly with temperature at a rate of $1\%\cdot{}^{o}C^{-1}$ (**Figure 5.9b**)

allowing for a straightforward intensity-based thermal reading with uncertainty below 1ºC. [21] Prior to conducting small animal experiments, the cytotoxicity of the NIR-QDs was evaluated. In particular, the time evolution of metabolic parameters and physical activity in individual mice after oral and intravenous administration of NIR- QDs was investigated by using fully automated cages capable of real time monitoring of metabolic, behavioral, and physiological parameters. A description of the investigation method can be found in Section 3.4.3. It was found that the side effects caused by the administration of our NIR-QDs were considered mild. Indeed, the minimum biophysical perturbation caused by our NIR-QDS is in agreement with the negligible toxicity previously found in both *in vivo* and *in vitro* studies (DEL ROSAL et al., 2016a; SACCOMANDI; SCHENA; SILVESTRI, 2013).

### 5.2.3. Animal model of artery disease

The procedure followed to evaluate the potential application of our NIR-QDs for ischemia detection is schematically represented in **Figure 5.10.** It corresponds to a murine model of hindlimb ischemia, a standard model of peripheral artery disease in humans (LIMBOURG et al., 2009). CD1 individual mice were anesthetized and subjected to a double ligation of the femoral artery in one limb that resulted in a low blood perfusion rate in the entire hindlimb tissue (**Figure 5.10a**). For a detailed description of the surgery procedure see Section 3.4.2. The efficacy of surgery in reducing the blood perfusion was checked by thermographic imaging. The success of the surgery was evidenced by a clear reduction in the limb temperature with respect to the temperature at the control limb (BROOKS et al., 2000). For practical means, a successful surgery was assumed if, 24 hours after artery ligation, the temperature difference between ischemic and control limbs ($\Delta T_I = T_C - T_S$, where $T_S$ and $T_C$ are the temperature at the ischemic and control limb, respectively) was larger than 1 °C (i.e. if $\Delta T_I > 1$ °C). **Figure 5.10b** shows, as an example, the thermal image of an individual mouse 24 hours after a successful surgery, denoted by a relative temperature

reduction in the left limb close to 2 °C. The mice that presented $\Delta T_I$ below 1 °C were discarded for this study as such low temperature differences were considered an indication of a minimum change in blood perfusion rate. On the other hand, in the successful cases, 50 µL of a 0.01 mg/mL solution of NIR-QDs in PBS were subcutaneously injected into both limbs over the surae triceps muscle (see **Figure 5.10c**). Injection was performed 24 hours after surgery. **Figure 5.10d** shows a NIR luminescence image ($\lambda_{exc}$ = 808 nm, $\lambda_{em}$ = 1200 nm) obtained from a characteristic individual after injection of the NIR-QDs, revealing their location in both limbs.

**Figure 5.10. Schematic representation of the experimental procedure followed for animal experiments in this work. (a)** Artery ligation. **(b)** Thermal image of an individual 24 hours after artery ligation in which the lower temperature in the ischemic leg is evidenced. **(c)** Injection of NIR-QDs. **(d)** Near infrared luminescence image of a characteristic individual as obtained just after the injection of the NIR-QDs. **(e)** Soft heating. **(f)** Measurement of the thermal transient. **(g)** Schematic representation of the working principle of Transient Thermometry.

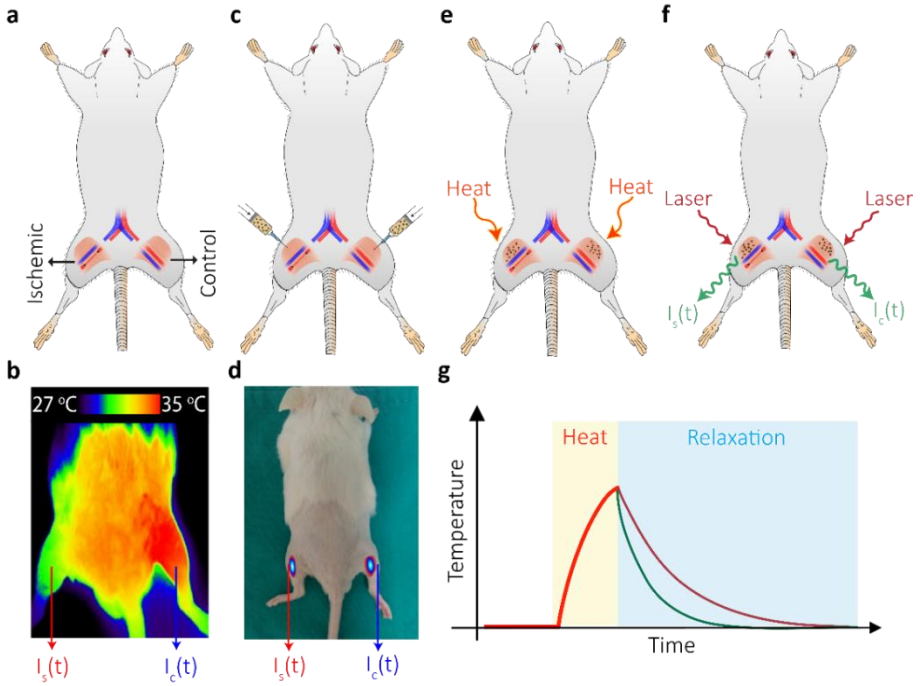


The procedure for measurement of thermal relaxation profiles of both ischemic and healthy limbs is represented in **Figure 5.10e** and **f**. The limb's

temperature was increased from its basal value by 8-10 °C by applying a 3 min long heat pulse provided by an 808 nm laser (*heating beam*) with a power density of 0.7 W/cm$^2$. This radiation energy was weakly absorbed by the limb tissues and delivered as heat. During and after the application of the heating pulse, both limbs were illuminated by a second 808 nm laser beam (*probing beam*) with a much-reduced power density (0.05 W/cm$^2$), so that sufficient fluorescence from the NIR-QDs was obtained without additional heating. Then, the time evolution of the emitted intensity generated by NIR-QDs inside both limbs was recorded and translated into temperature units by using the calibration curve included in **Figure 5.9b**. This entire procedure allowed us to explore the possible modification of tissue relaxation dynamics due to ischemia (see schematic representation of **Figure 5.10g**).

### 5.2.4. Determination of ischemic and inflammatory phases by PbS/CdS/ZnS QDs

Once the thermal relaxation profiles of both limbs were registered, mice were sacrificed 72 hours after surgery in order to measure the relative modification of the distal area of the *surae* triceps muscles ($\Delta S^R_m$):

$$\Delta S_m^R = \frac{S_s - S_c}{S_C}$$

**Equation 5.5**

where $S_S$ and $S_C$ were the cross-sectional areas (mm$^2$) of ischemic and control (healthy) limbs, respectively. These areas were calculated by dividing the muscle mass (mg) by the muscle optimal length (mm) and by the density of mammalian skeletal muscle (1.06 mg/mm$^3$). Evaluating $\Delta S^R_m$ can, in principle, give a better understanding of the effects induced after artery ligation, in particular when elucidates which of the processes was dominant: ischemia or inflammation.

Artery ligation leads to the appearance of ischemic muscular injury due to a relevant reduction in metabolic activity, supply of nutrients and oxygen (AOI et al., 2009; CHARGÉ; RUDNICKI, 2004; RUSCHKEWITZ; GEFEN, 2010). As a result,

ischemic muscles suffer from an initial phase of degeneration, atrophy and necrosis that results in a reduction in muscle size (*i.e.* ischemia phase $\Rightarrow \Delta S^{R}_{m} < 0$). This degenerative phase, in turns, is followed by a regenerative one in which the muscle undergoes a repairing process implying in overlapping inflammation, edema, angiogenesis and revascularization (CHARGÉ; RUDNICKI, 2004). In particular, the generated inflammatory mediators during the regenerative phase result in an increase of metabolic processes and, thus, in an increased muscle size (i.e. inflammation phase $\Rightarrow \Delta S^{R}_{m} > 0$) (CARDEN; GRANGER, 2000; RUSCHKEWITZ; GEFEN, 2010). A high variability in both phases between mice due to genetic and microvascular morphology differences was already reported in literature (LIMBOURG et al., 2009). In our experiments, the predominant effect 72 hours after surgery was found to be a degenerative phase evidenced by atrophy: 77% of individuals investigated in this work displayed $\Delta S^{R}_{m} < 0$.

**Figure 5.11a** shows the thermal relaxation profiles from an individual mouse as obtained 48 hours after surgery. This individual presented a reduction in the distal area of muscle as large as $\Delta S^{R}_{m}$ = -20 %, thus being in an ischemic phase. The thermal relaxation profiles of both healthy and ischemic limbs were fitted, in a first order approximation, to a single exponential decay of the form:

$$\Delta T(t) = \Delta T_0 \cdot exp[-t/\tau_{eff}\,]$$

**Equation 5.6**

where $\Delta T$ was the tissue temperature increment with respect to the basal temperature, $\Delta T_o$ was the tissue temperature increment achieved at the end of the heating pulse, $t$ was the time elapsed after the end of the heating pulse, and $\tau_{eff}$ was defined as the effective relaxation time of the tissue. At this point it is important to mention that, strictly speaking, fitting thermal relaxation profiles of tissues to single exponentials, does not correspond to a complete solution of **Equation 2.15** for this particular problem. Nevertheless, this approach is supported by experimental data. For a detailed discussion see Section 2.3.2.3, where a reasonable practice, that allows a straightforward description of

complex phenomena in terms of a single parameter (the effective relaxation time), is presented. Thus, fitting the experimental data of **Figure 5.11b** to **Equation 5.6** lead to thermal relaxation times of $\tau^{c}_{eff}$ =(196 ± 5) s and $\tau^{S}_{eff}$ = (113 ± 5) s for healthy and ischemic legs, respectively. Consequently, artery ligation has produced a relative reduction in the characteristic thermal relaxation time ($\Delta\tau^{R}_{eff}$ =($\tau^{c}_{eff}$ -$\tau^{c}_{eff}$)/$\tau^{c}_{eff}$)) as large as $\Delta\tau^{R}_{eff}$ = -30%. The magnitude of $\Delta\tau^{R}_{eff}$ was systematically examined for a total amount of 12 mice. The statistical results are summarized in **Figure 5.11c** which includes the ($\Delta\tau^{R}_{eff}$, $\Delta S^{R}_{m}$) coordinates obtained for each individual. As it can be observed, all individuals in the ischemic phase (negative values of $\Delta S^{R}_{m}$) also showed negative values of $\Delta\tau^{R}_{eff}$. At the same time, those individuals in the inflammatory phase (positive values of $\Delta S^{R}_{m}$) showed positive values for $\Delta\tau^{R}_{eff}$. Thus, **Figure 5.11** revealed $\Delta\tau^{R}_{eff}$ as an unequivocal indicator of the tissues response against transient occlusion of blood flow. When the response was dominated by the initial degenerative phase with muscle atrophy, $\Delta\tau^{R}_{eff}$ was reduced. On the other hand, when the dominant role of an inflammatory reaction was evidenced, $\Delta\tau^{R}_{eff}$ increased. This fact was in good agreement with previous numerical simulations related to the thermal recovery of injured and healthy tissues (BHARGAVA; CHANMUGAM; HERMAN, 2014; DIAO; ZHU; WANG, 2003).

**Figure 5.11. Dependence of thermal relaxation profiles on blood perfusion and its consequences. (a)** Characteristic time evolution of the luminescence intensity generated by injected NIR-QDs during the procedure followed for Transient Thermometry. Note that the initial intensity is fully recovered at the end of the measurement cycle. **(b)** Representative thermal transients obtained from ischemic and healthy legs. The faster thermal dynamics of the ischemic leg is evidenced. **(c)** Statistical results of $\Delta\tau^{R}_{eff}$ vs. $S^{R}_{m}$, taken over 12 mice.

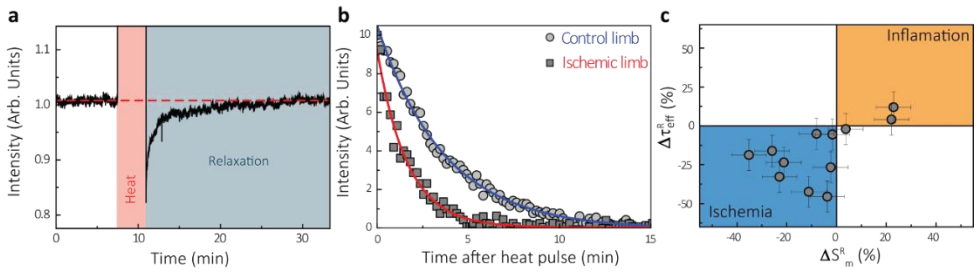

At this point, we still needed to address the following question: why does the ischemic tissue undergo faster thermal relaxations? In order to answer it, we based our discussion on a model of heat conduction in a composite material subjected to perfusion (see Section 2.3.2.3) from which we could express the following relation:

$$\tau_{eff} = L^2/(4\alpha_{tissue}^{eff})$$

**Equation 5.7**

where $L_R$ was a characteristic length common to both ischemic and healthy states and $\alpha^{eff}_{tissue}$ was the so-called effective thermal diffusivity of the tissue (M. et al., 2011).

Thus, since $L_R$ was defined as a constant (see **Appendices 2**), data included in **Figure 5.11** suggested an increment in $\alpha^{eff}_{tissue}$. The literature clearly identified two distinct effects during the ischemic phase: reduction in blood perfusion rate and in tissue dimensions. These two effects, however, were expected to have different impact on the effective thermal diffusivity. On one side, numerous works described how the thermal diffusivity of tissues and organs is reduced if the blood perfusion rate decreases (PATEL et al., 1987). On the other, any reduction in water content causes mass loss and a reduction in the tissue dimensions, which results in an increment in the tissue thermal diffusivity (CHASTAGNER et al., 2016; COOPER; TREZEK, 1971). In few words, the experimentally observed increment in the effective tissue thermal diffusivity could not be attributed to the reduction in blood perfusion *per se* (as this would actually cause the opposite effect). Consequently, the increment in thermal diffusivity must had to be caused by a dominant reduction in water content and the resulting tissue injury (ZACCAGNINI et al., 2015).

### 5.2.5. Monitoring of ischemic damage recovery by PbS/CdS/ZnS QDs

In order to get a further understanding on the tissue modifications induced after artery ligation, long-term studies were also conducted using PbS/CdS/ZnS

QDs. In this case the procedure was the same as the one schematically included in **Figure 5.10** with the difference that the individuals were not sacrificed after 72 hours but, instead, 30 days after surgery. Relaxation profiles, NIR luminescence and thermographic images were systematically obtained every 2 days. Representative results of these long-term studies are included in **Figure 5.12**. **Figure 5.12a** and **b** show the NIR luminescence images ($\lambda_{exc}$ = 808 nm, $\lambda_{em}$ = 1200 nm) of a representative individual as obtained 3 and 13 days after surgery, respectively. In **Figure 5.12a** the luminescence generated by the NIR-QDs (injected 2 days after surgery) is clearly observed. Both limbs presented similar emission intensities as expected since both were inoculated with the same amount of QDs. The luminescence image obtained 13 days after surgery (**Figure 5.12b**), however, demonstrated a drastic reduction in the luminescence intensity generated from the control limb in respect to the ischemic one. This fact evidences a more effective retention of the PbS/CdS/ZnS QDs at the ischemic limb. This QDs retention is even more evident in **Figure 5.12c** which includes the time evolution of the fluorescence intensities generated at both ischemic and control limbs. The enhanced retention of QDs at the ischemic limb can be explained in terms of two different phenomena. Firstly, the ischemic leg had a reduced blood perfusion so that removal of NIR-QDs from the ischemic limb via the bloodstream was less efficient. Secondly, there was a preferential and long-term accumulation of nanoparticles in ischemic tissues due to the enhanced permeability and retention effect (DVIR et al., 2011; ENGLAND et al., 2016; KIM et al., 2011; LUNDY et al., 2016; MATSUMURA; MAEDA, 1986). **Figure 5.12c** shows a fast clearance of PbS/CdS/ZnS QDs during the first 13 days (in both healthy and ischemic limbs) whereas for longer times the emitted intensities seemed to stabilize, thus suggesting a weak clearance of QDs. At this point we state that during the first 13 days, revascularization within the ischemic leg was produced, being responsible for the intensity decay. Nevertheless, during this period, blood flow was larger in the healthy leg, which explains why the intensity decays much faster than in the ischemic leg. At longer times, we state that both

ischemic and control limbs had the same blood perfusion activity, so that the larger retention of QDs in the ischemic limb found for such times can be fully attributed to the enhanced permeability and retention effect.

**Figure 5.12d** shows the time evolution of the temperature difference between ischemic and control limbs (previously defined as $\Delta T_I$). As it can be observed, this difference decreased rapidly during the first 13 days and for longer times its value became stable. Since this temperature difference was strongly related to the blood perfusion level, these data also supported the existence of an efficient revascularization process in the ischemic leg during the first 13 days after surgery. These results are in agreement with those observed by Zaccagnini et al using magnetic resonance imaging (ZACCAGNINI et al., 2015).

**Figure 5.12. (a)** Time evolution of ischemic injury as detected by TTh. Near infrared luminescence images of a representative individual as obtained 3 and 13 days after artery ligation (**(a)** and **(b)**, respectively). **(c)** Time evolution of luminescence intensity generated by NIR-QDs injected in an ischemic and healthy limb. **(d)** Temperature difference between ischemic and healthy limbs as a function of the time elapsed after artery ligation. e, Relative reduction in the characteristic thermal relaxation time ($\Delta\tau^R_{eff}$) as a function of the time elapsed after artery ligation. In **(c)**, **(d)** and **(e)** dots are experimental data and lines are guides for the eyes. The error bars correspond to the standard deviations.

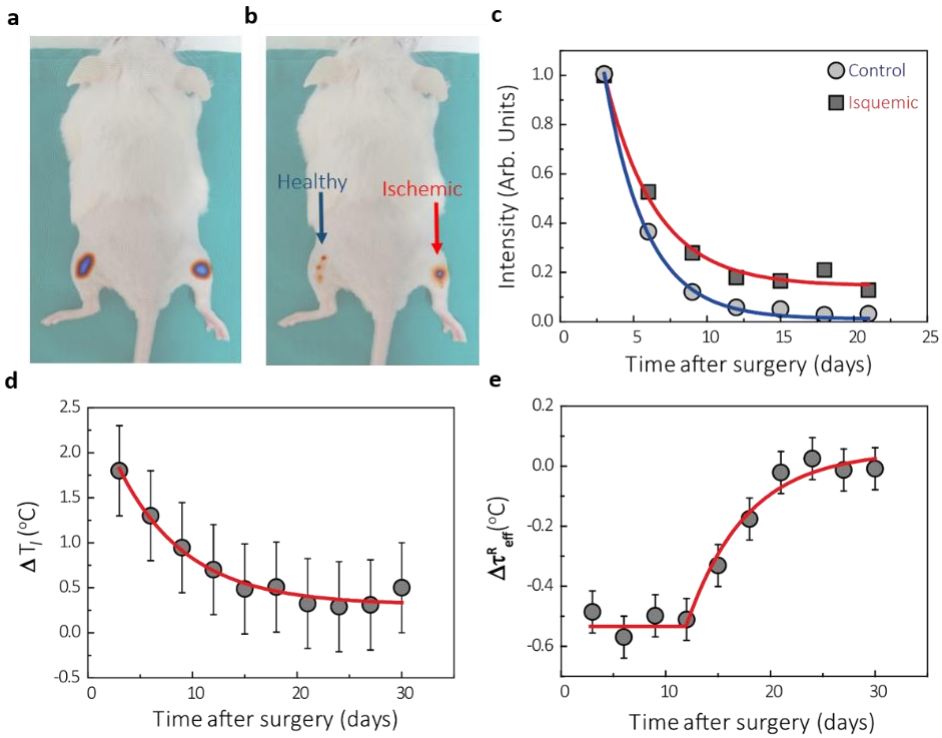


Finally, **Figure 5.12e** shows the time evolution of the $\Delta\tau^{R}_{eff}$ parameter. In accordance with data included in **Figure 5.11**, at short times after surgery, the ischemic limb shows a relaxation time substantially smaller than that of the control limb (3 days after surgery $\Delta\tau^{R}_{eff}$ = -60 %). During the first 10-15 days after surgery, $\Delta\tau^{R}_{eff}$ remained virtually constant despite the fact that revascularization was already taking place in the ischemic limb. For longer times (>15 days) the ischemic limb started to approach the same relaxation time of the healthy limb. We state that, during this period, a significant re-establishment of perfusion lead to a recovery of water content and metabolic activity in the ischemic tissues. This recovery, in turns, lead to the gradual increase of $\Delta\tau^{R}_{eff}$ from the value induced after surgery (-60%) until zero which corresponds to a situation in which the ischemic tissues had recovered their initial properties.

Thus, in summary, this work clearly demonstrated how LNThs can not only be used to access the basic properties of living tissues but also to detect and monitor the time evolution of an incipient disease.

## 5.3. Core/shell NPs for the acquisition of 2D subcutaneous *in vivo* thermal imaging

Up to now, the discussion of this chapter has been directed to demonstrate the use of LNThs as diagnosis probes in order to determine the health status of living tissues. At this point it should be noted that the utilized LNThs only performed subcutaneous dynamical thermal reading in one spatial dimension (a point). However, for an accurate achievement of thermal-based diagnosis one would need, at least, the dynamical acquisition of 2D subcutaneous thermal images as this would provide more information on heat transfers taking place in biological systems. Going from 1D to 2D, in turns, is not an easy task. In fact, other well-established methods have failed in undergoing this transition. For instance, thermographic cameras were capable of accurate contactless 2D *in vivo* dynamic thermal imaging but only at the surface of the tissues (skin) with negligible penetration capability (GODOY et al., 2015; HERMAN, 2013). Prior to the development of this thesis, the elaboration of a direct procedure for two-dimensional subcutaneous dynamic thermal imaging (2D-SDTI) was still left to be done.

For the reasons described in the beginning of this chapter, the eventual ambition of achieving *in vivo* 2D-SDTI by means of LNThs would benefit from the concurrent use of all three available BWs, *i.e.*, exciting the NPs in the BW-I and collecting their emission in BW-II and/or BW-III (HEMMER et al., 2016; SKRIPKA et al., 2017; SORDILLO et al., 2014). Prior to the development of the work in this section, a great effort was given to the production of rare-earth-based luminescent thermometers emitting in the BW-II while being excited by a wavelength within BW-I. On the other hand, only one example of a LNTh emitting in the BW-II and BW-III while being excited in the BW-I could be found (SKRIPKA et al., 2017). However, in every case, the LNThs did not satisfy a fundamental requirement for the achievement of 2D-SDTI: a relatively high thermal sensitivity (not larger than $1x10^{-2}\ ^{o}C^{-1}$). These low thermal sensitivities made it

very difficult for the commercially available shortwave infrared cameras to acquire low-noise fluorescence images and, therefore, to reconstruct accurate two-dimensional thermal images (BRITES et al., 2012). That was exactly the problem faced in this section: to provide a highly sensitive LNTh emitting in BW-II and BW-III while being excited in BW-I.

### 5.3.1. Proposed NPs (Er-Yb@Yb-Tm $LaF_3$ NPs)

The NPs were based on a core/shell structure consisting of an $Er^{3+}$, $Yb^{3+}$ co-doped $LaF_3$ core and a $Tm^{3+}$, $Yb^{3+}$ $LaF_3$ co-doped shell. The spatial separation between $Tm^{3+}$ and $Er^{3+}$ was meant to avoid deleterious luminescence quenching via ET or back-ET whereas ion-ion interaction at the core/shell interface allows for full optical operation of the structure under single 690 nm laser excitation. The $Tm^{3+}$, $Yb^{3+}$ and $Er^{3+}$ concentrations were, after many tests, respectively fixed to 10, 10 and 2 mol. %. The spatial separation between ions was achieved by selective doping during the synthesis procedure (see Section 3.9.2.3), resulting in NPs such as those schematically drawn in inset of **Figure 5.13**.

Under this configuration, the shell acts as a donor unit absorbing the 690 nm radiation through $^2H_6 \rightarrow {}^3F^3$ $Tm^{3+}$ absorption (see **Figure 5.13**). Then, non-radiative ET between $Tm^{3+}$ and $Yb^{3+}$ ions both inside the shell and at the core/shell interface results in the $^2F_{7/2} \rightarrow {}^2F_{5/2}$ excitation of $Yb^{3+}$ ions inside the core. Finally, ET between $Yb^{3+}$ and $Er^{3+}$ ions allocated at the core leads to the excitation of erbium ions up to their $^4I_{11/2}$ state. The energy transfer (ET) processes taking place after 690nm optical excitation are also summarized in **Figure 5.13**. The radiative emissions of $Er^{3+}$ (1550 nm, BW-III), $Yb^{3+}$ (1000 nm, BW-II) and $Tm^{3+}$ (1230 nm, BW-II) are represented by full lines.

**Figure 5.13.** Simplified energy scheme of the $Tm^{3+}$, $Yb^{3+}$ and $Er^{3+}$ emitting centers representing excitation and radiative decays (full lines), nonradiative decays (curved line), and possible cross-relaxations and ion–ion energy transfer paths (dashed lines). Upon 690 nm excitation, they present the emission bands ascribed to $Tm^{3+}$ (1230 and 1470 nm), $Yb^{3+}$ (1000 nm) and $Er^{3+}$ (1550 nm).The inset shows the schematic representation of the Er-Yb@Yb-Tm $LaF_3$ NPs.

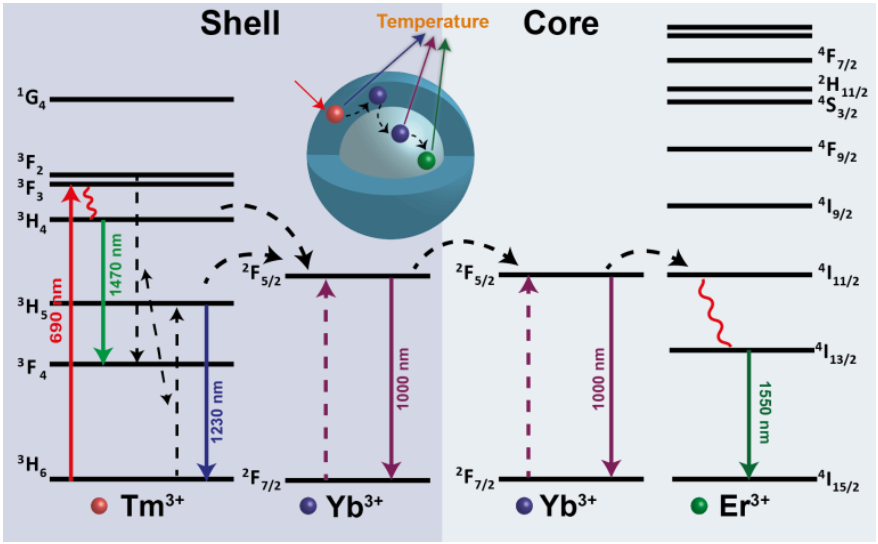


### 5.3.2. Characterization of Er-Yb@Yb-Tm $LaF_3$ NPs

For the sake of comparison, we have systematically investigated the spectroscopic and thermal sensing properties of two different samples. The first sample corresponded to the already mentioned Er-Yb@Yb-Tm NPs and will be graphically represented by a gray core sphere surrounded by a blue shell (just as the one depicted in **Figure 5.13**). The second sample was a single core $LaF_3$ NP triply doped with $Tm^{3+}$, $Yb^{3+}$ and $Er^{3+}$ ions (hereafter Er-Yb-Tm $LaF_3$ NPs) – with the same molar concentrations as in the first sample - and will be represented by a green sphere. It can be noted that $Tm^{3+}$ ions are only spatially separated from the Er-Yb ions in the core/shell NPs. Section 3.9 includes both the characteristic transmission electron microscopy (TEM) images of Er-Yb@Yb-Tm and Er-Yb-Tm $LaF_3$ NPs and their corresponding diameters. The core/shell nature of the Er-Yb@Yb-Tm $LaF_3$ NPs may be inferred, as discussed later, by the observed spectroscopic differences and guaranteed by measurements of both energy-dispersive X-ray (EDX) and electron paramagnetic resonance (EPR) performed on NPs produced with similar synthesis routes (as in Sections 4.1.2 and 4.2.2).

**Figure 5.14.** Room temperature emission spectra of Er-Yb-Tm $LaF_3$ NPs under 690 nm excitation (green) and of Er-Yb@Yb-Nd LaF3 NPs under 690 (yellow) and 808 nm (blue) laser excitations.

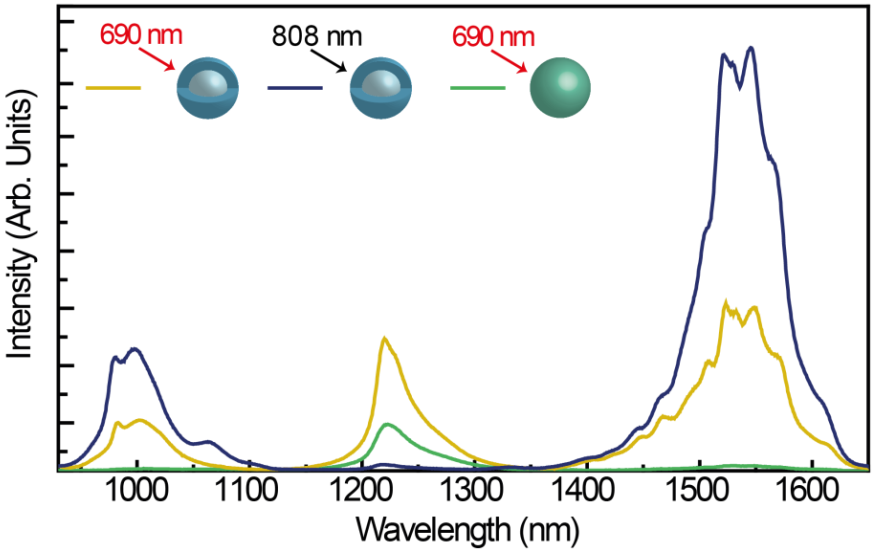


The room temperature emission spectra generated from the single-core NPs under infrared 690 nm laser excitation and from the core/shell NPs under infrared 690 and 808 nm laser excitations are included in **Figure 5.14** as green, yellow and blue curves, respectively. The characteristic bands of $Yb^{3+}$, $Tm^{3+}$ and $Er^{3+}$- centered at 1000, 1230 and 1550 nm, respectively, were only clearly observed for the Er-Yb@Yb-Tm $LaF_3$ NPs under 690 nm laser excitation. On the other hand, the characteristic bands of $Yb^{3+}$ and $Er^{3+}$were barely detected for Er-Yb-Tm $LaF_3$ NPs under the same conditions, with the only remarkable emission being centered at 1230 nm. This fact demonstrated that the core/shell engineering was essential to produce efficient luminescence in both BW-II and BW-III. Core/shell structure lead to a spatial separation between $Er^{3+}$ and $Tm^{3+}$ ions in such a way that $Er^{3+} \rightarrow Tm^{3+}$ back ET, involving $^4I_{13/2}(Er^{3+})$ and $^3F_4(Tm^{3+})$ energy levels, was avoided or reduced. This back ET was minimized in the core/shell structure where Erbium and Thulium ions were spatially separated, being this denoted by an enlargement in the fluorescence lifetime of the $^4I_{13/2}$ level of $Er^{3+}$ ions. The ability of core/shell engineering for tailoring the fluorescence properties of rare-earth based nanostructures is not restricted to the case here discussed as it has been already previously demonstrated in other cases. For instance, core/shell engineering has been found to be essential to shift

excitation wavelength of upconverting nanoparticles from 980 down to 808 nm and for fine tuning of luminescent properties via selective energy migration (AI et al., 2015; LI et al., 2013; WANG et al., 2011). In order to elucidate the role played by the excitation wavelength, the emission spectrum generated by the Er-Yb@Yb-Tm $LaF_3$ NPs under 808 nm laser excitation was also included in **Figure 5.14**. As it can be observed, even though the core/shell system presents a higher brightness under 808 nm excitation, the characteristic band emission of $Tm^{3+}$ at 1230 nm is now barely detected. This can be explained in terms of the energy level schemes included in **Figure 5.13**. We state that the $^3H_5$ ($Tm^{3+}$) level responsible for the 1230 nm emission band is mainly populated through the $^3F_3;^3H_6 \rightarrow ^3F_4;^3H_5$ cross-relaxation (see dashed arrows in **Figure 5.13**). Under 808 nm excitation the $^3F_3$($Tm^{3+}$) level is not populated so that this cross-relaxation process does not take place and, consequently, the $^3H_5$($Tm^{3+}$) level is only populated due to deexcitation from the $^3H_4$. As it will be demonstrated later, accurate ratiometric thermal sensing requires similar contribution of the three bands to the overall emission spectrum. Thus, optimum performance of Er-Yb@Yb-Tm $LaF_3$ NPs as LNThs requires optical excitation at 690 nm, *i.e.*, within the BW-I spectral range.

### 5.3.3. Thermal sensing capability of Er-Yb@Yb-Tm

The ability of our Er-Yb@Yb-Tm $LaF_3$ NPs for luminescence thermometry in BW-II and BW-III was investigated by analyzing their emission spectra under 690 nm excitation in the physiological temperature range. The results are summarized in **Figure 5.15**, in which emission spectra of Er-Yb@Yb-Tm and Er-Yb-Tm $LaF_3$ NPs (as obtained at 20 and 50°C), under 690 nm excitation, are displayed (**Figure 5.15a** and **b**, respectively). Whereas was a clear reduction in the relative contributions of thulium and erbium ions to the overall emission spectrum was observed for the core/shell NPs, the relative contributions of the different ions to the emission spectrum of simple NPs barely changed with temperature. As a result, the observed variations in the core/shell structure suggested the use of three ratiometric approaches for temperature sensing. They

could be achieved by evaluating the following ratios: i) between the emitted intensity of $Yb^{3+}$ ions at 1000nm ($^2F_{7/2} \rightarrow {}^2F_{5/2}$, hereafter $I_{Yb}$) and that of $Tm^{3+}$ ions at around 1230 nm ($^3H_5 \rightarrow {}^3H_6$, hereafter $I_{Tm}$); ii) between the emitted intensity of $Yb^{3+}$ ions ($I_{Yb}$) at 1000 nm and that of $Er^{3+}$ ions at 1550 nm ($^4I_{13/2} \rightarrow {}^4I_{15/2}$, hereafter $I_{Er}$); and iii) between $I_{Tm}$ and $I_{Er}$. It was graphically clear from **Figure 5.15c** that $R_1 = I_{Yb}/I_{Tm}$ and $R_2 = I_{Yb}/I_{Er}$ were far superior to $R_3 = I_{Tm}/I_{Er}$ in terms of temperature sensing and that the simple nanostructure did not provide a meaningful temperature sensitivity. From experimental data included in **Figure 5.15c** the relative thermal sensitivities achieved with each of the intensity ratios were calculated (see Section 2.2.4.1). The results are included in **Figure 5.15d** and can be summarized as follows: at 20 $^oC$ the Er-Yb-Tm $LaF_3$ NPs presented relative thermal sensitivities of $1.3\times10^{-2}$ and 0.7×10-2 $^oC^{-1}$ when using $R_1$ and $R_2$ as the temperature-sensitive parameter, respectively. On the other hand, the Er-Yb@Yb-Tm $LaF_3$ NPs presented remarkably higher values for the relative thermal sensitivities of $R_1$ and $R_2$: $3.9\times10^{-2}$ and $5.0\times10^{-2}$ $^oC^{-1}$, respectively, allowing temperature resolutions of 0.3 $^oC$ under the same conditions. Note that core/shell engineering has allowed for a four-fold improvement in the thermal sensitivity of Er/Yb/Tm triply doped $LaF_3$ NPs.

**Figure 5.15.** Emission spectra of **(a)** Er-Yb@Yb-Tm $LaF_3$ and **(b)** Er-Yb-Tm $LaF_3$ NPs obtained at 20 and 50 °C under 690 nm excitation. **(c)** Calibration curves of Er-Yb@Yb-Tm $LaF_3$ (blue circles and squares) and Er-Yb-Tm $LaF_3$ (green triangles and inverted triangles) NPs. $R_1$stands for the ratio between the emitted intensity of $Yb^{3+}$ ions at 1000nm and of $Tm^{3+}$ ions at around 1230 nm, while $R_2$ stands for the ratio between the emitted intensity of $Yb^{3+}$ ions at 1000nm and of $Er^{3+}$ ions at 1550 nm. Dots are experimental values, and the dashed lines represent the best linear fits to the experimental data. **(d)** Relative thermal sensitivities as a function of the temperature for the Er-Yb@Yb-Tm $LaF_3$ and Er-Yb-Tm $LaF_3$ NPs. The symbols are as described in (c).

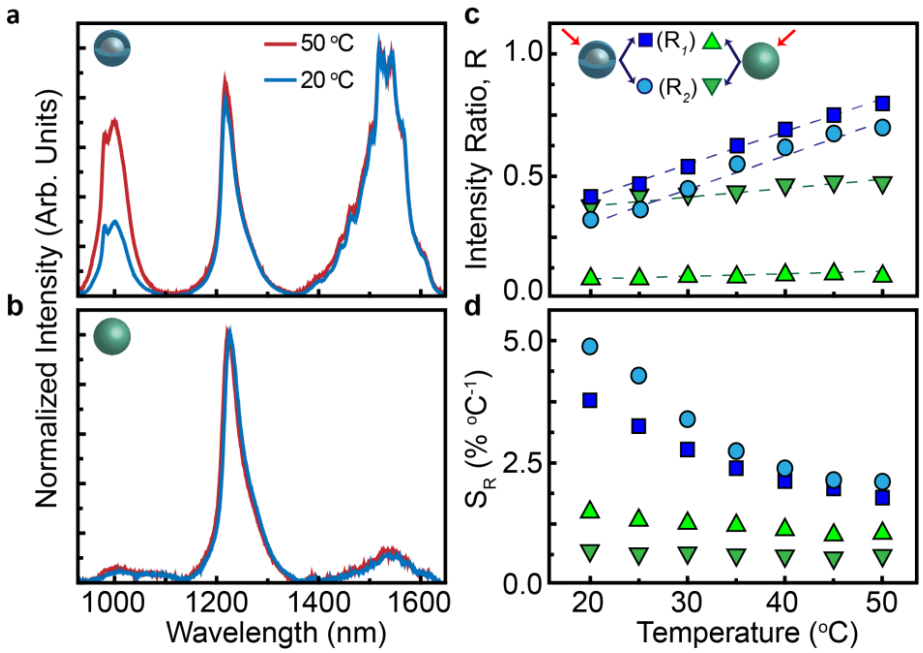


In order to give a comprehensive comparison of the thermal sensitivity provided by Er-Yb@Yb-Tm core/shell NPs with respect to other LNThs, its value was compared with those reported for other nanostructures operating in the BW-II and/or BW-III and that were proposed up until the development of this thesis. Reminding **Figure 1.3** , one can observe that the NPs presented in this section were, to the best of our knowledge, the most sensitive LNThs operating in BW-II and/or BW-III. Even though the thermal sensitivity of the OA-$NaYF_4$:$Yb^{3+}$, $Ho^{3+}$, $Er^{3+}$ NPs was comparable to the ones reported in this work, they presented the disadvantage of using an excitation wavelength (980 nm) that was partially absorbed by the water within tissues, reducing penetration depth and causing non-negligible pump induced thermal effects during *in vivo* experiments (KAMIMURA et al., 2017; MAESTRO et al., 2013a).

### 5.3.4. Acquisition of in vivo 2D-SDTI by means of Er-Yb@Yb-Tm $LaF_3$ NPs

Once the superior thermal sensitivity of Er-Yb@Yb-Tm $LaF_3$ NPs in both BW-II and BW-III was demonstrated, their potential use for 2D-SDTI was then

evaluated. As mentioned in the introduction, such subcutaneous thermal videos would allow for the acquisition of two dimensional patterns of tissue thermal properties that, in turns, could be used to identify and localize damaged tissues. Moreover, *in vivo* 2D-SDTI would also make possible the quantification of the thermal dose administrated in the whole area of injection in a hyperthermia treatment. The achievement of *in vivo* 2D-SDTI by means of Er-Yb@Yb-Tm $LaF_3$ NPs was demonstrated with the simple experiment schematically described in **Figure 5.16**. A total volume of 200 μL of a PBS dispersion of Er-Yb@Yb-Tm $LaF_3$ NPs (1% in mass) was subcutaneously injected in a CD1 mouse. The injected mouse was anesthetized and placed in a small animal imaging chamber equipped with a body temperature controller so that the basal mouse temperature was kept constantly close to 33 °C. Once thermal stabilization was achieved and the subcutaneous presence of the Er-Yb@Yb-Tm $LaF_3$ NPs was confirmed by simple fluorescence imaging experiments, we proceeded to induce a moderate temperature increment at the injection site via laser irradiation. Two different experimental arrangements were used in order to study the heating and cooling dynamics of the tissue (see **Figure 5.16a** and **b**):

- In order to perform 2D-SDTI during a heating cycle, the mouse was illuminated with a 690 nm laser (0.32 W $cm^{-2}$ of power density). This laser played a double role: it warmed up the tissue while, simultaneously, excited the infrared luminescence of the Er-Yb@Yb-Tm $LaF_3$ NPs from which time resolved thermal videos were built up.

- For the 2D-SDTI during a tissue cooling, the mouse was simultaneously illuminated with two laser sources. An 808 laser (0.7 W $cm^{-2}$) was used to warm up the tissue and a 690 nm laser (0.1 W $cm^{-2}$) was used for optical excitation. The latter was kept at a power density low enough to avoid extra heating and yet high enough to make the fluorescence of the Er-Yb@Yb-Tm $LaF_3$ NPs observable. In this second approach, during the heating cycle, the $Tm^{3+}$ ions absorbed 808 nm light which resulted in a saturation of fluorescence. Thus, in this case, dynamical

thermal imaging was only possible during cooling, i.e. after the 808 nm laser was switched off (**Figure 5.16b**).

**Figure 5.16.** (a) Subcutaneous injection of Er-Yb@Yb-Tm $LaF_3$ NPs in a CD1 mouse. (b) Temperature profiles as (b) heating and (c) cooling take place. (d) Schematic representation of the in vivo SDTI experiment. Fluorescence images of injection in the CD1 mouse as obtained by means of band-pass filters immediately after the start of the (e) heating and (f) cooling process. The dashed-lined drawings represent half the body of the CD1 mouse and it serves as an indication to the place of injection.

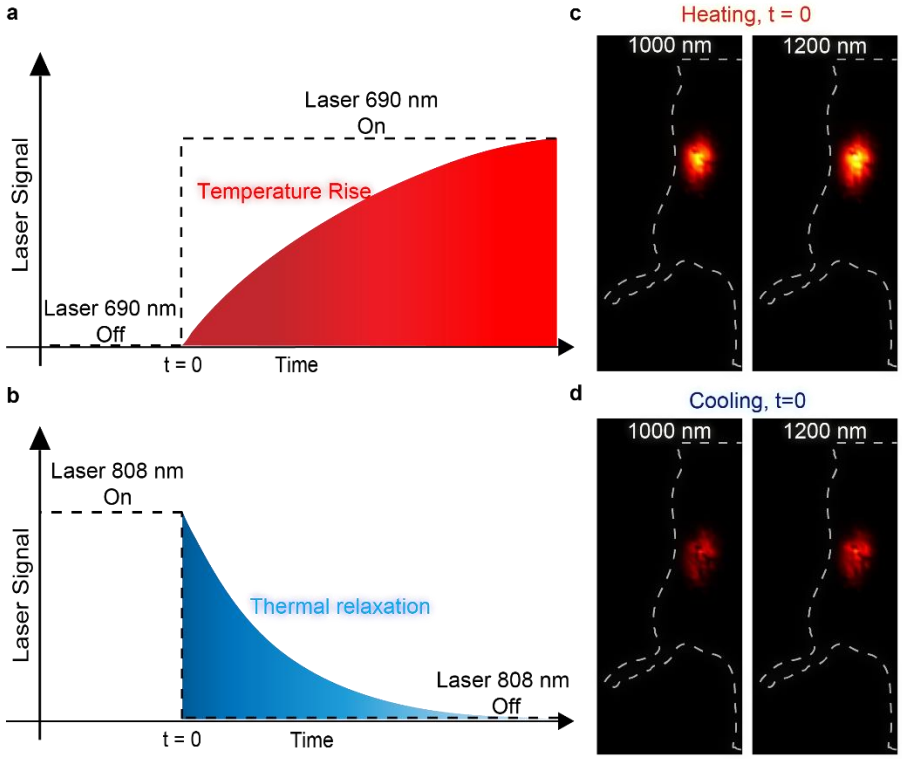


For the 2D-SDTI *in vivo* measurements the setup described in Section 3.2.1 was employed. For the quasi-simultaneous acquisition of fluorescence images at 1000 and 1200 nm, two bandpass filters were placed in a motorized wheel with a switching frequency of 0.3 Hz. The ratio between the emitted intensities at 1000 and 1200 nm was calculated pixel by pixel according to the algorithm described in Section 3.5.2. The resulting ratiometric fluorescence image was then

converted into temperature units by using a calibration curve obtained with an *ex vivo* tissue.

Figure **Figure 5.16e** and **f** contain the fluorescence images obtained at 1000 and 1200 nm at t = 0, *i.e.* immediately before starting the heating and thermal relaxation processes, respectively. From these fluorescence images it was clear that the heating procedure led to a remarkable decrease in the contrast of fluorescence images obtained at both 1000 and 1200 nm – which is in good agreement with **Figure 5.15c**. The temperature patterns obtained after processing these images were both included in **Figure 5.17** (labeled as t = 0 s). The thermal image obtained just before starting the heating procedure provided an average subcutaneous temperature close to 33 $^{o}$C which, in turns, was in very good agreement with the mouse's basal temperature. Correspondingly, the thermal image obtained immediately after the heating procedure with the 808 nm laser (*i.e.* at the beginning of the relaxation procedure) gave an average subcutaneous temperature close to 42 $^{o}$C. After the experiments, the fluorescence signal intensities at 1000 and 1200 nm recovered their original values, indicating no relevant spreading of the injected NPs.

The fluorescence images at 1000 and 1200 nm obtained at different time delays in respect to the initialization of both heating and relaxing procedures were then used to build up the corresponding thermal videos during both procedures. The MPG files of the subcutaneous thermal videos can be found in Wiley's storage of the corresponding article (XIMENDES et al., 2017b). These thermal videos were the first *in vivo* subcutaneous thermal videos reported so far. From them we have extracted thermal images at different time delays after the beginning of heating and cooling procedures. These subcutaneous thermal images are shown in **Figure 5.17** and are superimposed to an optical picture of the studied mouse. Data included in **Figure 5.17** revealed the capacity of Er-Yb@Yb-Tm $LaF_3$ NPs in combination with the home-made imaging system to provide accurate two-dimensional images of the subcutaneous spatial distribution of temperature with a time resolution better than 1 s. When looking

into literature, it was possible to find only one work reporting on an *in vivo* thermal video based on luminescence thermometry. T. Miyagawa and co-workers managed to record a thermal video of a living insect (*Dicronorrhinaderbyana*) during muscular warming (MIYAGAWA et al., 2016). In doing so, they used a luminescent thermosensitive film that was attached to the imaged muscle. The operation range of the thermosensitive film, as well as the requirement of being stacked at skin, resulted in a "superficial" thermal video. In our case we, again, recall that we are dealing with a *subcutaneous* thermal video that, as said before, would open up the possibility of intrabody thermal diagnosis and control procedures. Finally, we should note that thermal images here acquired were constructed based on a ratiometric approach so that they were not affected by undesired overall intensity fluctuations due to different concentration of NPs and/or to instabilities in the laser excitation intensity (as would be the case for QDs).

From the subcutaneous thermal videos, the time evolution of the subcutaneous temperature during both heating and cooling procedures was computed. The time evolution of temperature at different points provided the means by which we could estimate the thermal diffusivity, D, of the tissue in which LNThs were placed. In order to accomplish this, we made use of a model developed from the Green's function formalism applied to the bioheat equation (see Section 2.3.2.2). Under this approach, the subcutaneous temperatures during (i) a thermal relaxation and (ii) a laser induced heating procedure were described by **Equation 2.26** and **Equation 2.21**.

**Figure 5.17.** Thermal images obtained by dividing the luminescence images at 1000 and 1200 nm during heating **(a)** and relaxation **(b)** processes. An optical figure of the anesthetized mouse was superimposed. **(c)** Time evolution of the average temperature of the injection area as measured by the subcutaneous LNThs during heating and thermal relaxation processes. The fits according to equation (5.11) and (5.12) are represented as colored solid lines.

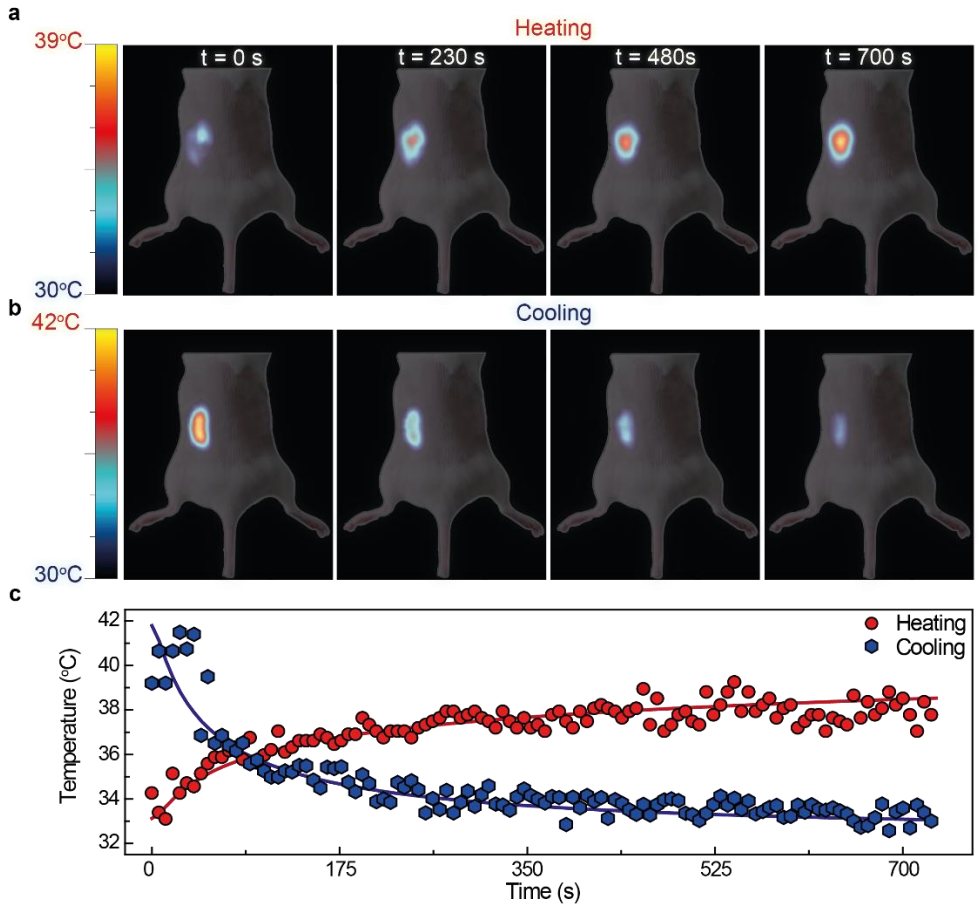


These equations were used to construct a multidimensional fitting – *i.e.*, $r$ and $t$ were considered independent variables - to the experimental data summarized in **Figure 5.17c**. The numerical values of the parameters $a_{690nm}$= 5 mm, $a_{808nm}$= 3 mm, $t_o^{690\ nm}$ = 660 s, $t_o^{808\ nm}$ = 180 s, $z$ = 1 mm, were determined by experimental constraints while $\alpha_{808nm}$ = 0.023 mm$^{-1}$, $\alpha_{690nm}$ = 0.035 mm$^{-1}$, ρ = 10$^{-3}$ g mm$^{-3}$ and c = 3.7 J g$^{-1}$ K$^{-1}$ were data extracted from literature (BASHKATOV et al., 2005; JACQUES, 2013; XIMENDES et al., 2016b). Under this approach the thermal diffusivity of the tissue, D, was the only variable parameter. Best fitting between model and experimental data corresponding to the heating cycle provided a value of D = 0.15 ± 0.02 mm$^2$ s$^{-1}$ whereas the fitting of experimental data obtained during the cooling process provided D = 0.12 ± 0.02 mm$^2$ s$^{-1}$. Their respective fitting curves are included as solid colored lines in **Figure 5.17c**. The

proximity of these two values together with the fact that they are in very good agreement with the ones reported in literature (TROMBERG et al., 1997) and the one obtained in Section 5.1.5, $D = 0.13 \pm 0.04 mm^2 s^{-1}$, supports the validity of using Er-Yb@Yb-Tm core/shell $LaF_3$ NPs as accurate and reliable subcutaneous thermal sensors for 2D-SDTI.

# 6. Conclusions

In this chapter, the main results and findings obtained throughout this doctoral thesis are summarized.

The most relevant results concerning the design of heating and self-monitored NPs were:

- The core/shell engineering successfully allowed for the combination of a thermally sensitive core surrounded by a heating shell in a rare earth doped single structure.
- The multifunctionality of the NPs was achieved in different spectral regions – specifically BW-I and BW-II – depending on the doping ions selected.
- For the case of multifunctional core/shell NPs operating in BW-I, the core was doubly doped with $Er^{3+}$ and $Yb^{3+}$ ions while the shell was heavily doped with $Nd^{3+}$ ions.
- Time resolved spectroscopy evidenced an efficient shell-to-core energy transfer that allowed for the generation of the thermosensitive emission of erbium ions at the core after infrared (808 nm) excitation of $Nd^{3+}$ ions at the shell.
- The heating capability of the Er-Yb@Nd $LaF_3$ NPs appeared as a result of the non-radiative de-excitation of $Nd^{3+}$ ions.
- For the case of multifunctional core/shell NPs operating in BW-II, the core was doped with $Yb^{3+}$ ions while the shell was heavily doped with $Nd^{3+}$ ions.
- The ratio between the $Yb^{3+}$ and $Nd^{3+}$ infrared emissions after 808 nm excitation provided a full optical method for remote thermal reading with Yb@Nd* $LaF_3$ NPs.
- The non-radiative de-excitation of $Nd^{3+}$ ions was also responsible for the heating capability of Yb@Nd* $LaF_3$ NPs.

- Even though similar results were presented in literature prior to the development of this thesis (by using hybrids such as optical-magnetic systems), the systems here developed constituted the first optical nanoparticles whose heating and thermal sensing could be achieved under a single optical excitation wavelength. This, in turns, was essential for miniaturizing experimental arrangements and to avoid separation between NHs and NThs within the system under study.
- Their ability for simultaneous heating and thermal sensing allowed for the demonstration of controlled photothermal processes under single infrared beam excitation in both aqueous and tissue environments and hence opened up a new range of possibilities and applications for multi-doped $LaF_3$ core/shell nanoparticles.

Concerning the use of core/shell NPs for the study of *in vivo* thermal dynamics, the main results were:

- The core/shell nanoengineering was successfully used to produce subcutaneous thermal probes operating in the second and/or third biological windows.
- Selective doping during the core/shell growth has been demonstrated to be a promising approach for tailoring luminescence and thermal sensitivity of the nanostructures. In particular, it has been found that if $Yb^{3+}$ and $Nd^{3+}$ emitting ions were spatially separated in the core and shell (or vice versa), a fourfold improvement in the thermal sensitivity was reached. On the other hand, when producing a core/shell structure constituted of a core doped with $Er^{3+}$ and $Yb^{3+}$ ions and a shell doped with $Yb^{3+}$ and $Tm^{3+}$, a five-fold improvement in the thermal sensitivity was achieved.

- The ratio between the $Yb^{3+}$ and $Nd^{3+}$ infrared emissions in Yb@Nd $LaF_3$ NPs provided a full optical method to measure subcutaneous temperatures in a minimally invasive way.
- The intensity ratios between the $Yb^{3+}$ and $Tm^{3+}$ or between $Yb^{3+}$ and $Er^{3+}$ infrared emissions in Er-Yb@Yb-Tm $LaF_3$ NPs provided a full optical method to acquire subcutaneous temperature images in a minimally invasive way.
- Yb@Nd $LaF_3$ NPs were successfully used to measure subcutaneous thermal transients in small animal models from which accurate information about basic properties of tissues (e.g., absorption coefficient and thermal diffusivity) were obtained.
- NIR emitting PbS/CdS/ZnS QDs, when used as deep tissue NThs, were capable of discriminating between the ischemic and inflammatory phases commonly found after artery ligation.
- The contrary effects that blood perfusion and its consequences (atrophy and necrosis) had on the effective thermal diffusivity of damaged tissues were found to be decisive factors in the discrimination between the ischemic and inflammatory phases.
- PbS/CdS/ZnS QDs were capable of time monitoring the revascularization of tissues after temporal restriction of blood supply, evidencing how it lead to a subsequent recovery of the induced ischemic damage.
- Infrared-emitting active-core/active-shell Er-Yb@Yb-Tm $LaF_3$ NPs were successfully used as subcutaneous thermal probes operating in both the second and third biological windows.
- An outstanding thermal sensitivity close to 5 $\%\cdot{}^{o}C^{-1}$ was achieved. The highest thermal sensitivity obtained for a LNTh operating in the

second or third biological windows up to the development of this thesis.

- The high thermal sensitivity in combination with the large optical penetration into tissues of the infrared luminescence of Er-Yb@Yb-Tm $LaF_3$ NPs allowed the acquisition of time resolved two-dimensional thermal images in a small animal model.
- A ratiometric subcutaneous thermal video was recorded for the first time, constituting a relevant advance with previous works dealing with *in vivo* luminescence thermometry in which only punctual dynamic thermal measurements were performed.
- The thermo-physical properties of tissues obtained with the core/shell NPs were found to be in excellent agreement with published data obtained by completely different methods.

In summary, the experiments performed throughout this thesis demonstrated the bright potential of core/shell engineering as it not only provided the basis by which one could produce optical multifunctional nanoparticles operating under a single excitation wavelength but it also extended the applicability of luminescence thermometry at the small animal level, deepening the study of heat transfer and detecting subcutaneous anomalies (in particular, accidents, malfunctions and/or diseases of the cardiovascular system). Thus, at this point, it is safe to say that the challenges presented in **Figure 1.7** were all successfully faced, though not exhaustively, by means of core/shell engineering. Consequently, the effort put into these studies has resulted in the publication of five scientific articles (XIMENDES et al., 2016a, 2016b, 2016c, 2017a, 2017b). Though many of the nanoparticles that were here proposed did not have a thorough investigation of their biocompatibility, we state that the next natural step in our research will, of course, be their functionalization. In this sense, not only proofs of concepts will be presented but actual targeting of biological problems so that in the future we may see the

application of core/shell nanoparticles at the clinical stage.

---

En este capítulo, se resumirán los principales resultados y hallazgos obtenidos a lo largo de esta tesis doctoral.

Los resultados más relevantes relacionados con el diseño de la calefacción y los PN autopercibidos fueron:

- La ingeniería del core/shell permitió con éxito la combinación de un núcleo térmicamente sensible rodeado por una carcasa de calentamiento en una única estructura dopada de tierras raras.
- La multifuncionalidad de las NPs se logró en diferentes regiones espectrales, específicamente BW-I y BW-II, dependiendo de los iones dopantes seleccionados.
- Para el caso de NPs de core/shell multifuncionales que operan en BW-I, el núcleo estaba doblemente dopado con iones $Er^{3+}$ e $Yb^{3+}$ mientras que el caparazón estaba fuertemente dopado con iones $Nd^{3+}$.
- La espectroscopia resuelta en el tiempo evidenció una eficiente transferencia de energía de núcleo a núcleo que permitió la generación de la emisión termosensible de iones de erbio en el núcleo después de la excitación infrarroja (808 nm) de los iones $Nd^{3+}$ en el caparazón.
- La capacidad de calentamiento de las NPs Er-Yb@Nd $LaF_3$ apareció como resultado de la de-excitación no radiativa de los iones $Nd^{3+}$.
- Para el caso de las NPs de core/shell que operan en BW-II, el núcleo estaba dopado con iones $Yb^{3+}$ mientras que el caparazón estaba fuertemente dopado con iones $Nd^{3+}$.

- La relación entre las emisiones de infrarrojos $Yb^{3+}$ y $Nd^{3+}$ después de la excitación de 808 nm proporcionó un método óptico completo para la lectura térmica remota con Yb@Nd * NP $LaF_3$.
- La desexcitación no radiativa de los iones $Nd^{3+}$ también fue responsable por la capacidad de calentamiento de las NPs Yb@Nd * NP $LaF_3$.
- Aunque en la literatura se presentaron resultados similares antes del desarrollo de esta tesis (mediante el uso de híbridos tales como sistemas ópticos magnéticos), los sistemas aquí desarrollados constituyeron las primeras nanopartículas ópticas cuya calefacción y detección térmica podrían lograrse bajo una sola longitud de onda de excitación. Esto, a su vez, fue esencial para miniaturizar los arreglos experimentales y evitar la separación entre NH y NTh dentro del sistema en estudio.
- Su capacidad de calentamiento y detección térmica simultáneos permitieron la demostración de procesos fototérmicos controlados bajo excitación de un solo haz de infrarrojos en ambientes acuosos y tisulares y, por lo tanto, abrió un nuevo rango de posibilidades y aplicaciones para nanopartículas core/shell de $LaF_3$ multi-dopadas.

En lo que respecta al uso de NPs core/shell para el estudio de la dinámica térmica *in vivo*, los principales resultados fueron:

- La nanoingeniería core/shell fue utilizada con éxito para producir sondas térmicas subcutáneas que operan en la segunda y/o tercera ventanas biológicas.
- El dopaje selectivo durante el crecimiento del núcleo/caparazón ha demostrado ser un enfoque prometedor para adaptar la luminiscencia y la sensibilidad térmica de las nanoestructuras. En particular, se ha encontrado que si los iones emisores de $Yb^{3+}$ y $Nd^{3+}$

se separaban espacialmente en el núcleo y la carcasa (o viceversa), se alcanzaba una mejora de cuatro veces en la sensibilidad térmica. Por otro lado, cuando se produce una estructura núcleo/caparazón constituida por un núcleo dopado con iones $Er^{3+}$ e $Yb^{3+}$ y un caparazón dopado con $Yb^{3+}$ y $Tm^{3+}$, se logró una mejora de cinco veces en la sensibilidad térmica.

- La relación entre las emisiones en el infrarrojo de $Yb^{3+}$ y $Nd^{3+}$ en las NP de Yb@Nd $LaF_3$ proporcionó un método óptico completo para medir las temperaturas subcutáneas de una manera mínimamente invasiva.
- Las relaciones de intensidad entre las emisiones infrarrojas de $Yb^{3+}$ y $Tm^{3+}$ o entre $Yb^{3+}$ y $Er^{3+}$ en las NPs Er-Yb@Yb-Tm LaF3 proporcionaron un método óptico completo para adquirir imágenes subcutáneas de temperatura de una manera mínimamente invasiva.
- Las NPs Yb@Nd $LaF_3$ se usaron con éxito para medir transientes térmicos subcutáneos en modelos de animales pequeños a partir de los cuales se obtuvo información precisa sobre las propiedades básicas de los tejidos (p. ej., coeficiente de absorción y difusividad térmica).
- Los QDs PbS/CdS/ZnS que emiten en el infrarrojo cercano, cuando se usados como termómetros de tejido profundo, fueron capaces de discriminar entre las fases isquémica e inflamatoria que se encuentran comúnmente después de la ligadura de la arteria.
- Los efectos contrarios que la perfusión sanguínea y sus consecuencias (atrofia y necrosis) tuvieron sobre la difusividad térmica efectiva de los tejidos dañados se encontraron como factores decisivos en la discriminación entre las fases isquémica e inflamatoria.

- Los QDs de PbS/CdS/ZnS fueron capaces de controlar el tiempo de la revascularización de los tejidos después de la restricción temporal del flujo de sangre, lo que demuestra cómo conduce a una recuperación posterior del daño isquémico inducido.
- Las NPs de $LaF_3$ Er-Yb@Yb-Tm que emiten en el infrarrojo fueron usadas con éxito como sondas térmicas subcutáneas que operan tanto en la segunda como en la tercera ventanas biológicas.
- Se logró una sensibilidad térmica excepcional cercana al $5\%\cdot{}^{o}C^{-1}$. La mayor sensibilidad térmica obtenida para un LNTh que opera en el segundo o tercer biológico hasta el desarrollo de esta tesis.
- La alta sensibilidad térmica en combinación con la gran penetración óptica en los tejidos de la luminiscencia infrarroja de las NPs $LaF_3$ de Er-Yb@Yb-Tm permitió la adquisición de imágenes térmicas bidimensionales resueltas en el tiempo en un modelo de animal pequeño.
- Se registró un video térmico subcutáneo radiométrico por primera vez, constituyendo un avance relevante con los trabajos previos que trataban de la termometría de luminiscencia *in vivo* en la que solo se realizaban mediciones térmicas dinámicas puntuales.
- Se encontró que las propiedades termo-físicas de los tejidos obtenidos con las NPs de núcleo/capa están en excelente acuerdo con los datos publicados y obtenidos por métodos completamente diferentes.

En resumen, los experimentos realizados a lo largo de esta tesis demostraron el brillante potencial de la ingeniería *core/shell* ya que no solo proporcionaba la base para producir nanopartículas ópticas multifuncionales operando bajo una sola longitud de onda de excitación sino que también extendía la aplicabilidad de la termometría de luminiscencia en el nivel de animales de

pequeño tamaño, profundizando el estudio de la transferencia de calor y detectando anomalías subcutáneas (en particular, accidentes, disfunciones y / o enfermedades del sistema cardiovascular). Por lo tanto, en este punto, es seguro decir que los desafíos presentados en la **Figure 1.7** fueron exitosamente enfrentados, aunque no exhaustivamente, por medio de la ingeniería *core/shell*. En consecuencia, el esfuerzo puesto en estos estudios ha resultado en la publicación de cinco artículos científicos (XIMENDES et al., 2016a, 2016b, 2016c, 2017a, 2017b). Aunque muchas de las nanopartículas que se propusieron aquí no tuvieron una investigación exhaustiva de su biocompatibilidad, afirmamos que el próximo paso natural en nuestra investigación será, por supuesto, su funcionalización. En este sentido, no solo se presentarán pruebas de conceptos, sino que se enfocarán en problemas biológicos para posibilitar la aplicación de nanopartículas *core/shell* en la etapa clínica.

---

Neste capítulo, estão resumidos os principais resultados e descobertas obtidos nesta tese de doutorado.

Os resultados mais relevantes relativos ao design de NPs aquecedoras e auto-monitoradas foram:

- A engenharia de núcleo/casca permitiu, com sucesso, a combinação de um núcleo termicamente sensível rodeado por uma casca de aquecimento em uma única estrutura dopada com terras raras.
- A multifuncionalidade das NPs foi atingida em diferentes regiões espectrais – especificamente BW-I e BW-II – a depender dos íons dopantes selecionados.
- Para o caso de NPs multifuncionais de núcleo/casca operando na BW-I, o núcleo foi duplamente dopado com $Er^{3+}$ e $Yb^{3+}$ ions enquanto que a casca foi altamente dopada com íons de $Nd^{3+}$.

- A espectroscopia resolvida no tempo evidenciou uma transferência de energia eficiente do núcleo para a casca que permitiu a geração da emissão termosensível dos íons de érbio no núcleo após excitação infravermelha (808 nm) dos íons de $Nd^{3+}$ na casca.
- A capacidade aquecedora das NPs de Er-Yb@Nd $LaF_3$ NPs surgiu como um resultado da desexcitação não-radiativa dos íons de $Nd^{3+}$.
- Para o caso de NPs multifuncionais de núcleo/casca operando na BW-II, o núcleo foi dopado com íons de $Yb^{3+}$ enquanto que a casca foi altamente dopada com íons de $Nd^{3+}$.
- A razão entre as emissões infravermelhas de $Yb^{3+}$ e $Nd^{3+}$ após excitação a 808 nm forneceu um método óptico complete para sensoriamento térmico remote com NPs de Yb@Nd* $LaF_3$.
- A desexcitação não-radiativa dos íons de $Nd^{3+}$ também foi responsável pela capacidade aquecedora das NPs de Yb@Nd* $LaF_3$.
- Apesar de resultados similares terem sido apresentados na literature antes do desenvolvimento dessa tessa (ao usar híbridos como sistemas magneto-ópticos), os sistemas aqui desenvolvidos constituíram as primeiras nanopartículas ópticas cujo aquecimento e sensoriamento térmico poderiam ser atingidos por meio de um único comprimento de onda de excitação. Isso, por sua vez, foi essencial para miniaturizar o setup experimental e para evitar a separação entre nanoaquecedores e nanotermômetros no sistema sob estudo.
- A habilidade dessas NPs para aquecimento e sensoriamento térmico simultâneo permitiu a demonstração de processos fototérmicos controlados sob um único feixe de excitação infravermelha em meios aquosos e teciduais e, portanto, abriram um leque de possibilidades e aplicações para nanopartículas $LaF_3$ de núcleo/casca multi-dopadas.

Concernente ao uso de NPs de núcleo/casca para o estudo da dinâmica térmica *in vivo*, os principais resultados foram:

- A engenharia de núcleo/casca foi usada com sucesso para produzir sondas térmicas subcutâneas operando na segunda e/ou terceira janelas biológicas.
- A dopagem seletiva durante o crescimento de núcleo/casca demonstrou ser uma abordagem promissora para melhorar a luminescência e a sensibilidade térmica de nanoestruturas. Em particular, descobriu-se que se os íons emissores de $Yb^{3+}$ e $Nd^{3+}$ forem espacialmente separados no núcleo e na casca (ou vice versa), a sensibilidade térmica é aumentada em até quatro vezes. Por outro lado, ao produzir uma estrutura constituída de um núcleo dopado com íons de $Er^{3+}$ e $Yb^{3+}$ e uma casca dopada com $Yb^{3+}$ e $Tm^{3+}$, a sensibilidade térmica foi aumentada em até cinco vezes.
- A razão entre as emissões infravermelhas de $Yb^{3+}$ e $Nd^{3+}$ nas NPs de Yb@Nd forneceram um método óptico complete para medir subcutaneamente as temperaturas de maneira minimamente invasiva.
- As razões entre as intensidades de emissão infravermelha entre $Yb^{3+}$ e $Tm^{3+}$ ou entre $Yb^{3+}$ e $Er^{3+}$ nas NPs de Er-Yb@Yb-Tm $LaF_3$ forneceram um método óptico complete para aquisição de imagens térmicas subcutâneas de uma maneira minimamente invasiva.
- As NPs de Yb@Nd $LaF_3$ foram usadas com sucesso para medir transientes térmicos subcutâneos em pequenos animais, a partir os quais informações precisas sobre propriedades básicas dos tecidos (como, por exemplo, coeficiente de absorção e difusividade térmica) foram obtidas.

- Pontos quânticos de PbS/CdS/ZnS emitindo no infravermelho próximo, quando usados como nanotermômetros subcutâneos, foram capazes de discriminar entre as fases isquêmica e inflamatória comumente encontradas depois da ligação de uma artéria.
- Os efeitos contrários que a perfusão de sangue e suas consequências (atrofia e necrose) tiveram sobre a difusividade térmica efetiva de tecidos danificados foram descritos como fatores decisivos na discriminação entre as fases isquêmica e inflamatória.
- Pontos quânticos de PbS/CdS/ZnS foram capazes de monitorar no tempo a revascularização de tecidos após uma restrição temporal de fluxo de sangue, evidenciando como isso levou a uma recuperação subsequente do dano isquêmico induzido.
- NPs de Er-Yb@Yb-Tm $LaF_3$ emitindo no infravermelho foram usadas com sucesso como sondas térmicas subcutâneas operando tanto na segunda quanto na terceira janela biológica.
- Uma surpreendente sensibilidade térmica de 5 $\%\cdot{}^{o}C^{-1}$ foi atingida. A mais alta obtida para um nanotermômetro luminescente operando na segunda ou terceira janela biológica até o desenvolvimento dessa tese.
- A alta sensibilidade térmica em combinação com a alta penetração óptica em tecidos da luminescência das NPs de Er-Yb@Yb-Tm $LaF_3$ permitiu a aquisição de imagens térmicas 2D resolvidas no tempo em modelos de animais pequenos.
- Um video térmico subcutâneo e ratiométrico foi gravado pela primeira vez, constituindo um avanço significativo em relação a trabalhos prévios lidando com a termometria luminescente *in vivo* que, até o momento, havia realizado apenas medidas dinâmicas pontuais.

- As propriedades termo-físicas dos tecidos obtidas por meio das NPs de núcleo/casca estavam em ótimo acordo com dados publicados na literatura e obtidos por métodos completamente diferentes.

Em resumo, os experimentos realizados durante essa tese demonstratam o grande potencial da engenharia de núcleo/casca uma vez que ela não somente forneceu a base pela qual pode-se produzir nanopartículas multifuncionais operando sob um único feixe de excitação mas também extendeu a aplicabilidade da termometria luminescente a nível de animais pequenos, aprofundando o estudo da trasnferência de calor e detectando anomalias subcutâneas (em particular, acidentes, disfunções e/ou doenças no sistema cardiovascular). Portanto, a essa altura, é seguro dizer que os desafios apresentados na **Figure 1.7** foram todos enfrentados com sucesso, ainda que não de maneira exaustiva, por meio da engenharia de núcleo/casca. Consequentemente, o esforço colocado nesses estudos resultou na publicação de cinco artigos científicos (XIMENDES et al., 2016a, 2016b, 2016c, 2017a, 2017b). Apesar de algumas das nanopartículas aqui apresentadas não terem sido submetidas a uma investigação rigorosa de sua biocompatibilidade, asseguramos que o próximo passo natural de nossa pesquisa será sua funcionalização. Sendo assim, não apenas provas de conceitos serão apresentadas mas o alvejar de problemas biológicos para que, a pequenos passos, possamos um dia possibilitar a aplicação de nanopartículas a nível clínico.

# References

AI, F. et al. A core-shell-shell nanoplatform upconverting near-infrared light at 808 nm for luminescence imaging and photodynamic therapy of cancer. **Scientific Reports**, [s. l.], v. 5, n. 1, 2015. Disponível em: <http://www.nature.com/articles/srep10785>. Acesso em: 16 fev. 2018.

AIGOUY, L. et al. Scanning thermal imaging of microelectronic circuits with a fluorescent nanoprobe. **Applied Physics Letters**, [s. l.], v. 87, n. 18, p. 184105, 2005.

ALENCAR, M. A. R. C. et al. Er3+-doped BaTiO3 nanocrystals for thermometry: Influence of nanoenvironment on the sensitivity of a fluorescence based temperature sensor. **Applied Physics Letters**, [s. l.], v. 84, n. 23, p. 4753–4755, 2004.

ALLISON, S. W.; GILLIES, G. T. Remote thermometry with thermographic phosphors: Instrumentation and applications. **Review of Scientific Instruments**, [s. l.], v. 68, n. 7, p. 2615–2650, 1997.

ANDREAKOU, P. et al. Size- and Temperature-Dependent Carrier Dynamics in Oleic Acid Capped PbS Quantum Dots. **The Journal of Physical Chemistry C**, [s. l.], v. 117, n. 4, p. 1887–1892, 2013.

AOI, N. et al. Ultrasound Assessment of Deep Tissue Injury in Pressure Ulcers: Possible Prediction of Pressure Ulcer Progression: **Plastic and Reconstructive Surgery**, [s. l.], v. 124, n. 2, p. 540–550, 2009.

ARAI, S. et al. Micro-thermography in millimeter-scale animals by using orally-dosed fluorescent nanoparticle thermosensors. **The Analyst**, [s. l.], v. 140, n. 22, p. 7534–7539, 2015.

BAKER, J. M.; FORD, N. C. Dependence of Spin-Lattice Relaxation Time Upon Magnetic Field for Two Salts of Neodymium. **Physical Review**, [s. l.], v. 136, n. 6A, p. A1692–A1701, 1964.

BAKER, S. N.; MCCLESKEY, T. M.; BAKER, G. A. An Ionic Liquid-Based Optical Thermometer. In: ROGERS, R. D.; SEDDON, K. R. (Eds.). **Ionic Liquids IIIB: Fundamentals, Progress, Challenges, and Opportunities**. Washington, DC: American Chemical Society, 2005. v. 902p. 171–181.

BALABHADRA, S. et al. Boosting the sensitivity of $Nd^{3+}$ -based luminescent nanothermometers. **Nanoscale**, [s. l.], v. 7, n. 41, p. 17261–17267, 2015.

BARBOSA-GARCÍA, O. et al. Neodymium-to-erbium nonradiative energy transfer and fast initial fluorescence decay of the ^4F_3/2 state of neodymium in garnet crystals. **Journal of the Optical Society of America B**, [s. l.], v. 14, n. 10, p. 2731, 1997.

BASHKATOV, A. N. et al. Optical properties of human skin, subcutaneous and mucous tissues in the wavelength range from 400 to 2000 nm. **Journal of Physics D: Applied Physics**, [s. l.], v. 38, n. 15, p. 2543–2555, 2005.

BECKER, S. M. One-Dimensional Transient Heat Conduction in Composite Living Perfuse Tissue. **Journal of Heat Transfer**, [s. l.], v. 135, n. 7, p. 071002, 2013.

BEDNARKIEWICZ, A. et al. Optically stimulated heating using Nd3+ doped NaYF4 colloidal near infrared nanophosphors. **Applied Physics B**, [s. l.], v. 103, n. 4, p. 847–852, 2011.

BENAYAS, A. et al. PbS/CdS/ZnS Quantum Dots: A Multifunctional Platform for In Vivo Near-Infrared Low-Dose Fluorescence Imaging. **Advanced Functional Materials**, [s. l.], v. 25, n. 42, p. 6650–6659, 2015.

BERGMAN, T. L.; INCROPERA, F. P. (EDS.). **Fundamentals of heat and mass transfer**. 7th ed ed. Hoboken, NJ: Wiley, 2011.

BERTHOU, H.; JÖRGENSEN, C. K. Optical-fiber temperature sensor based on upconversion-excited fluorescence. **Optics Letters**, [s. l.], v. 15, n. 19, p. 1100, 1990.

BHARGAVA, A.; CHANMUGAM, A.; HERMAN, C. Heat transfer model for deep tissue injury: a step towards an early thermographic diagnostic capability. **Diagnostic Pathology**, [s. l.], v. 9, n. 1, p. 36, 2014.

BRIGGER, I.; DUBERNET, C.; COUVREUR, P. Nanoparticles in cancer therapy and diagnosis. **Advanced drug delivery reviews**, [s. l.], v. 54, n. 5, p. 631–651, 2002.

BRITES, C. D. S. et al. Thermometry at the nanoscale. **Nanoscale**, [s. l.], v. 4, n. 16, p. 4799, 2012.

BRITES, C. D. S.; MILLÁN, A.; CARLOS, L. D. Lanthanides in Luminescent Thermometry. In: **Handbook on the Physics and Chemistry of Rare Earths**. [s.l.] : Elsevier, 2016. v. 49p. 339–427.

BROOKS, J. P. et al. Thermal imaging in the detection of bowel ischemia. **Diseases of the Colon and Rectum**, [s. l.], v. 43, n. 9, p. 1319–1321, 2000.

BROWN, J. M.; WILSON, W. R. Exploiting tumour hypoxia in cancer treatment. **Nature Reviews Cancer**, [s. l.], v. 4, n. 6, p. 437–447, 2004.

BULLEN, C.; MULVANEY, P. The Effects of Chemisorption on the Luminescence of CdSe Quantum Dots. **Langmuir**, [s. l.], v. 22, n. 7, p. 3007–3013, 2006.

CARDEN, D. L.; GRANGER, D. N. Pathophysiology of ischaemia-reperfusion injury. **The Journal of Pathology**, [s. l.], v. 190, n. 3, p. 255–266, 2000.

CARLSON, M. T.; KHAN, A.; RICHARDSON, H. H. Local Temperature Determination of Optically Excited Nanoparticles and Nanodots. **Nano Letters**, [s. l.], v. 11, n. 3, p. 1061–1069, 2011.

CARRASCO, E. et al. Intratumoral Thermal Reading During Photo-Thermal Therapy by Multifunctional Fluorescent Nanoparticles. **Advanced Functional Materials**, [s. l.], v. 25, n. 4, p. 615–626, 2015.

CARUSO, F. Nanoengineering of Particle Surfaces. **Advanced Materials**, [s. l.], v. 13, n. 1, p. 11–22, 2001.

CASSETTE, E. et al. Design of new quantum dot materials for deep tissue infrared imaging. **Advanced Drug Delivery Reviews**, [s. l.], v. 65, n. 5, p. 719–731, 2013.

CERÓN, E. N. et al. Hybrid Nanostructures for High-Sensitivity Luminescence Nanothermometry in the Second Biological Window. **Advanced Materials**, [s. l.], v. 27, n. 32, p. 4781–4787, 2015.

ÇETINGÜL, M. P.; HERMAN, C. A heat transfer model of skin tissue for the detection of lesions: sensitivity analysis. **Physics in Medicine and Biology**, [s. l.], v. 55, n. 19, p. 5933–5951, 2010.

CHALFIE, M. et al. Green fluorescent protein as a marker for gene expression. **Science**, [s. l.], v. 263, n. 5148, p. 802–805, 1994.

CHARGÉ, S. B. P.; RUDNICKI, M. A. Cellular and Molecular Regulation of Muscle Regeneration. **Physiological Reviews**, [s. l.], v. 84, n. 1, p. 209–238, 2004.

CHASTAGNER, M. W. et al. Measurement and Modeling of Tissue Thermal Conductivity With Variable Water Content and Compression. **Journal of Heat Transfer**, [s. l.], v. 138, n. 7, p. 074503, 2016.

CHEN, G. et al. ($\alpha$-$NaYbF_4$:$Tm^{3+}$)/$CaF_2$ Core/Shell Nanoparticles with Efficient Near-Infrared to Near-Infrared Upconversion for High-Contrast Deep Tissue Bioimaging. **ACS Nano**, [s. l.], v. 6, n. 9, p. 8280–8287, 2012.

CHENG, L. et al. Organic Stealth Nanoparticles for Highly Effective *in Vivo* Near-Infrared Photothermal Therapy of Cancer. **ACS Nano**, [s. l.], v. 6, n. 6, p. 5605–5613, 2012.

CHICHEŁ, A. et al. Hyperthermia – description of a method and a review of clinical applications. **Reports of Practical Oncology & Radiotherapy**, [s. l.], v. 12, n. 5, p. 267–275, 2007.

COLLINS, A. J. et al. Quantitation of thermography in arthritis using multi-isothermal analysis. I. The thermographic index. **Annals of the Rheumatic Diseases**, [s. l.], v. 33, n. 2, p. 113–115, 1974.

COLLINS, S. F. et al. Comparison of fluorescence-based temperature sensor schemes: Theoretical analysis and experimental validation. **Journal of Applied Physics**, [s. l.], v. 84, n. 9, p. 4649–4654, 1998.

COOKE, D. W. et al. Temperature-dependent luminescence of cerium-doped ytterbium oxyorthosilicate. **Journal of Luminescence**, [s. l.], v. 79, n. 3, p. 185–190, 1998.

COOKE, D. W. et al. Intrinsic ultraviolet luminescence from Lu2O3, Lu2SiO5 and Lu2SiO5:Ce3+. **Journal of Luminescence**, [s. l.], v. 106, n. 2, p. 125–132, 2004.

COOPER, T. E.; TREZEK, G. J. Correlation of thermal properties of some human tissue with water content. **Aerospace Medicine**, [s. l.], v. 42, n. 1, p. 24–27, 1971.

COWLES, E. A. et al. Near-infrared optical imaging for monitoring the regeneration of osteogenic tissue-engineered constructs. **BioResearch open access**, [s. l.], v. 2, n. 3, p. 186–191, 2013.

DE SOUSA, D. F. et al. Spectroscopy of Nd3+ and Yb3+ codoped fluoroindogallate glasses. **Journal of Applied Physics**, [s. l.], v. 90, n. 7, p. 3308–3313, 2001.

DEBASU, M. L. et al. All-In-One Optical Heater-Thermometer Nanoplatform Operative From 300 to 2000 K Based on $Er^{3+}$ Emission and Blackbody Radiation. **Advanced Materials**, [s. l.], v. 25, n. 35, p. 4868–4874, 2013.

DEL ROSAL, B. et al. Flow effects in the laser-induced thermal loading of optical traps and optofluidic devices. **Optics Express**, [s. l.], v. 22, n. 20, p. 23938, 2014.

DEL ROSAL, B. et al. Infrared-Emitting QDs for Thermal Therapy with Real-Time Subcutaneous Temperature Feedback. **Advanced Functional Materials**, [s. l.], v. 26, n. 33, p. 6060–6068, 2016. a.

DEL ROSAL, B. et al. In Vivo Luminescence Nanothermometry: from Materials to Applications. **Advanced Optical Materials**, [s. l.], v. 5, n. 1, p. 1600508, 2016. b.

DEWEY, W. C.; DIEDERICH, C. J. Hyperthermia classic commentary: 'Arrhenius relationships from the molecule and cell to the clinic' by William Dewey, ***Int. J. Hyperthermia*** , 10:457–483, 1994. **International Journal of Hyperthermia**, [s. l.], v. 25, n. 1, p. 21–24, 2009.

DIAO, C.; ZHU, L.; WANG, H. Cooling and rewarming for brain ischemia or injury: theoretical analysis. **Annals of Biomedical Engineering**, [s. l.], v. 31, n. 3, p. 346–353, 2003.

DOKE, G. et al. Photoluminescence of neodymium and erbium doped NaLaF4 material. **Radiation Measurements**, [s. l.], v. 56, p. 27–30, 2013.

DONNER, J. S. et al. Imaging of Plasmonic Heating in a Living Organism. **ACS Nano**, [s. l.], v. 7, n. 10, p. 8666–8672, 2013.

DU, P. et al. Optical temperature sensor based on upconversion emission in Er-doped ferroelectric 0.5Ba(Zr $_{0.2}$ Ti $_{0.8}$ )O $_{3}$ -0.5(Ba $_{0.7}$ Ca $_{0.3}$ )TiO $_{3}$ ceramic. **Applied Physics Letters**, [s. l.], v. 104, n. 15, p. 152902, 2014.

DUARTE, M. et al. De-excitation mechanisms of BaLiF3:Co2+ crystals. **Optics Communications**, [s. l.], v. 159, n. 4–6, p. 221–224, 1999.

DVIR, T. et al. Nanoparticles Targeting the Infarcted Heart. **Nano Letters**, [s. l.], v. 11, n. 10, p. 4411–4414, 2011.

ELSAYED, I.; HUANG, X.; ELSAYED, M. Selective laser photo-thermal therapy of epithelial carcinoma using anti-EGFR antibody conjugated gold nanoparticles. **Cancer Letters**, [s. l.], v. 239, n. 1, p. 129–135, 2006.

ELTZSCHIG, H. K.; ECKLE, T. Ischemia and reperfusion—from mechanism to translation. **Nature Medicine**, [s. l.], v. 17, n. 11, p. 1391–1401, 2011.

ENGLAND, C. G. et al. Re-assessing the enhanced permeability and retention effect in peripheral arterial disease using radiolabeled long circulating nanoparticles. **Biomaterials**, [s. l.], v. 100, p. 101–109, 2016.

FERRARI, M. Cancer nanotechnology: opportunities and challenges. **Nature Reviews Cancer**, [s. l.], v. 5, n. 3, p. 161–171, 2005.

FRANGIONI, J. V. In vivo near-infrared fluorescence imaging. **Current opinion in chemical biology**, [s. l.], v. 7, n. 5, p. 626–634, 2003.

FURZIKOV, N. Different lasers for angioplasty: Thermooptical comparison. **IEEE Journal of Quantum Electronics**, [s. l.], v. 23, n. 10, p. 1751–1755, 1987.

GARCÍA SOLÉ, J.; BAUSÁ, L. E.; JAQUE, D. **An introduction to the optical spectroscopy of inorganic solids**. Hoboken, NJ: J. Wiley, 2005.

GIERING, K. et al. Determination of the specific heat capacity of healthy and tumorous human tissue. **Thermochimica Acta**, [s. l.], v. 251, p. 199–205, 1995.

GODOY, S. E. et al. Dynamic infrared imaging for skin cancer screening. **Infrared Physics & Technology**, [s. l.], v. 70, p. 147–152, 2015.

GONZÁLEZ-PÉREZ, S. et al. Temperature dependence of Nd3+→Yb3+ energy transfer processes in co-doped oxyfluoride glass ceramics. **Journal of Non-Crystalline Solids**, [s. l.], v. 353, n. 18–21, p. 1951–1955, 2007.

GUI, R. et al. Recent advances in synthetic methods and applications of colloidal silver chalcogenide quantum dots. **Coordination Chemistry Reviews**, [s. l.], v. 296, p. 91–124, 2015.

HABASH, R. W. Y. et al. Thermal therapy, part 1: an introduction to thermal therapy. **Critical Reviews in Biomedical Engineering**, [s. l.], v. 34, n. 6, p. 459–489, 2006.

HAINFELD, J. F.; SLATKIN, D. N.; SMILOWITZ, H. M. The use of gold nanoparticles to enhance radiotherapy in mice. **Physics in Medicine and Biology**, [s. l.], v. 49, n. 18, p. N309-315, 2004.

HARDY, J. D. The Physical Laws of Heat Loss from the Human Body. **Proceedings of the National Academy of Sciences**, [s. l.], v. 23, n. 12, p. 631–637, 1937.

HEMMER, E. et al. Exploiting the biological windows: current perspectives on fluorescent bioprobes emitting above 1000 nm. **Nanoscale Horizons**, [s. l.], v. 1, n. 3, p. 168–184, 2016.

HENDERSON, B.; IMBUSCH, G. F. **Optical spectroscopy of inorganic solids**. Oxford [Oxfordshire] : New York: Clarendon Press ; Oxford University Press, 1989.

HERMAN, C. The role of dynamic infrared imaging in melanoma diagnosis. **Expert Review of Dermatology**, [s. l.], v. 8, n. 2, p. 177–184, 2013.

HILDEBRANDT, B. et al. The cellular and molecular basis of hyperthermia. **Critical Reviews in Oncology/Hematology**, [s. l.], v. 43, n. 1, p. 33–56, 2002.

HOENER, C. F. et al. Demonstration of a shell-core structure in layered cadmium selenide-zinc selenide small particles by x-ray photoelectron and Auger spectroscopies. **The Journal of Physical Chemistry**, [s. l.], v. 96, n. 9, p. 3812–3817, 1992.

HONG, G. et al. In Vivo Fluorescence Imaging with $Ag_2S$ Quantum Dots in the Second Near-Infrared Region. **Angewandte Chemie International Edition**, [s. l.], v. 51, n. 39, p. 9818–9821, 2012.

HONMA, I.; SANO, T.; KOMIYAMA, H. Surface-enhanced Raman scattering (SERS) for semiconductor microcrystallites observed in silver-cadmium sulfide hybrid particles. **The Journal of Physical Chemistry**, [s. l.], v. 97, n. 25, p. 6692–6695, 1993.

HUANG, L.; LIU, L.-S. Simultaneous determination of thermal conductivity and thermal diffusivity of food and agricultural materials using a transient plane-source method. **Journal of Food Engineering**, [s. l.], v. 95, n. 1, p. 179–185, 2009.

HUANG, S. et al. Highly fluorescent and bioresorbable polymeric nanoparticles with enhanced photostability for cell imaging. **Nanoscale**, [s. l.], v. 7, n. 3, p. 889–895, 2015.

HUANG, X.; LIN, J. Active-core/active-shell nanostructured design: an effective strategy to enhance $Nd^{3+}$ /$Yb^{3+}$ cascade sensitized upconversion luminescence in lanthanide-doped nanoparticles. **Journal of Materials Chemistry C**, [s. l.], v. 3, n. 29, p. 7652–7657, 2015.

JACQUES, S. L. Corrigendum: Optical properties of biological tissues: a review. **Physics in Medicine and Biology**, [s. l.], v. 58, n. 14, p. 5007–5008, 2013.

JAQUE, D. et al. Nd 3 + → Yb 3 + energy transfer in the YAl 3 ( B O 3 ) 4 nonlinear laser crystal. **Physical Review B**, [s. l.], v. 68, n. 3, 2003. Disponível em: <https://link.aps.org/doi/10.1103/PhysRevB.68.035118>. Acesso em: 14 fev. 2018.

JAQUE, D. et al. Nanoparticles for photothermal therapies. **Nanoscale**, [s. l.], v. 6, n. 16, p. 9494–9530, 2014. a.

JAQUE, D. et al. Fluorescent nanothermometers for intracellular thermal sensing. **Nanomedicine**, [s. l.], v. 9, n. 7, p. 1047–1062, 2014. b.

JAQUE, D.; VETRONE, F. Luminescence nanothermometry. **Nanoscale**, [s. l.], v. 4, n. 15, p. 4301, 2012.

JAQUE GARCÍA, D.; GARCÍA SOLÉ, J. Chapter 4. Quantum Dot Fluorescence Thermometry. In: CARLOS, L.; PALACIO, F. (Eds.). **RSC Nanoscience & Nanotechnology**. Cambridge: Royal Society of Chemistry, 2015. p. 83–123.

JENNINGS, R. B. et al. Relation between high energy phosphate and lethal injury in myocardial ischemia in the dog. **The American Journal of Pathology**, [s. l.], v. 92, n. 1, p. 187–214, 1978.

JING, P. et al. Temperature-Dependent Photoluminescence of CdSe-Core CdS/CdZnS/ZnS-Multishell Quantum Dots. **The Journal of Physical Chemistry C**, [s. l.], v. 113, n. 31, p. 13545–13550, 2009.

JING-LIANG LI; MIN GU. Gold-Nanoparticle-Enhanced Cancer Photothermal Therapy. **IEEE Journal of Selected Topics in Quantum Electronics**, [s. l.], v. 16, n. 4, p. 989–996, 2010.

JOHANNSEN, M. et al. Clinical hyperthermia of prostate cancer using magnetic nanoparticles: presentation of a new interstitial technique. **International Journal of Hyperthermia: The Official Journal of European Society for Hyperthermic Oncology, North American Hyperthermia Group**, [s. l.], v. 21, n. 7, p. 637–647, 2005.

KAMIMURA, M. et al. Ratiometric near-infrared fluorescence nanothermometry in the OTN-NIR (NIR II/III) biological window based on rare-earth doped β-$NaYF_4$ nanoparticles. **Journal of Materials Chemistry B**, [s. l.], v. 5, n. 10, p. 1917–1925, 2017.

KANG, H. et al. Enhanced photothermal therapy assisted with gold nanorods using a radially polarized beam. **Applied Physics Letters**, [s. l.], v. 96, n. 6, p. 063702, 2010.

KIM, J. et al. Targeted Delivery of Nanoparticles to Ischemic Muscle for Imaging and Therapeutic Angiogenesis. **Nano Letters**, [s. l.], v. 11, n. 2, p. 694–700, 2011.

KIM, K. et al. Ultra-High Vacuum Scanning Thermal Microscopy for Nanometer Resolution Quantitative Thermometry. **ACS Nano**, [s. l.], v. 6, n. 5, p. 4248–4257, 2012.

KIM, K.; GUO, Z. Thermal Relaxation Times in Biological Tissues Subjected to Pulsed Laser Irradiation. In: 2006, **Anais**... : American Institute of Aeronautics and

Astronautics, 2006. Disponível em: <http://arc.aiaa.org/doi/10.2514/6.2006-2938>. Acesso em: 15 fev. 2018.

KLIMOV, V.; BOLIVAR, P. H.; KURZ, H. Ultrafast carrier dynamics in semiconductor quantum dots. **Physical Review B**, [s. l.], v. 53, n. 3, p. 1463–1467, 1996.

KUCSKO, G. et al. Nanometre-scale thermometry in a living cell. **Nature**, [s. l.], v. 500, n. 7460, p. 54–58, 2013.

KUMAR, G. A. et al. Optical Characterization of Infrared Emitting Rare-Earth-Doped Fluoride Nanocrystals and Their Transparent Nanocomposites. **Chemistry of Materials**, [s. l.], v. 19, n. 6, p. 1523–1528, 2007.

KUSAMA, H.; SOVERS, O. J.; YOSHIOKA, T. Line Shift Method for Phosphor Temperature Measurements. **Japanese Journal of Applied Physics**, [s. l.], v. 15, n. 12, p. 2349–2358, 1976.

LAMBERT, T. N. et al. Water-Soluble Germanium(0) Nanocrystals: Cell Recognition and Near-Infrared Photothermal Conversion Properties. **Small**, [s. l.], v. 3, n. 4, p. 691–699, 2007.

LEE, D.-E. et al. Multifunctional nanoparticles for multimodal imaging and theragnosis. **Chem. Soc. Rev.**, [s. l.], v. 41, n. 7, p. 2656–2672, 2012.

LÉVESQUE, L. Law of cooling, heat conduction and Stefan-Boltzmann radiation laws fitted to experimental data for bones irradiated by CO2 laser. **Biomedical Optics Express**, [s. l.], v. 5, n. 3, p. 701, 2014.

LI, S. et al. Single Quantum Dots as Local Temperature Markers. **Nano Letters**, [s. l.], v. 7, n. 10, p. 3102–3105, 2007.

LI, X. et al. Nd3+ Sensitized Up/Down Converting Dual-Mode Nanomaterials for Efficient In-vitro and In-vivo Bioimaging Excited at 800 nm. **Scientific Reports**, [s. l.],

v. 3, n. 1, 2013. Disponível em: <http://www.nature.com/articles/srep03536>. Acesso em: 14 fev. 2018.

LIMBOURG, A. et al. Evaluation of postnatal arteriogenesis and angiogenesis in a mouse model of hind-limb ischemia. **Nature Protocols**, [s. l.], v. 4, n. 12, p. 1737–1748, 2009.

LUNDY, D. J. et al. Distribution of Systemically Administered Nanoparticles Reveals a Size-Dependent Effect Immediately following Cardiac Ischaemia-Reperfusion Injury. **Scientific Reports**, [s. l.], v. 6, n. 1, 2016. Disponível em: <http://www.nature.com/articles/srep25613>. Acesso em: 15 fev. 2018.

M., D. et al. Heat Generation and Transfer on Biological Tissues Due to High-Intensity Laser Irradiation. In: DOS SANTOS BERNARDES, M. A. (Ed.). **Developments in Heat Transfer**. [s.l.] : InTech, 2011.

MAESTRO, L. M. et al. Nanoparticles for highly efficient multiphoton fluorescence bioimaging. **Optics Express**, [s. l.], v. 18, n. 23, p. 23544, 2010. a.

MAESTRO, L. M. et al. CdSe Quantum Dots for Two-Photon Fluorescence Thermal Imaging. **Nano Letters**, [s. l.], v. 10, n. 12, p. 5109–5115, 2010. b.

MAESTRO, L. M. et al. Heating efficiency of multi-walled carbon nanotubes in the first and second biological windows. **Nanoscale**, [s. l.], v. 5, n. 17, p. 7882, 2013. a.

MAESTRO, L. M. et al. Fluorescent nanothermometers provide controlled plasmonic-mediated intracellular hyperthermia. **Nanomedicine**, [s. l.], v. 8, n. 3, p. 379–388, 2013. b.

MARCINIAK, Ł. et al. Near infrared absorbing near infrared emitting highly-sensitive luminescent nanothermometer based on $Nd^{3+}$ to $Yb^{3+}$ energy transfer. **Physical Chemistry Chemical Physics**, [s. l.], v. 17, n. 37, p. 24315–24321, 2015.

MARMOR, J. B. et al. Treatment of superficial human neoplasms by local hyperthermia induced by ultrasound. **Cancer**, [s. l.], v. 43, n. 1, p. 188–197, 1979.

MATSUMURA, Y.; MAEDA, H. A new concept for macromolecular therapeutics in cancer chemotherapy: mechanism of tumoritropic accumulation of proteins and the antitumor agent smancs. **Cancer Research**, [s. l.], v. 46, n. 12 Pt 1, p. 6387–6392, 1986.

MAURICE, E. et al. Erbium-doped silica fibers for intrinsic fiber-optic temperature sensors. **Applied Optics**, [s. l.], v. 34, n. 34, p. 8019, 1995.

MIKKELSEN, R.; WALLACH, D. Temperature sensitivity of the erythrocyte membrane potential as determined by cyanine dye fluorescence. **Cell Biology International Reports**, [s. l.], v. 1, n. 1, p. 51–55, 1977.

MIYAGAWA, T. et al. Glue-Free Stacked Luminescent Nanosheets Enable High-Resolution Ratiometric Temperature Mapping in Living Small Animals. **ACS Applied Materials & Interfaces**, [s. l.], v. 8, n. 49, p. 33377–33385, 2016.

MOON, H. K.; LEE, S. H.; CHOI, H. C. *In Vivo* Near-Infrared Mediated Tumor Destruction by Photothermal Effect of Carbon Nanotubes. **ACS Nano**, [s. l.], v. 3, n. 11, p. 3707–3713, 2009.

MORELLO, G. et al. Temperature and Size Dependence of Nonradiative Relaxation and Exciton−Phonon Coupling in Colloidal CdTe Quantum Dots. **The Journal of Physical Chemistry C**, [s. l.], v. 111, n. 16, p. 5846–5849, 2007.

MOTT, N. F. On the Absorption of Light by Crystals. **Proceedings of the Royal Society A: Mathematical, Physical and Engineering Sciences**, [s. l.], v. 167, n. 930, p. 384–391, 1938.

NG, E. Y.-K. A review of thermography as promising non-invasive detection modality for breast tumor. **International Journal of Thermal Sciences**, [s. l.], v. 48, n. 5, p. 849–859, 2009.

NIE, S. et al. Nanotechnology Applications in Cancer. **Annual Review of Biomedical Engineering**, [s. l.], v. 9, n. 1, p. 257–288, 2007.

NIIYAMA, H. et al. Murine Model of Hindlimb Ischemia. **Journal of Visualized Experiments**, [s. l.], n. 23, 2009. Disponível em: <http://www.jove.com/index/Details.stp?ID=1035>. Acesso em: 13 fev. 2018.

NYBORG, W. L. Solutions of the bio-heat transfer equation. **Physics in Medicine and Biology**, [s. l.], v. 33, n. 7, p. 785–792, 1988.

NYK, M. et al. High Contrast in Vitro and in Vivo Photoluminescence Bioimaging Using Near Infrared to Near Infrared Up-Conversion in $Tm^{3+}$ and $Yb^{3+}$ Doped Fluoride Nanophosphors. **Nano Letters**, [s. l.], v. 8, n. 11, p. 3834–3838, 2008.

OKABE, K. et al. Intracellular temperature mapping with a fluorescent polymeric thermometer and fluorescence lifetime imaging microscopy. **Nature Communications**, [s. l.], v. 3, n. 1, 2012. Disponível em: <http://www.nature.com/articles/ncomms1714>. Acesso em: 6 fev. 2018.

ORLOVSKII, Y. V. et al. Fluctuation kinetics of fluorescence hopping quenching in the Nd3+:Y2O3 spherical nanoparticles. **Journal of Luminescence**, [s. l.], v. 139, p. 91–97, 2013.

OSTROUMOV, V. et al. Study of luminescence concentration quenching and energy transfer upconversion in Nd-doped LaSc_3(BO_3)_4 and GdVO_4 laser crystals. **Journal of the Optical Society of America B**, [s. l.], v. 15, n. 3, p. 1052, 1998.

PANKHURST, Q. A. et al. Applications of magnetic nanoparticles in biomedicine. **Journal of Physics D: Applied Physics**, [s. l.], v. 36, n. 13, p. R167–R181, 2003.

PARAK, W. J. et al. Biological applications of colloidal nanocrystals. **Nanotechnology**, [s. l.], v. 14, n. 7, p. R15–R27, 2003.

PATEL, P. A. et al. A self-heated thermistor technique to measure effective thermal properties from the tissue surface. **Journal of Biomechanical Engineering**, [s. l.], v. 109, n. 4, p. 330–335, 1987.

PATTERSON, A. P.; BOOTH, S. A.; SABA, R. The Emerging Use of In Vivo Optical Imaging in the Study of Neurodegenerative Diseases. **BioMed Research International**, [s. l.], v. 2014, p. 1–14, 2014.

PAVEL, N. et al. In-band pumping of Nd-vanadate thin-disk lasers. **Applied Physics B**, [s. l.], v. 91, n. 3–4, p. 415–419, 2008.

PENG, H.-S.; HUANG, S.-H.; WOLFBEIS, O. S. Ratiometric fluorescent nanoparticles for sensing temperature. **Journal of Nanoparticle Research**, [s. l.], v. 12, n. 8, p. 2729–2733, 2010.

PENNES, H. H. Analysis of tissue and arterial blood temperatures in the resting human forearm. **Journal of Applied Physiology**, [s. l.], v. 1, n. 2, p. 93–122, 1948.

QUEK, C.-H.; LEONG, K. W. Near-Infrared Fluorescent Nanoprobes for in Vivo Optical Imaging. **Nanomaterials**, [s. l.], v. 2, n. 4, p. 92–112, 2012.

QUINTANILLA, M. et al. Energy transfer efficiency in $YF_3$ nanocrystals: Quantifying the $Yb^{3+}$ to $Tm^{3+}$ infrared dynamics. **Journal of Applied Physics**, [s. l.], v. 113, n. 17, p. 174308, 2013.

REN, F. et al. Microwave-assisted cation exchange toward synthesis of near-infrared emitting PbS/CdS core/shell quantum dots with significantly improved quantum yields through a uniform growth path. **Nanoscale**, [s. l.], v. 5, n. 17, p. 7800, 2013.

ROBINSON, J. T. et al. In Vivo Fluorescence Imaging in the Second Near-Infrared Window with Long Circulating Carbon Nanotubes Capable of Ultrahigh Tumor Uptake. **Journal of the American Chemical Society**, [s. l.], v. 134, n. 25, p. 10664–10669, 2012.

ROCHA, U. et al. Subtissue Thermal Sensing Based on Neodymium-Doped $LaF_3$ Nanoparticles. **ACS Nano**, [s. l.], v. 7, n. 2, p. 1188–1199, 2013.

ROCHA, U. et al. $Nd^{3+}$ doped $LaF_3$ nanoparticles as self-monitored photo-thermal agents. **Applied Physics Letters**, [s. l.], v. 104, n. 5, p. 053703, 2014. a.

ROCHA, U. et al. Neodymium-Doped $LaF_3$ Nanoparticles for Fluorescence Bioimaging in the Second Biological Window. **Small**, [s. l.], v. 10, n. 6, p. 1141–1154, 2014. b.

ROTMAN, S. R. Analysis of neodymium-to-erbium energy transfer in yttrium aluminum garnet with a nonuniform-distribution model. **Optics Letters**, [s. l.], v. 15, n. 4, p. 230, 1990.

RUSCHKEWITZ, Y.; GEFEN, A. Cell-level temperature distributions in skeletal muscle post spinal cord injury as related to deep tissue injury. **Medical & Biological Engineering & Computing**, [s. l.], v. 48, n. 2, p. 113–122, 2010.

SACCOMANDI, P.; SCHENA, E.; SILVESTRI, S. Techniques for temperature monitoring during laser-induced thermotherapy: An overview. **International Journal of Hyperthermia**, [s. l.], v. 29, n. 7, p. 609–619, 2013.

SAÏDI, E. et al. Scanning thermal imaging by near-field fluorescence spectroscopy. **Nanotechnology**, [s. l.], v. 20, n. 11, p. 115703, 2009.

SAJI, V. S.; CHOE, H. C.; YEUNG, K. W. K. Nanotechnology in biomedical applications: a review. **International Journal of Nano and Biomaterials**, [s. l.], v. 3, n. 2, p. 119–139, 2010.

SALATA, O. V. Applications of nanoparticles in biology and medicine. **Journal of Nanobiotechnology**, [s. l.], v. 2, n. 1, p. 3, 2004.

SAVCHUK, O. A. et al. Er:Yb:$NaY_2F_5O$ up-converting nanoparticles for sub-tissue fluorescence lifetime thermal sensing. **Nanoscale**, [s. l.], v. 6, n. 16, p. 9727, 2014.

SAVCHUK, O. A. et al. Ho,Yb:KLu(WO $_4$ ) $_2$ Nanoparticles: A Versatile Material for Multiple Thermal Sensing Purposes by Luminescent Thermometry. **The Journal of Physical Chemistry C**, [s. l.], v. 119, n. 32, p. 18546–18558, 2015.

SEDLMEIER, A. et al. Photon upconverting nanoparticles for luminescent sensing of temperature. **Nanoscale**, [s. l.], v. 4, n. 22, p. 7090, 2012.

SEITZ, F. An interpretation of crystal luminescence. **Transactions of the Faraday Society**, [s. l.], v. 35, p. 74, 1939.

SHAH, N. et al. Noninvasive functional optical spectroscopy of human breast tissue. **Proceedings of the National Academy of Sciences**, [s. l.], v. 98, n. 8, p. 4420–4425, 2001.

SHAN GUAN, S. G. et al. Spectroscopic properties and energy transfer processes in Er3+/Nd3+ co-doped tellurite glass for 2.7-\mu m laser materials. **Chinese Optics Letters**, [s. l.], v. 10, n. 7, p. 071603-71607, 2012.

SHEN, S. et al. Targeting mesoporous silica-encapsulated gold nanorods for chemo-photothermal therapy with near-infrared radiation. **Biomaterials**, [s. l.], v. 34, n. 12, p. 3150–3158, 2013.

SIDIROGLOU, F. et al. Effects of high-temperature heat treatment on Nd3+-doped optical fibers for use in fluorescence intensity ratio based temperature sensing. **Review of Scientific Instruments**, [s. l.], v. 74, n. 7, p. 3524–3530, 2003.

SINGH, S. K.; KUMAR, K.; RAI, S. B. Er3+/Yb3+ codoped Gd2O3 nano-phosphor for optical thermometry. **Sensors and Actuators A: Physical**, [s. l.], v. 149, n. 1, p. 16–20, 2009.

SKRIPKA, A. et al. Double rare-earth nanothermometer in aqueous media: opening the third optical transparency window to temperature sensing. **Nanoscale**, [s. l.], v. 9, n. 9, p. 3079–3085, 2017.

SMITH, A. M.; MANCINI, M. C.; NIE, S. Second window for in vivo imaging: Bioimaging. **Nature Nanotechnology**, [s. l.], v. 4, n. 11, p. 710–711, 2009.

SORDILLO, L. A. et al. Deep optical imaging of tissue using the second and third near-infrared spectral windows. **Journal of Biomedical Optics**, [s. l.], v. 19, n. 5, p. 056004, 2014.

STALDER, M.; BASS, M.; CHAI, B. H. T. Thermal quenching of fluorescence in chromium-doped fluoride laser crystals. **Journal of the Optical Society of America B**, [s. l.], v. 9, n. 12, p. 2271, 1992.

STOUWDAM, J. W.; VAN VEGGEL, F. C. J. M. Near-infrared Emission of Redispersible $Er^{3+}$, $Nd^{3+}$, and $Ho^{3+}$ Doped $LaF_3$ Nanoparticles. **Nano Letters**, [s. l.], v. 2, n. 7, p. 733–737, 2002.

TAKAHASHI, I. et al. Clinical application of hyperthermia combined with anticancer drugs for the treatment of solid tumors. **Surgery**, [s. l.], v. 131, n. 1 Suppl, p. S78-84, 2002.

TOUTOUZAS, K. et al. Inflammation in lone atrial fibrillation: New insights by coronary sinus thermography. **International Journal of Cardiology**, [s. l.], v. 134, n. 3, p. 345–350, 2009.

TROMBERG, B. J. et al. Non-invasive measurements of breast tissue optical properties using frequency-domain photon migration. **Philosophical Transactions of the Royal Society B: Biological Sciences**, [s. l.], v. 352, n. 1354, p. 661–668, 1997.

TU, D. et al. Time-Resolved FRET Biosensor Based on Amine-Functionalized Lanthanide-Doped NaYF4 Nanocrystals. **Angewandte Chemie International Edition**, [s. l.], v. 50, n. 28, p. 6306–6310, 2011.

VALERINI, D. et al. Temperature dependence of the photoluminescence properties of colloidal Cd Se ⁄ Zn S core/shell quantum dots embedded in a polystyrene matrix. **Physical Review B**, [s. l.], v. 71, n. 23, 2005. Disponível em: <https://link.aps.org/doi/10.1103/PhysRevB.71.235409>. Acesso em: 9 fev. 2018.

VALVANO, J. W.; COCHRAN, J. R.; DILLER, K. R. Thermal conductivity and diffusivity of biomaterials measured with self-heated thermistors. **International Journal of Thermophysics**, [s. l.], v. 6, n. 3, p. 301–311, 1985.

VAN VEGGEL, F. C. J. M. Near-Infrared Quantum Dots and Their Delicate Synthesis, Challenging Characterization, and Exciting Potential Applications. **Chemistry of Materials**, [s. l.], v. 26, n. 1, p. 111–122, 2014.

VETRONE, F. et al. The Active-Core/Active-Shell Approach: A Strategy to Enhance the Upconversion Luminescence in Lanthanide-Doped Nanoparticles. **Advanced Functional Materials**, [s. l.], v. 19, n. 18, p. 2924–2929, 2009.

VETRONE, F. et al. Intracellular imaging of HeLa cells by non-functionalized NaYF4 : Er $^{3+}$ , Yb $^{3+}$ upconverting nanoparticles. **Nanoscale**, [s. l.], v. 2, n. 4, p. 495–498, 2010. a.

VETRONE, F. et al. Temperature Sensing Using Fluorescent Nanothermometers. **ACS Nano**, [s. l.], v. 4, n. 6, p. 3254–3258, 2010. b.

VILLA, I. et al. 1.3 μm emitting SrF2:Nd3+ nanoparticles for high contrast in vivo imaging in the second biological window. **Nano Research**, [s. l.], v. 8, n. 2, p. 649–665, 2015.

WALKER, G. W. et al. Quantum-dot optical temperature probes. **Applied Physics Letters**, [s. l.], v. 83, n. 17, p. 3555–3557, 2003.

WANG, F. et al. Tuning upconversion through energy migration in core–shell nanoparticles. **Nature Materials**, [s. l.], v. 10, n. 12, p. 968–973, 2011.

WANG, F. et al. Experimental study of the scintillation index of a radially polarized beam with controllable spatial coherence. **Applied Physics Letters**, [s. l.], v. 103, n. 9, p. 091102, 2013. a.

WANG, F.; LIU, X. Upconversion Multicolor Fine-Tuning: Visible to Near-Infrared Emission from Lanthanide-Doped $NaYF_4$ Nanoparticles. **Journal of the American Chemical Society**, [s. l.], v. 130, n. 17, p. 5642–5643, 2008.

WANG, X.; WOLFBEIS, O. S.; MEIER, R. J. Luminescent probes and sensors for temperature. **Chemical Society Reviews**, [s. l.], v. 42, n. 19, p. 7834, 2013.

WANG, Y.-F. et al. $Nd^{3+}$ -Sensitized Upconversion Nanophosphors: Efficient *In Vivo* Bioimaging Probes with Minimized Heating Effect. **ACS Nano**, [s. l.], v. 7, n. 8, p. 7200–7206, 2013. b.

WAWRZYNCZYK, D. et al. Neodymium(iii) doped fluoride nanoparticles as non-contact optical temperature sensors. **Nanoscale**, [s. l.], v. 4, n. 22, p. 6959, 2012.

WEBER, M. J. Optical Properties of Yb 3 + and Nd 3 + - Yb 3 + Energy Transfer in YAl O 3. **Physical Review B**, [s. l.], v. 4, n. 9, p. 3153–3159, 1971.

WEISSLEDER, R. A clearer vision for in vivo imaging. **Nature Biotechnology**, [s. l.], v. 19, n. 4, p. 316–317, 2001.

WEISSLEDER, R.; PITTET, M. J. Imaging in the era of molecular oncology. **Nature**, [s. l.], v. 452, n. 7187, p. 580–589, 2008.

WELCH, A. J.; GEMERT, M. J. Van (EDS.). **Optical-thermal response of laser-irradiated tissue**. 2. ed ed. Dordrecht: Springer, 2011.

WELSHER, K.; SHERLOCK, S. P.; DAI, H. Deep-tissue anatomical imaging of mice using carbon nanotube fluorophores in the second near-infrared window. **Proceedings of the National Academy of Sciences**, [s. l.], v. 108, n. 22, p. 8943–8948, 2011.

WEN, H. et al. Upconverting Near-Infrared Light through Energy Management in Core-Shell-Shell Nanoparticles. **Angewandte Chemie International Edition**, [s. l.], v. 52, n. 50, p. 13419–13423, 2013.

XIE, X. et al. Mechanistic Investigation of Photon Upconversion in $Nd^{3+}$ -Sensitized Core–Shell Nanoparticles. **Journal of the American Chemical Society**, [s. l.], v. 135, n. 34, p. 12608–12611, 2013.

XIMENDES, E. C. et al. Self-monitored photothermal nanoparticles based on core–shell engineering. **Nanoscale**, [s. l.], v. 8, n. 5, p. 3057–3066, 2016. a.

XIMENDES, E. C. et al. Unveiling in Vivo Subcutaneous Thermal Dynamics by Infrared Luminescent Nanothermometers. **Nano Letters**, [s. l.], v. 16, n. 3, p. 1695–1703, 2016. b.

XIMENDES, E. C. et al. $LaF_3$ core/shell nanoparticles for subcutaneous heating and thermal sensing in the second biological-window. **Applied Physics Letters**, [s. l.], v. 108, n. 25, p. 253103, 2016. c.

XIMENDES, E. C. et al. In Vivo Ischemia Detection by Luminescent Nanothermometers. **Advanced Healthcare Materials**, [s. l.], v. 6, n. 4, p. 1601195, 2017. a.

XIMENDES, E. C. et al. In Vivo Subcutaneous Thermal Video Recording by Supersensitive Infrared Nanothermometers. **Advanced Functional Materials**, [s. l.], v. 27, n. 38, p. 1702249, 2017. b.

YANG, J.-M.; YANG, H.; LIN, L. Quantum Dot Nano Thermometers Reveal Heterogeneous Local Thermogenesis in Living Cells. **ACS Nano**, [s. l.], v. 5, n. 6, p. 5067–5071, 2011.

YANG, W. et al. Effect of carrier emission and retrapping on luminescence time decays in InAs/GaAs quantum dots. **Physical Review B**, [s. l.], v. 56, n. 20, p. 13314–13320, 1997.

ZACCAGNINI, G. et al. Magnetic Resonance Imaging Allows the Evaluation of Tissue Damage and Regeneration in a Mouse Model of Critical Limb Ischemia. **PLOS ONE**, [s. l.], v. 10, n. 11, p. e0142111, 2015.

ZHAN, Q. et al. Using 915 nm Laser Excited Tm $^{3+}$ /Er $^{3+}$ /Ho $^{3+}$ -Doped NaYbF4 Upconversion Nanoparticles for *in Vitro* and Deeper *in Vivo* Bioimaging without Overheating Irradiation. **ACS Nano**, [s. l.], v. 5, n. 5, p. 3744–3757, 2011.

ZHANG, X. et al. Influence of neodymium-doping on structure and properties of yttrium aluminium garnet. **CrystEngComm**, [s. l.], v. 15, n. 39, p. 8029, 2013.

ZHANG, Y. et al. Ag $_2$ S Quantum Dot: A Bright and Biocompatible Fluorescent Nanoprobe in the Second Near-Infrared Window. **ACS Nano**, [s. l.], v. 6, n. 5, p. 3695–3702, 2012.

ZHAO, Y. et al. High-Temperature Luminescence Quenching of Colloidal Quantum Dots. **ACS Nano**, [s. l.], v. 6, n. 10, p. 9058–9067, 2012.

ZHAO, Y. et al. Optically investigating Nd^3+-Yb^3+ cascade sensitized upconversion nanoparticles for high resolution, rapid scanning, deep and damage-free bio-imaging. **Biomedical Optics Express**, [s. l.], v. 6, n. 3, p. 838, 2015.

ZHOU, H. S. et al. Coated Semiconductor Nanoparticles: The CdS/PbS System's Photoluminescence Properties. **Chemistry of Materials**, [s. l.], v. 6, n. 9, p. 1534–1541, 1994.

ZHUANG, X. et al. Enhanced emission of 2.7μm from Er3+/Nd3+-codoped LiYF4 single crystals. **Materials Science and Engineering: B**, [s. l.], v. 178, n. 5, p. 326–329, 2013.

ZOHAR, O. et al. Thermal Imaging of Receptor-Activated Heat Production in Single Cells. **Biophysical Journal**, [s. l.], v. 74, n. 1, p. 82–89, 1998.

# Appendices

**Appendix 1 - Thermal dynamics of subcutaneous tissue in the presence of a multimode laser fiber**

The equation describing heating and cooling processes of a biological system is the so-called Penne's bioheat equation. In cylindrical coordinates this equation can be written as:

$$\frac{\partial T(r,z,t)}{\partial t} = D\nabla^2 T(r,z,t) - \ b\,T(r,z,t) + \frac{1}{\rho c} S(r,z,t)$$

(S1)

where the first and the second terms on the right-hand side are due to thermal diffusion and blood flow, respectively. S(r,z,t) is the power deposited per unit volume due to the absorption of the laser energy and T(r,z,t) is the temperature above the baseline temperature of the tissue. The thermal diffusivity $D$ is equal to $k/\rho c$, where $k$, $\rho$ and $c$ are thermal conductivity, density and specific heat of the tissue, respectively.

Since in the experiments of Section 5.3, the injection depth was estimated to be low enough so that we could consider the NPs as being present in the epidermis where blood flow was expected to be minimal, then the parameter b was neglected. The Green function for Eq. S1 is then written as:

$$G(r,z,t,r',z',t') = \frac{r'\Theta(t-t')}{\sqrt{2\pi}\rho c[2D(t-t')]^{\frac{3}{2}}} e^{-\frac{(z-z')^2}{4D(t-t')}} e^{-\frac{r'^2+r^2}{4D(t-t')}} I_o\left(\frac{rr'}{2D(t-t')}\right)$$

(S2)

where $\Theta(t-t')$ is the Heaviside function defined as1 if $t > t'$and 0 otherwise. $I_o$ is the modified Bessel function of order zero. The solution of Eq. S1 can be written as:

$$T(r,z,t) = \int_0^{\infty} \int_{-\infty}^{\infty} \int_{-\infty}^{\infty} G(r,z,t,r',z',t') S(r',z',t') r' dr' dz' dt'$$

(S3)

In order to simulate the heat contribution of a multimode laser fiber to the system, the heat source term, S(r,z,t), was expressed as decaying exponentially in the z direction, according to the following expression:

$$S(z,t) = \begin{cases} \dfrac{2\alpha E_o}{\pi a^2 t_o} \Theta(a-r) e^{-\alpha z}, for\ z \geq 0\ and\ 0 \leq t \leq t_o \\ 0, \qquad\qquad otherwise \end{cases}$$

(S4)

Here, $a$ is the radius of the laser beam, $E_o$ is the total energy of the heating pulse, $\alpha$ is the absorption coefficient of the tissue and $t_o$ is the pulse duration. Inserting S4 into S3, one obtains:

$$T(r,z,t) = C \int_0^{Min[t,t_o]} \left[ \int_0^{a} e^{-\frac{r'^2 + r^2}{4D(t-t')}} I_o\left(\frac{rr'}{2D(t-t')}\right) r'^2 dr' \right] \times$$

$$\frac{e^{-\alpha z + \alpha^2 D(t-t')}}{D(t-t')} Erfc\left(\frac{2D\alpha(t-t') - z}{\sqrt{4D(t-t')}}\right) dt'$$

(S5)

with $C = \alpha E_o / 2\pi a^2 t_o \rho c$. Thus, if one intends to study the temperature profile during the heating pulse, the proper expression is:

$$T(r,z,t) = C \int_0^{t} \left[ \int_0^{a} e^{-\frac{r'^2 + r^2}{4D(t-t')}} I_o\left(\frac{rr'}{2D(t-t')}\right) r'^2 dr' \right] \times$$

$$\frac{e^{-\alpha z + \alpha^2 D(t-t')}}{D(t-t')} Erfc\left(\frac{2D\alpha(t-t') - z}{\sqrt{4D(t-t')}}\right) dt'$$

(S6)

If, however, one intends to study the cooling process after the heating pulse, the temperature profile is written as:

$$T(r,z,t) = C\int_0^{t_o}\left[\int_0^a e^{-\frac{r'^2+r^2}{4D(t+t_o-t')}} I_o\left(\frac{rr'}{2D(t+t_o-t')}\right) r'^2 dr'\right]\times$$

$$\frac{e^{-\alpha z+\alpha^2 D(t+t_o-t')}}{D(t+t_o-t')} Erfc\left(\frac{2D\alpha(t+t_o-t')-z}{\sqrt{4D(t+t_o-t')}}\right)dt'$$

(S7)

**Appendix 2 – Heat conduction in a composite biomaterial with perfusion**

The one-dimensional problem of conduction of heat into a tissue with blood perfusion can be described by the well-known Penne's bioheat equation:

$$\rho c\frac{\partial T}{\partial t} = \frac{\partial}{\partial x}\left(k\frac{\partial T}{\partial x}\right) - \rho_b c_b \omega(T - T_a) + q$$

(S8)

where $\rho$, $c$, k are the density, specific heat and thermal conductivity of the tissue, $\omega$ the is the local blood perfusion rate and $q$ is the local metabolic heat generation rate. $T_a$ and $T$ are the blood and tissue temperatures, respectively.

This appendix describes the solution to S8 corresponding to the system depicted in Figure S1 where a number of 4 composite layers is presented. Each layer has its own physical properties and, as a consequence, the parameters of equation S8 may experience a discontinuity at the interfaces. The top surface of the first layer (epidermis) is exchanging thermal energy by convection with a flow field ($h_o$) whose ambient temperature is $T_o$. On the other hand, the interface between muscle and bone (bottom of layer 4) is assumed to be at constant core body temperature, $T_{core}$.[1, 2] Additionally, both temperature and heat flux are required to be continuous throughout the tissue.

**Supplementary Figure S1 –** Composite system representation of the perfuse tissue slab

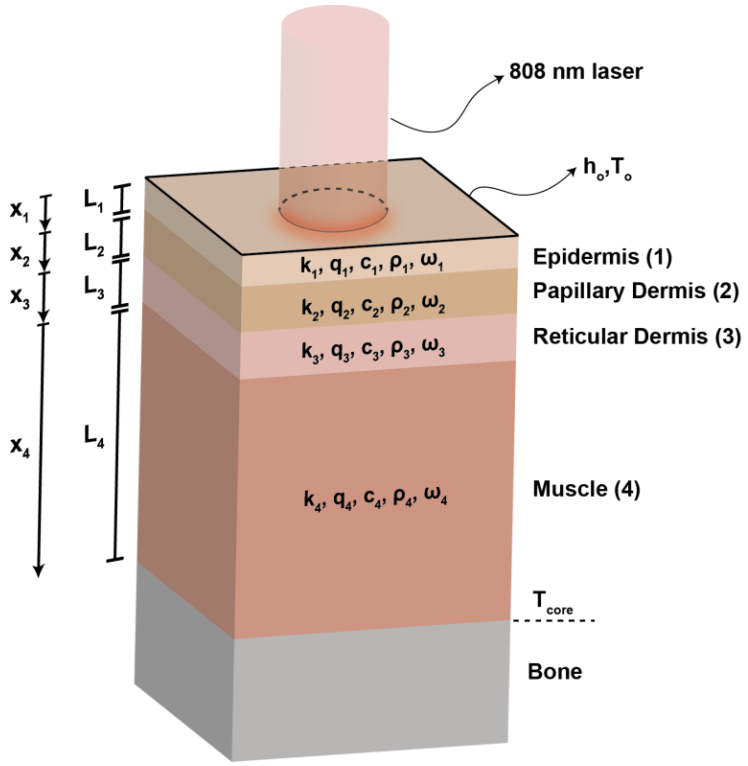


For the sake of simplicity, equation S8 will be put in a dimensionless form – a common approach recently used in works dealing with the bioheat equation.[3] In order to acomplish that, the spatial domain of the system will be discretized in such a way that each layer will have an associated spatial coordinate that is normalized by its own length (*i.e.*, $z_i = x_i/L_i$). Thus, the interface positions may be identified by the coordinates $z_{i-1} = 1$ and $z_i = 0$. The time variable will be scaled by an arbitrary time constant ($\tau = t/t_o$). Finally, the temperatures of each layer will be described by $\theta_i = (T_i - T_a)/(T_o - T_{core})$. Thus, equation S8 becomes:

$$\frac{1}{\delta_i}\frac{\partial \theta_i}{\partial \tau} + m_i^2\theta_i - \phi_i = \frac{\partial^2 \theta_i}{\partial z_i^2} \qquad \text{(S9)}$$

where $m_i^2 = (\rho_b c_b \omega L^2/k)_i$, $\delta_i = t_o(k_i/\rho_i c_i L_i^2)$ and $\phi_i = q_i L_i^2/(T_o - T_L)/k_i$ are the dimensionless terms corresponding to perfusion, the constant Fourier number and the volumetric energy source, respectively.

As it was mentioned, the top face of the first layer ($z_1 = 0$) is exposed to convection heat transfer. Therefore, the skin boundary condition is represented as:

$$\frac{\partial \theta_1}{\partial z_1}_{\{z_1=0\}} = H_o(\theta_1(0,\tau) - \Delta\theta_o) \tag{S10}$$

where $H_o = h_o L_1/k_1$ and $\Delta\theta_o = (T_o - T_a)/(T_o - T_{core})$. On the other hand, the outer end of the last layer is assumed to be at constant body temperature. Thus:

$$\theta_4(1,\tau) = \Delta\theta_L \tag{S11}$$

where $\Delta\theta_L = (T_{core} - T_a)/(T_o - T_{core})$. The requirement of continuous temperature and heat flux imposes (for i = 2, 3, 4):

$$K_i \frac{\partial \theta_i}{\partial z_i}_{\{z_i=0\}} = K_{i-1} \frac{\partial \theta_{i-1}}{\partial z_{i-1}}_{\{z_{i-1}=1\}} \tag{S12}$$

$$\theta_i(0,\tau) = \theta_{i-1}(1,\tau) \tag{S13}$$

where $K_i = k_i/L_i$. Lastly, at $\tau = 0$ the system has some spatially dependent temperature distribution:

$$\theta_i(z_i,0) = F(z_i) \tag{S14}$$

**S2.1 – Separation of variables**

We can suitably construct a solution consisting of a non-homogeneous steady spatially dependent component $\Psi_i(z_i)$ and a position and time dependent homogeneous component $\Theta_i(z_i,\tau)$:[4]

$$\theta_i(z_i,\tau) = \Psi_i(z_i) - \Theta_i(z_i,\tau) \tag{S15}$$

In order to make the governing equation and the boundary conditions homogeneous for the $\Theta_i(z_i,\tau)$ component, we impose that $\Psi_i(z_i)$ satisfies the non-homogeneous components of equations S10–S14:

$$m_i^2\Psi_i - \phi_i = \Psi_i{}'' \tag{16a}$$

$$\Psi_1{}'(0) = H_o(\Psi_1(0) - \Delta\theta_o) \tag{S16b}$$

$$\Psi_{\mathrm{N}}(1) = \Delta\theta_L \tag{S16c}$$

$$K_i\Psi_i'(0) = K_{i-1}\,\Psi_{i-1}'(1) \tag{S16d}$$

$$\Psi_1(0) = \Psi_{i-1}(1)\ \forall\ i = \{2, \dots, N\} \tag{S16e}$$

This, in turns, enables the separation of variables of $\Theta_i(z_i, \tau) = Z_i(z_i) \times \Gamma_i(\tau)$. Thus, substituting equation (S8) in equations S10-S15, we find:7

$$\frac{1}{\delta_i}\frac{\Gamma_i'(\tau)}{\Gamma_i(\tau)} + m_i^2 = \frac{Z_i''(z_i)}{Z_i(z_i)} = -\mu_i^2 \tag{S17a}$$

$$Z_1'(0) = H_o Z_1(0) \tag{S17b}$$

$$Z_N(1)\Gamma(\tau) = 0 \tag{S17c}$$

$$K_i Z_i'(0)\Gamma_i(\tau) = K_{i-1}Z_{i-1}'(1)\Gamma_{i-1}(\tau) \tag{S17d}$$

$$Z_i(0)\Gamma_i(\tau) = Z_{i-1}(1)\Gamma_{i-1}(\tau) \tag{S17e}$$

$$Z_i(z_i)\Gamma_i(0) = \Psi_i(z_i) - F_i(x_i) \tag{S17f}$$

where $\mu_i$ is the eigenvalue associated with the i-th layer. The quantity $\mu_i^2 + m_i^2$ is anticipated to be a positive real number so that the transient component solutions are of the form:

$$\Gamma_i(\tau) = exp\left(-\delta_i\left(\mu_i^2 + m_i^2\right)\tau\right) \tag{S18a}$$

$$Z_i(z_i) = a_i \sin(\mu_i x_i) + b_i \cos(\mu_i x_i) \tag{S18a}$$

where $a_i$ and $b_i$ are integration constants.

**S2. 2 – Algorithmic relations**

A similar problem containing the conditions described by Equations S10a, S10b, S10d, S10e and S10f was investigated by Becker et al. Therefore, we can

straightforwardly use the algorithmic relations found by the authors when using those boundary conditions: [3]

$$\mu_i = \sqrt{\frac{\delta_R}{\delta_i}(\mu_R^2 + m_R^2) - m_i^2} \tag{S19a}$$

$$b_1 = \frac{\mu_1}{H_o} a_1 \tag{S19b}$$

$$Z_1(z_1) = \sin(\mu_1 z_1) + \frac{\mu_1}{H_o}\cos(\mu_1 z_1) \tag{S19c}$$

$$Z_1'(z_1) = \mu_1 \left(\cos(\mu_1 z_1) - \frac{\mu_1}{H_o}\sin(\mu_1 z_1)\right) \tag{S19d}$$

$$Z_i(z_i) = \frac{K_{i-1}}{K_i}\frac{Z_{i-1}'(1)}{\mu_i}\sin(\mu_i z_i) + Z_{i-1}(1)\cos(\mu_i z_i) \tag{S19e}$$

$$Z_i'(z_i) = \frac{K_{i-1}}{K_i} Z_{i-1}'(1)\cos(\mu_i z_i) - \mu_i\, Z_{i-1}(1)\sin(\mu_i z_i) \tag{S19f}$$

In turn, equation S10c results in:

$$Z_N(1) = 0 \tag{S19g}$$

where $\mu_R$ and $m_R$ indicates the eigenvalue and the dimensionless perfusion parameter of the reference layer - defined as the one having the minimum value of $\delta_i m_i^2$ (in the present case, the epidermis).[3]

**S2.3 – The exponential function as an approximate solution of the bioheat equation**

The values of $\mu_R$ can be obtained through equation S19g. At this point it is important to note that $\mu_R$ depends on the thermal properties of all layers. As expected, this equation has an infinite number of distinct real roots due to the trigonometric nature of the $Z_i$ functions. Therefore, the solution can be written as:

$$\theta_i(z_i, \tau) = \Psi_i(z_i) - \sum_{n=1}^{\infty} C_n Z_{i,n}(z_i) \times \exp\left(-\delta_R\left(\mu_{R,n}^2 + m_R^2\right)\tau\right) \tag{S20}$$

However, for the sake of simplicity, we will suitably consider only one of the possible eigenvalues of equation S19g - specifically, the one with the highest weighting factor, $C_n$ - and write the solution as a single exponential instead of an infinite series. Therefore:

$$\theta_i(z_i,\tau) = \Psi_i(z_i) - CZ_i(z_i) \times \exp(-\delta_R(\mu_R^2 + m_R^2)\tau) \tag{S21}$$

Using the definition of $\theta_i$, the temperature in the i-th layer can then be expressed as:

$$T_i(z_i,\tau) = T_a + (T_o - T_{core})\Psi_i(z_i) + \\ -(T_o - T_{core})\, CZ_i(z_i) \times \exp(-\delta_R(\mu_R^2 + m_R^2)\tau) \tag{S22}$$

From which the exponential time decay is straightforwardly obtained:

$$\frac{T_i(z_i,t) - T_i(z_i,\infty)}{T_i(z_i,0) - T_i(z_i,\infty)} = \exp\left(-\frac{\delta_R(\mu_R^2 + m_R^2)}{t_o}t\right) = \exp\left(-\frac{\mathrm{t}}{\tau_{\mathrm{eff}}}\right) \tag{S23}$$

where $\tau_{eff} = L_R^2/4\alpha_{eff}$ and $\alpha_{eff} = (k_R\mu_R^2 + \rho_b c_b \omega_R L_R^2)/4\rho_R c_R$ are the characteristic thermal relaxation time and effective thermal diffusivity of the system, respectively.

**S2.4 – $\tau_{eff}$ and thermal properties of tissue layers**

In order to study the dependence of $\tau_{eff}$ on the thermal properties of tissue layers, one must use the S19 algorithmic relations and investigate how the eigenvalues $\mu_{R,n}$ vary with them. To fulfill that task, the values contained in Table S1, characteristic of biological tissues, were used:

**Table S1 –** Thermal parameters according to the literature

| Tissue layer | $L$ ($10^{-3}$m) | $k$ (W.m$^{-1}$ K$^{-1}$) | $\rho$ (kg.m$^{-3}$) | $c$ (J kg$^{-1}$ K$^{-1}$) | $\omega_b$ ($10^{-3}$s$^{-1}$) | $m$ | $\delta$ |
|---|---|---|---|---|---|---|---|
| Epidermis | 0.46 | 0.235 | 1110 | 3589 | 0 | 0 | 0.2788 |
| Pap. Dermis | 1.67 | 0.445 | 1116 | 3300 | 0.2 | 0.0045 | 0.0433 |
| Ret. Dermis | 1.67 | 0.445 | 1116 | 3300 | 2.8 | 0.0632 | 0.0433 |
| Muscle | 5 | 0.51 | 1038 | 3800 | 6.5 | 1.1471 | 0.0052 |

**Supplementary Figure S2.- (a)** Dependence of thermal relaxation time on muscle perfusion as obtained by calculating the eigenvalues of equation S19g. $\omega_{max}$ corresponds to the maximum value of muscle perfusion (*i.e.*, the one provided in Table S1) while $\tau_{\omega max}$ correspond to thermal relaxation time obtained with $\omega_{muscle} = \omega_{max}$. **(b)** Thermal relaxation profile of a mouse's leg before (τ = 193 s) and after (τ = 212 s) surgery.

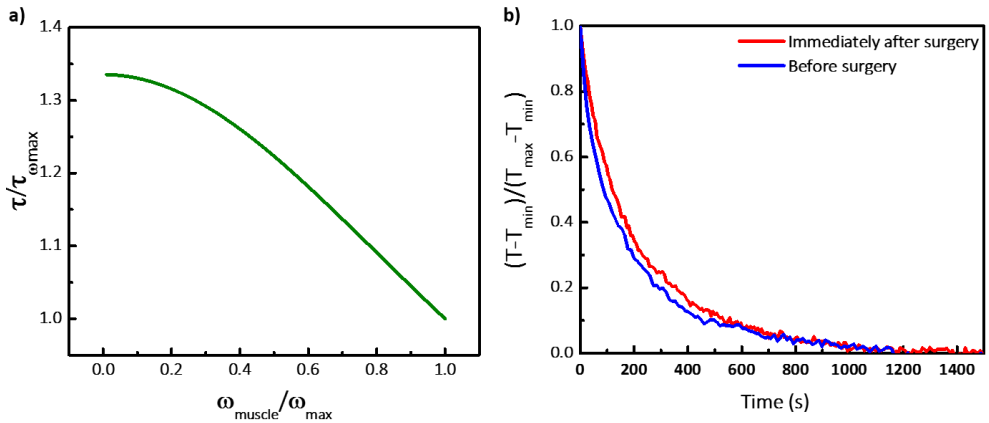

The effect caused in the thermal relaxation dynamics by the absence of blood flow was investigated by gradually reducing the value of $\omega_b$, corresponding to the muscle layer, to zero. Data included in **Figure S2 (a)** conclude that a simple reduction in blood flow can only produce an increment in the thermal relaxation time. This is, in fact, not only in good accordance with what was experimentally observed **(Figure S2 b)**, but to previous studies as well, which described how the thermal diffusivity of tissues and organs increases with blood perfusion. The leg's immediate response is opposite to the one observed on the following days after surgery. Therefore, one needs to consider the resulting consequences of ischemia – namely, the reduction in metabolic activity and nutrients (including water) supply – as the main reason for the posterior response.

**Supplementary Figure S3.** Dependence of thermal relaxation time on muscle size as obtained by calculating the eigenvalues of equation S19g.

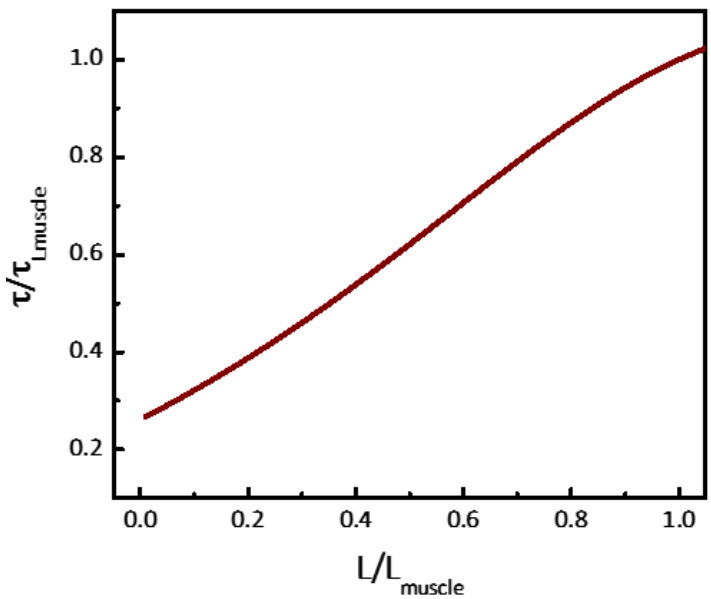


As a matter of fact, literature reports on damage of muscle as a resulting effect of ischemia. This is, in turns, reflected in a decrease in the muscle size (atrophy). Therefore, in order to investigate the dependence of the thermal relaxation dynamics on the muscle damage, one needs to gradually reduce the length of the

muscle layer, while imposing a reduced value for $\omega_b$ in the muscle layer, and to observe how $\tau_{eff}$ varies with it. From data included in Figure S3, it is evident that a reduction in the muscle size produces a decrement in the thermal relaxation time.

Even though the numerical analysis presupposes that the other layers – epidermis, reticular dermis and papillary dermis – are not directly altered by the surgery (i.e., their thermal properties do not change), the principles presented herein remain valid.

**Appendix 3 – Energy transfer processes in $Er^{3+}/Nd^{3+}$ co-doped materials**

The physical mechanism describing the visible and infrared emissions of $Er^{3}+/Nd^{3+}$ co-doped materials can be summarized as shown in Figure S4. $Er^{3+}$ ions were first excited from the ground state to the $^4I_{9/2}$ level by an 808 nm laser. Meanwhile, $Nd^{3+}$ ions were excited directly to the $^4F_{5/2}$ and $^2H_{9/2}$ levels. On one hand, a part of the excited $Nd^{3+}$ ions relaxed non-radiatively to the $^4F_{3/2}$ level. On the other hand, $Nd^{3+}$ ions in the $^4F_{5/2}$, $^2H_{9/2}$ and $^4F_{3/2}$ levels transferred their energy to $Er^{3+}$:$^4I_{9/2}$ and $^4I_{11/2}$ via the processes ($Nd^{3+}$:$^4F_{5/2}$, $^2H_{9/2}$ + $Er^{3+}$:$^4I_{15/2}$) → ($Nd^{3+}$:$^4I_{9/2}$ + $Er^{3+}$:$^4I_{9/2}$), ($Nd^{3+}$:$^4F_{5/2}$, $^2H_{9/2}$ + $Er^{3+}$:$^4I_{15/2}$) → ($Nd^{3+}$:$^4I_{9/2}$ + $Er^{3+}$:$^4I_{11/2}$), and ($Nd^{3+}$:$^4F_{3/2}$ + $Er^{3+}$:$^4I_{15/2}$) → ($Nd^{3+}$:$^4I_{9/2}$ + $Er^{3+}$:$^4I_{11/2}$). These energy transfer processes increase the population of $Er^{3+}$:$^4I_{11/2}$, which leads to enhanced 2.7 μm emission corresponding to $^4I_{11/2}$ → $^4I_{13/2}$. As a result, the increasing population of $Er^{3+}$:$^4I_{13/2}$ could lead to an increasing 550 nm up-conversion and 1.5 μm emission. However, an obvious decrease is observed in the 550 nm and 1.5 μm emissions, which may be due to the presence of energy transfer channels such as the following: ($Er^{3+}$:$^4I_{13/2}$ + $Nd^{3+}$:$^4I_{9/2}$) → ($Er^{3+}$:$^4I_{15/2}$ + $Nd^{3+}$:$^4I_{15/2}$) or ($Er^{3+}$:$^4I_{13/2}$ +$Nd^{3+}$:$^4I_{15/2}$) → ($Er^{3+}$:$^4I_{15/2}$ + $Nd^{3+}$:$^4F_{5/2}$,$^2H_{9/2}$). Therefore, the population of $Er^{3+}$:$^4I_{13/2}$ decreases, which leads to a reduction in both 550 nm up-conversion and 1.5 mm emission.

**Supplementary Figure S4.** Energy level diagram of Er3+ and Nd3+ and the mechanism proposed to explain 550-nm, 1.5-µm, and 2.7-µm emissions.